This is to certify that the

dissertation entitled

COMPARISON OF POLARIZATIONS OF
INCLUSIVELY PRODUCED LAMBDAS AND ANTILAMBDAS
BY PROTONS, ANTIPROTONS AND KAONS

presented by

HARRY L. MELANSON

has been accepted towards fulfillment
of the requirements for

PH.D. degree in PHYSICS

Maris A. Abolins
Major professor

Maris A. Abolins

Date 5-3-85

COMPARISON OF POLARIZATIONS OF
INCLUSIVELY PRODUCED LAMBDAS AND ANTILAMBDAS
BY PROTONS, ANTIPROTONS AND KAONS

By

Harry Louis Melanson

A DISSERTATION

Submitted to
Michigan State University
in partial fulfillment of the requirements
for the degree of

DOCTOR OF PHILOSOPHY

Department of Physics

1985

in loving memory of my parents,
Roger and Virginia Melanson

ACKNOWLEDGEMENTS

I would like to thank my adviser, Maris Abolins, for his support and encouragement of this work. Above all, I would like to thank him for his caring and friendship in both good times and bad.

Thanks to Steve Gourlay, for sharing this experience with me. The most important result of this experiment is our friendship, and I cherish it.

To Hans Kobrak, who showed me how to do things correctly, and to Phil Yager, who showed me new approaches to solving problems, I extend my appreciation. Thanks also go to the rest of the E663 collaboration - Bob Swanson, Bill Francis, Randy Pitt, Ken Edwards and Werner de Rosario.

Thanks to the Meson Dept., the Computing Dept. and the entire Fermilab staff for their crucial support in this work. Special thanks go to Lisa Dillingham and Debbie Robbins back at M.S.U., for their help.

Finally, thanks to Venae, whose love I value above all else.

TABLE OF CONTENTS

Appendices

LIST OF TABLES

LIST OF FIGURES

CHAPTER 1

Introduction

1.1 Introduction

This experiment measured the polarization of lambdas inclusively produced by protons and kaons, and antilambdas inclusively produced by antiprotons at a beam momentum of 176 GeV/c using a liquid hydrogen target. In particular, the processes studied were

$$p + p \rightarrow \Lambda + X$$

$$\bar{p} + p \rightarrow \bar{\Lambda} + X$$

$$K^- + p \rightarrow \Lambda + X,$$

where X represents the collection of all other possible final state particles. This data represents the highest energy, fixed target study of $K^- \rightarrow \Lambda$ and $\bar{p} \rightarrow \bar{\Lambda}$ to date. It is also the first experiment to measure hyperon polarizations using three such beams with the same apparatus, and it allows for direct comparisons of the results.

Also studied was the process

$$K^- + p \rightarrow K^0_s + X.$$

This last reaction was used as a bias check since the K^0_s has spin zero, and thus cannot be polarized. The decay modes that were used were

$$\Lambda \rightarrow p + \pi^- \ (0.642)$$

$$\bar{\Lambda} \rightarrow \bar{p} + \pi^+ \ (0.642)$$

$$K^0_s \rightarrow \pi^+ + \pi^- \ (0.6861).$$

The branching ratios for these decays are given in the parentheses. Data were collected in the range

$$0.2 < X_F < 1.0$$

$$0.0 < P_\perp < 1.5 \text{ GeV/c},$$

where X_F is Feynman X and $P_\perp$ is the transverse momentum of the produced particle with respect to the beam particle. A total of 8,250 lambdas from K^-'s, 10,480 lambdas from p's, 4,800 antilambdas from $\bar{p}$'s, and 16,685 K^0_s's from K^-'s were used in the analysis.

1.2 Background

Because of the high charged particle multiplicities at high energy ($\langle n_{ch} \rangle \approx 7$ at $P_{lab} = 176$ GeV/c), it is very difficult both theoretically and experimentally to study any reaction in detail. To simplify the situation greatly, inclusive processes like $a + b \rightarrow c + X$ are used. If any of the particles in the above reaction have spin, then polarization effects can occur.

Polarization measurements provide a method of detecting small spin-dependent terms in the reaction amplitude that cannot be detected by cross section measurements. Before 1976, it was known that polarization effects in elastic scattering experiments became small as the energy increased, which was in agreement with simple Regge pole models [1]. Perturbative QCD calculations have also shown that there are no expected large polarization effects for high-$P_\perp$ hadron reactions [2]. The report of substantial polarization for inclusively produced lambda's by 300 GeV protons on Beryllium [3] was therefore somewhat surprising.

Since that time, it has been determined that many hyperons produced at high energy have non-zero polarizations. These measurements all seem to be consistent with the polarization being

$$\vec{P}_{a+A\to b+X} = f_{a,b}(X_F,P_\perp,A)\ \hat{n}, \quad [4]$$

where A is the atomic weight of the target nucleus, and $\hat{n}$ is the normal to the production plane. The function $f_{a,b}$ has the properties :

1. $df/dX_F > 0$.
2. $df/dP_\perp > 0$ for $P_\perp < 1.0$ GeV/c.
3. $df/dP_\perp \approx 0$ for $P_\perp > 1.0$ GeV/c.
4. The polarization is smaller for heavy nuclei than for light nuclei,

   e.g. $f(0.35, 1\ \text{GeV/c}, A=9) \approx 1.5\ f(0.35, 1\ \text{GeV/c}, A=136)$.

From a large data sample for $p + p \to \Lambda + X$, an empirical fit has been made to

$$f_{p,\Lambda}(X_F,P_\perp,A=1) = (\ a\ X_F + b\ X_F^3\ )\ (\ 1 - e^{-cP_\perp^2}),$$

with a = 0.295±0.010, b = 0.18±0.04 and c = 2.48±0.12 [5], for the range of $P_\perp$ up to 5 GeV/c. Table 1-1 shows the general relationship between $\vec{P}_{p,\Lambda}$ and the other measured channels.

Table 1-1. Comparison of Polarization from Various Reactions

Channel	Polarization
$p \to \Lambda$	$\vec{P} = \vec{P}_{p,\Lambda}$ [3,6-11]
$\bar{p} \to \bar{\Lambda}$ $p \to \Xi^-$ $p \to \Xi^0$	$\vec{P} \simeq \vec{P}_{p,\Lambda}$ [12-14]
$p \to \Sigma^+$ $p \to \Sigma^0$ $p \to \Sigma^-$	$\vec{P} \simeq -\vec{P}_{p,\Lambda}$ [15-17]
$K^- \to \Lambda$ $K^+ \to \bar{\Lambda}$	$\vec{P} \simeq -\xi\,\vec{P}_{p,\Lambda}$ $(\xi > 1)$ [18-23]
$K^- \to \Xi^-$	$\vec{P} \simeq \zeta\,\vec{P}_{p,\Lambda}$ $(\zeta > 1)$ [24]
$p \to \bar{\Lambda}$ $\pi^- \to \Lambda$ $p \to \bar{\Xi}^0$ $\gamma(\rho) \to \Lambda$ $K^+ \to \Lambda$	$\vec{P} \simeq 0$ [6,24-26]

Several theoretical ideas have been proposed to explain these features. One, by Andersson, Gustafson and Ingelman [27], suggests that polarization comes from the soft, semi-classical process of quark-antiquark pair production via tunneling in a confined color field. Another, by DeGrand and Miettinen [28], uses the parton-recombination model plus SU(6) to relate the polarization to a Thomas precession like term in the recombination process. Both of these models will be described in more detail later in this chapter.

1.3 Polarization Physics

To determine the polarization of a sample of lambdas, consider the weak decay mode

$$\Lambda \rightarrow p + \pi^- .$$

To conserve total angular momentum, the p-π system must be in a L=0 or L=1 state. For a lambda with its spin in the +Z direction, its decay amplitude is

$$\Psi = a_s \, Y_0^0 \, \chi^+ + a_p \left[\sqrt{\tfrac{2}{3}} \, Y_1^1 \, \chi^- + \sqrt{\tfrac{1}{3}} \, Y_1^0 \, \chi^+ \right]$$

where a_s and a_p are the S and P wave amplitudes, $\chi^{\pm}$ are the proton spin states, and the $\sqrt{\frac{2}{3}}$ and $\sqrt{\frac{1}{3}}$ are Clebsch-Gordon coefficients. The angular distribution is then

$$\Psi\Psi^* = \left(a_s^2 + a_p^2 \right) \left(1 + \alpha_\Lambda \cos\theta \right)$$

where

$$\alpha_\Lambda = \frac{2 \, a_s \, \mathrm{Re}(a_p)}{[a_s^2 + a_p^2]} ,$$

and θ is the angle between the pion and the lambda spin. Previous measurements have determined α_Λ to be

$$\alpha_\Lambda = -0.642 \pm 0.013$$ [29].

Finally, the angular distribution of the pion in the lambda center of mass is

$$\frac{dN}{d\Omega} = \frac{1}{4\pi} \left(1 + \alpha_\Lambda \, \hat{s} \cdot \hat{\pi} \right)$$

where $\hat{\pi}$ is a unit vector in the pion direction, and $\hat{s}$ is a unit vector in the lambda spin direction.

For an ensemble of lambda spins, we can integrate over all spin directions to get

$$\frac{dN}{d\Omega} = \frac{1}{4\pi} (1 + \alpha_\Lambda \vec{P} \cdot \hat{\pi}) \qquad (1-1)$$

where

$$\vec{P} = \int \vec{s} \, d\vec{s}$$

is the polarization vector. The measurement of lambda polarization can therefore be accomplished by determining the angular decay distribution of pions from lambda decays. The above analysis holds for antilambdas as well, with the assumption that

$$\alpha_{\bar{\Lambda}} = - \alpha_\Lambda .$$

This assumption relies on CP invariance for the lambda decay.

1.4 Theory

As mentioned earlier, simple Regge models and perturbative QCD calculations have failed to explain the measured polarizations. Attempts to apply triple Regge theory have also failed [30]. More recently, two semi-classical models have been suggested that yield some agreement with the data.

Andersson, Gustafson and Ingelman propose that the polarization of hadrons can be understood through the soft process of quarks tunneling through a confined color field. They assume that baryons can be described as bound states of a quark and a diquark (the diquark is made up of the two quarks with the most similar wave functions). In this framework, the lambda is made up of a ud singlet diquark, and an s quark, with the lambda spin being defined by the s quark. They first consider the channel $p \rightarrow \Lambda$. During beam fragmentation, the diquark of the incoming proton continues on as a unit. A color dipole field is stretched between the diquark and the central collision region. This color field is assumed to be confined, without any transverse degrees of freedom (like a 1-dimensional string). It is assumed that transverse momentum is locally conserved. To produce a lambda, an $s\bar{s}$ pair is created on the string. This pair will now have some orbital angular momentum. To conserve angular momentum, the spins of the quarks must be polarized in a direction opposite to the angular momentum.

The proposed method through which the spins become polarized is a Thomas precession during the production stage. In order to get the sign of the polarization correct, the color fields must be assumed to be confined, so that there is no interaction between the quark's magnetic moment and the color field [31]. A Monte Carlo involving the above model has given general agreement for low $P_\perp$, $p \rightarrow \Lambda$ data.

They apply the same proton fragmentation model to other channels, and give their expected signs for the polarizations (see Table 1-2). These signs are in agreement with the data.

For the reactions $K^- \to \Lambda$ and $K^+ \to \bar{\Lambda}$, the s quark comes from the incoming beam particle, and thus these channels cannot be handled by their model.

Table 1-2. Theoretical Expectations of Polarizations

Channel	Degrand and Miettinen	Andersson, *et al.*
$p \to \Lambda$	ε	$P > 0$
$p \to \Sigma^+, \Sigma^-, \Sigma^0$	$-(1/3\ \varepsilon + 2/3\ \delta)$	$P < 0$
$p \to \Xi^0, \Xi^-$	$1/3\ \varepsilon + 2/3\ \delta$	$P > 0$
$\pi, K^+ \to \Lambda$	$\delta/2$	
$K^- \to \Lambda$	$-\varepsilon$	

The model by Degrand and Miettinen is proposed within the framework of the parton-recombination model, assuming minimal complexity for quark transitions and uses SU(6) symmetry. They propose the following rule to describe the data - "slow partons preferentially recombine with their spins down in the scattering plane while fast partons recombine with their spins up". Here, as in Andersson, *et al.*, a baryon is considered to be made up of a quark and a diquark. This assumption implies that their model has two parameters - one for how single quarks combine, and one for how diquarks combine. To extract these two parameters, they use the results of $p \to \Lambda$ (where ud is the diquark), and $p \to \Sigma^+$ (uu is the diquark). By applying their rule and the two extracted parameters they make predictions for several other reaction channels. Table 1-2 gives a review of these predictions. The signs of these predictions are all in agreement with the current data. The relative magnitudes are in general agreement, with the exception of the $K^- \to \Lambda$ channel. Their model predicts the polarization for $K^- \rightarrow \Lambda$ to have the same magnitude as that for $p \rightarrow \Lambda$. The data show $K^- \rightarrow \Lambda$ has a much larger signal than $p \rightarrow \Lambda$.

To explain the dynamical origin of their rule, they propose that the spin of the parton undergoes a Thomas precession during recombination. This comes about because the force on the parton is in general not parallel to its initial momentum. Because slow partons are accelerated but fast partons are decelerated, the Thomas precession term in the Hamiltonian will be of opposite sign. By using this model and semi-classical arguments, they predict that the polarization should be approximately linear in $P_\perp$ and weakly dependent on X_F. This is in general agreement with the low $P_\perp$ dependence of the data, but disagrees with the X_F dependence.

Although this model contains some interesting agreements with the current data, it is in no way a satisfactory explanation of the observed polarization signals.

CHAPTER 2

Apparatus

In order to satisfy the goals of this experiment, the apparatus had to determine the type of incoming beam particle and measure its vector momentum, identify events containing final state Λ, $\bar{\Lambda}$ or K^0_s's and determine their vector momenta, and measure the vector momenta of their decay products. The apparatus used in this experiment satisfied these requirements, and is shown schematically in Figure 2-1.

A Cerenkov counter was used to tag the incoming beam particle. Its vector momentum was measured by a beam spectrometer. The beam was then focused onto a liquid hydrogen target to produce the Λ, $\bar{\Lambda}$ and K^0_s's. Located just downstream of this target was a 6' long magnet with a 0.8 GeV/c $P_\perp$ kick which attempted to sweep out any charged particles produced in the target, while leaving all of the desired neutral particles uneffected. Following the magnet was a 14.6 m long evacuated region where most of the neutrals decayed. Finally, a forward spectrometer was used to measure the momenta and positions of their decay products. The lab coordinate system was defined such that X measured horizontally (+X was beam left), Y measured vertically (+Y was up) and Z measured along the beam (+Z was in the beam direction).

Each section of the apparatus will now be described in detail.

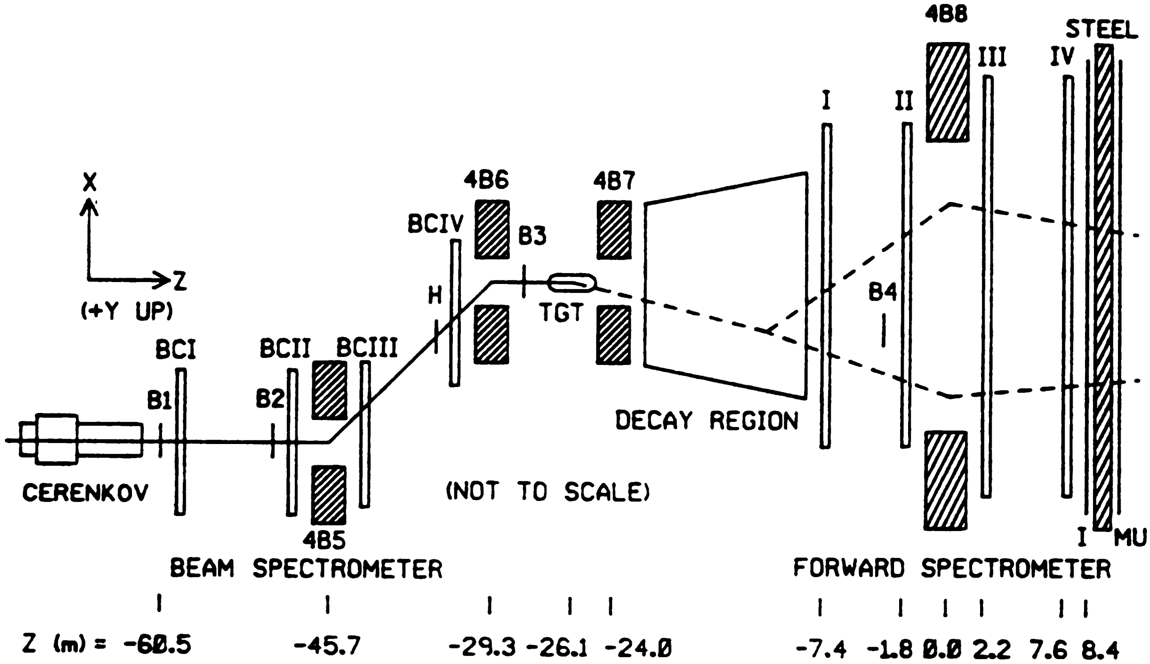

Figure 2-1. Plan View of the Apparatus

2.1 Fermilab M4 Beam Line

This experiment was performed in the Fermilab M4 beamline [32] during the period from March, 1980 to June, 1980. The beam was made from primary, 400 GeV/c protons incident on a 1.5 mm x 1.5 mm x 203 mm Beryllium target. Particles coming off at a 6.8 mrad production angle were selected by a 10' long steel collimator located 200 m from the target. This selection had the effect of lowering the total possible hadron flux. The lowered flux was necessary to allow the tagging of each beam particle by the Cerenkov Counter. The beamline was able to be tuned to select either positive particles (for protons), or negative particles (for kaons and antiprotons). To change from a positive beam to a negative one, the magnetic fields of the beam magnets were reversed. The 6.8 mrad production angle also had the effect of increasing the K^- and $\bar{p}$ fraction in the negative beam. The composition of the negative beam is given in Table 2-1. The positive beam was dominated by protons. The beam line was tuned to have an average momentum of 176 GeV/c with a spread of 2.8 %.

Table 2-1. Negative Beam Composition

Particle	Fraction
π^-	0.91
K^-	0.06
$\bar{p}$	0.03

2.2 Cerenkov Counter

A differential Cerenkov counter [33] was used to identify protons in the positive beam and kaons and antiprotons in the negative beam. Figure 2-2 shows a schematic of this counter. By adjusting the pressure of the gas in the counter, the threshold was set so that particles with a mass less than or equal to that of a proton would radiate light. The radiator consisted of a 75 m beam pipe filled with He. Light from a particle above threshold was reflected by the primary mirror (M1) onto the secondary mirror (M2). The secondary mirror had a hole in its center and a mask around its outer rim. Light from protons would go through the hole in M2 and be detected by the photomultiplier tube P. Light from kaons would be reflected by M2 into the photomultiplier tube K. Pion light would fall on the masked region of M2, and would not be detected. The pressure in the counter was adjusted to maximize the separation between the proton and kaon signals. Figure 2-3 shows the P pulse height versus the K pulse height. The overlap between protons and kaons is very small (less than 0.05 %). The counter was operated at 0.55 atm.

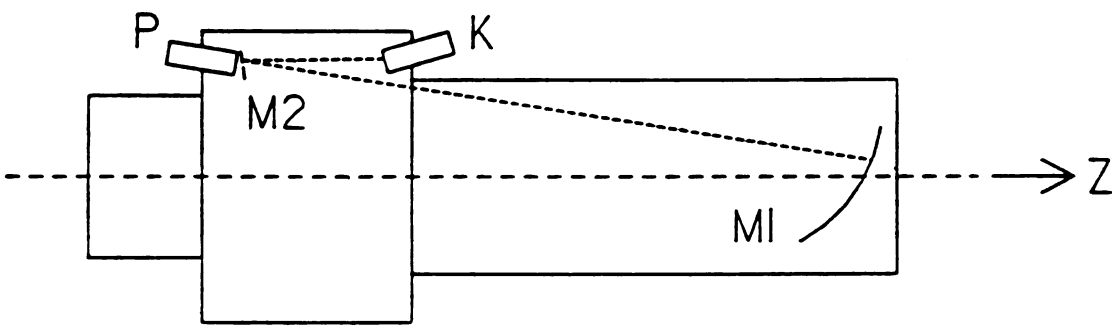

Figure 2-2. Cerenkov Counter

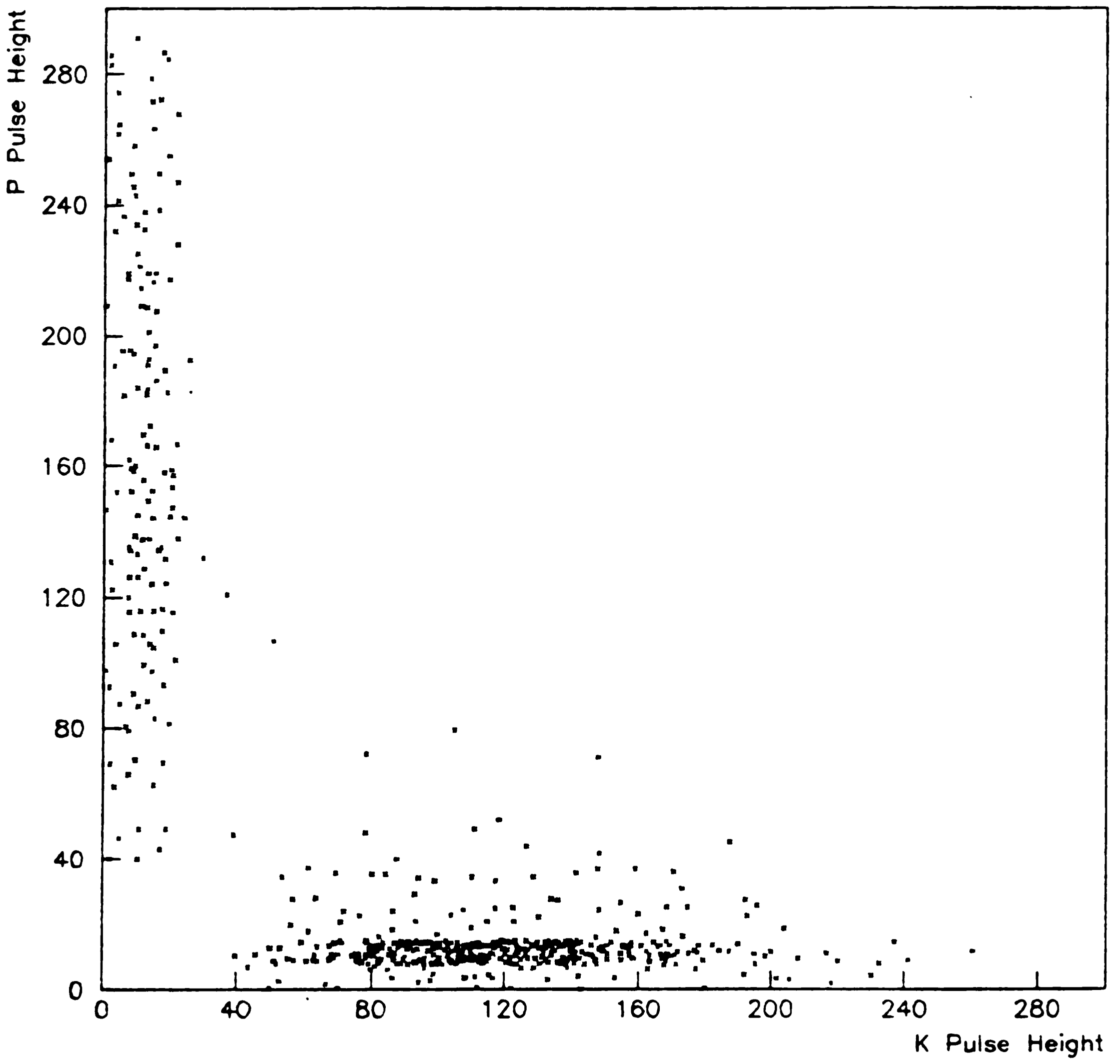

Figure 2-3. P Pulse Height versus K Pulse Height

2.3 Beam Spectrometer

A spectrometer consisting of small proportional wire chambers [34] was used to determine the position and momentum of the incoming beam. This system is shown in Figure 2-4. It was composed of four stations, each station made up of an X and a Y chamber. Each chamber contained 64 sense wires spaced 1.0 mm apart. The sense wires were 12 μm gold plated tungsten. The gas used was CO_2 (20%), Freon 13B1 (0.15%) and Argon (balance).

The readout system [35] (Figure 2-5) utilized a digital delay-line scheme. Each chamber was connected to separate 64 bit, 16 word memories. Every 50 ns, the condition of each wire was recorded into its memory. The words in each memory were addressed in a circular fashion with the newest information overwriting the oldest. At any one time, there was 50 x 16 = 800 ns of wire history stored in the memories.

Upon receiving a fast trigger signal (to be described later), the storing of information in the memories was halted, and a selected word from the memory was loaded into a shift register. The particular word to be loaded was determined by the timing requirements of the trigger.

After the data had been loaded, the shift registers were read out serially by a CAMAC scanner module [36]. The scanner used a 10 Mhz clock to read out all eight chambers in 51.2 μsec. Since the number of hits expected in each chamber was small, the scanner only reported the location and size of clusters of hits, ignoring sections of unhit wires. This cluster information was stored in a 16 word memory in the scanner. Each word could report the location of a cluster up to 7 wires long. The location of a cluster was defined as the address of the last wire hit in that cluster.

The magnet used to determine the momentum of the beam (4B5 in Figure 2-4) had a $P_{\perp}$ kick of 1.6 GeV/c. A second magnet (4B6) was used to straighten out the beam after it passed through the beam spectrometer system. This magnet was identical to and was run in series with the first magnet, its current running in the opposite direction to insure that the two magnetic fields were equal in magnitude and opposite in direction. The fields were measured with a Hall probe and were found to be equal to within 0.4 %.

The average position resolution for a beam chamber was 265 μm, and the average momentum resolution of the system was 0.4 %.

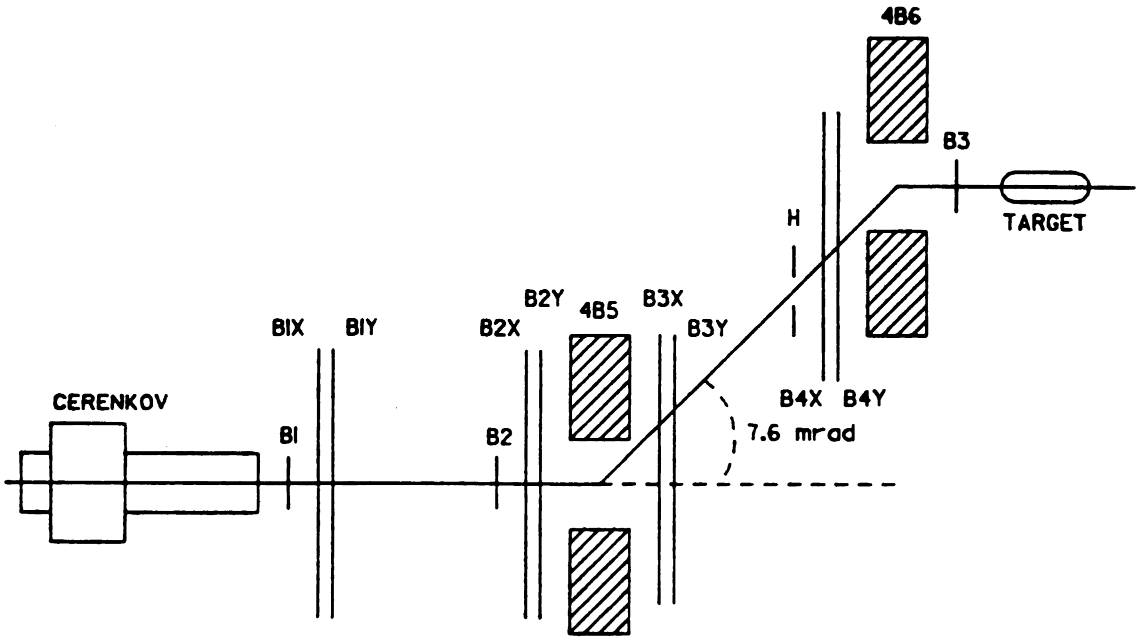

Figure 2-4. Beam Spectrometer

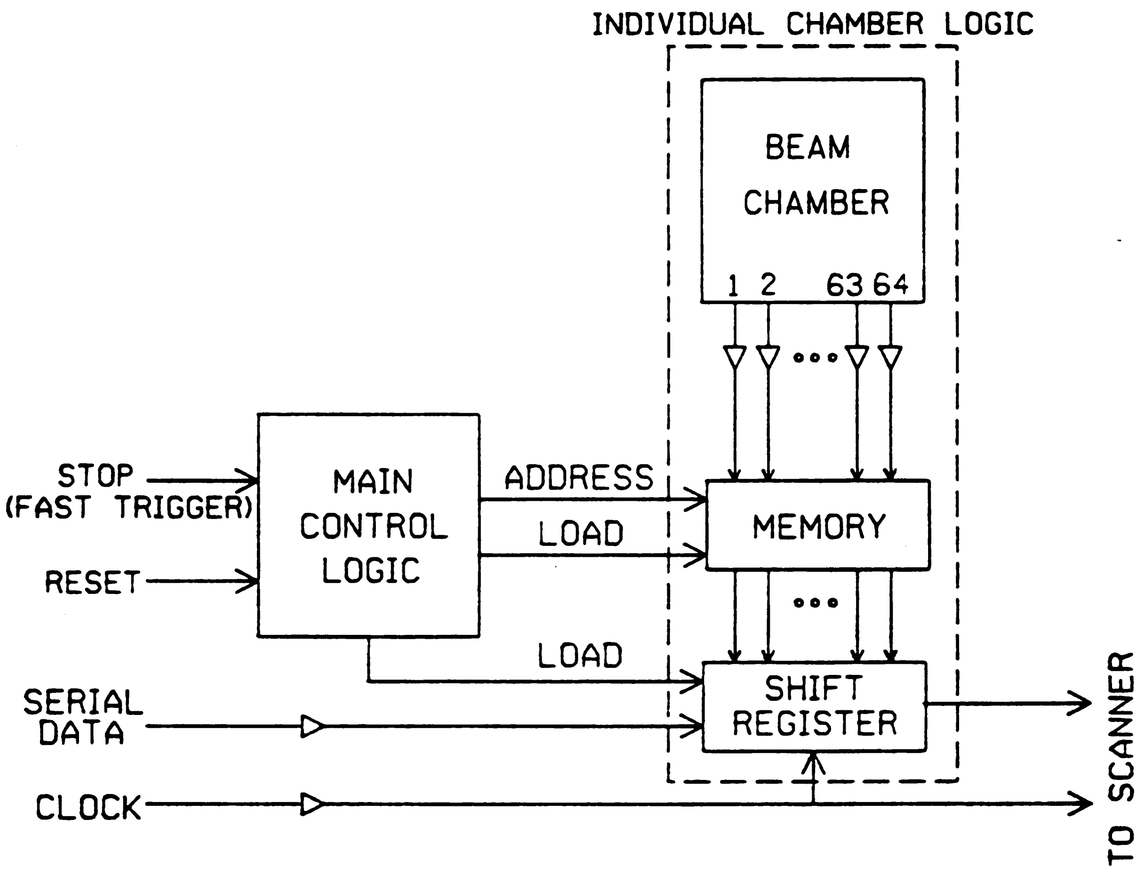

Figure 2-5. Beam Chamber Readout

2.4 Sweeper Magnet

Located just downstream of the target was a magnet (4B7) used to sweep out charged particles produced in the target, without affecting the trajectory of the Λ's, $\bar{\Lambda}$'s and K^0_s's. It was run in ramped mode, and the $P_\perp$ kick at the top of the ramp was measured with a Hall probe to be 0.85 GeV/c. The magnet was intended to be operated at this maximum field during the spill, with the ramping occuring before the spill. However, by using reconstructed, non-interacting beam tracks, it was determined that the magnet was still ramping during the spill. The average kick was determined to be 0.78 GeV/c, with a difference between the beginning and end of spill of 8 %. It was assumed during the data analysis that the field was a constant 0.78 GeV/c. The effect of this assumption is discussed in Section 4.2 under systematic errors.

2.5 Target

A liquid hydrogen target built by the Hydrogen Target Group at Fermilab was used. It consisted of two flasks, one 25.4 cm long and the other 45.7 cm long. Their diameters were 5.1 cm. The flasks were made out of 0.127 mm Mylar. The two flasks, a reservoir, and a refrigerator were all enclosed in a foam vacuum vessel. This vessel had a 0.127 mm Mylar upstream window.

2.6 Forward Spectrometer

The forward spectrometer was composed of four stations, with two stations upstream and two stations downstream of the analysis magnet (Figure 2-6). Each station was identical, consisting of a proportional wire chamber (PWC) section and a drift chamber section. The PWC section contained X and Y planes, and the drift chamber section contained X, Y, U and V planes. The U,V planes were oriented at ± 45° with respect to the X,Y planes. The analysis magnet was operated at a constant current to maintain a 0.2 GeV/c $P_{\perp}$ kick. Its field was in the Y direction. The average momentum resolution of the system was 2 %.

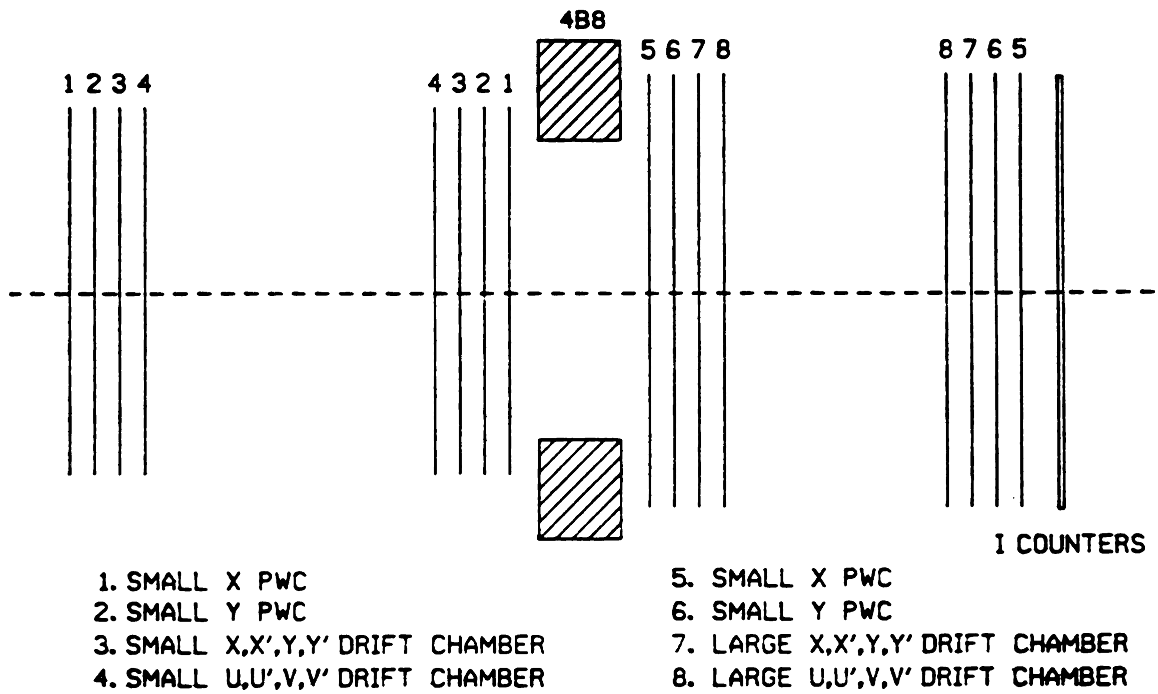

Figure 2-6. Forward Spectrometer

2.6.1 Proportional Wire Chamber System

The PWC system [37] consisted of eight chambers. Each chamber included one plane of sense wires located half way between two planes of high voltage wires. The high voltage wires were oriented perpendicular to the sense wires. The spacing between the sense wires was 2.0 mm. The spacing between the high voltage wires was 1.0 mm. The sense wires were either 20 or 25 µm gold-plated tungsten and the high voltage wires were 64 µm phosphor-bronze. The windows were made of 0.051 mm Aclar (type 3C). The gas used was CO_2 (20%), Freon 13B1 (0.15%) and Argon (balance).

There were two sizes of proportional chambers - their dimensions are listed in Table 2-2. Each chamber had support wires made out of AWG 30 wire wrap wire running perpendicular to the sense wires, attached with glue to each wire. These were included to eliminate electromechanical vibrations in the sense wires. The number of support wires per plane is listed in Table 2-2. They were equally spaced throughout each chamber. They also had the undesirable effect of deadening about a 7.0 mm region of the chamber running along each support wire.

Each sense wire was connected to an amplifier, and the amplifier was connected to the input of a one-shot (Figure 2-7). The one-shot was used as an adjustable delay. If a fast trigger occured, the trailing edge of each one-shot output would be latched into a single, long shift register. The shift registers for each plane were read out serially by individual CAMAC scanner modules. These scanners were of the same type as the one used to read out the beam chambers. It took about 100 μsec for the scanners to read out the information in the shift registers.

The average position resolution obtained was 533 μm. The average efficiency was 96 %. A lower efficiency was found in the center of each chamber, coinciding with the region through which the beam passed. This region was approximately 5 x 5 cm in size, and the average efficiency in it was 73 %.

Table 2-2. PWC Information

Chamber	Size	Support Wires
P1X	1.2 x 0.8 m	1
P2X	1.2 x 0.8 m	1
P3X	1.5 x 1.2 m	2
P4X	1.5 x 1.2 m	2
P1Y	1.2 x 0.8 m	2
P2Y	1.2 x 0.8 m	2
P3Y	1.5 x 1.2 m	3
P4Y	1.5 x 1.2 m	3

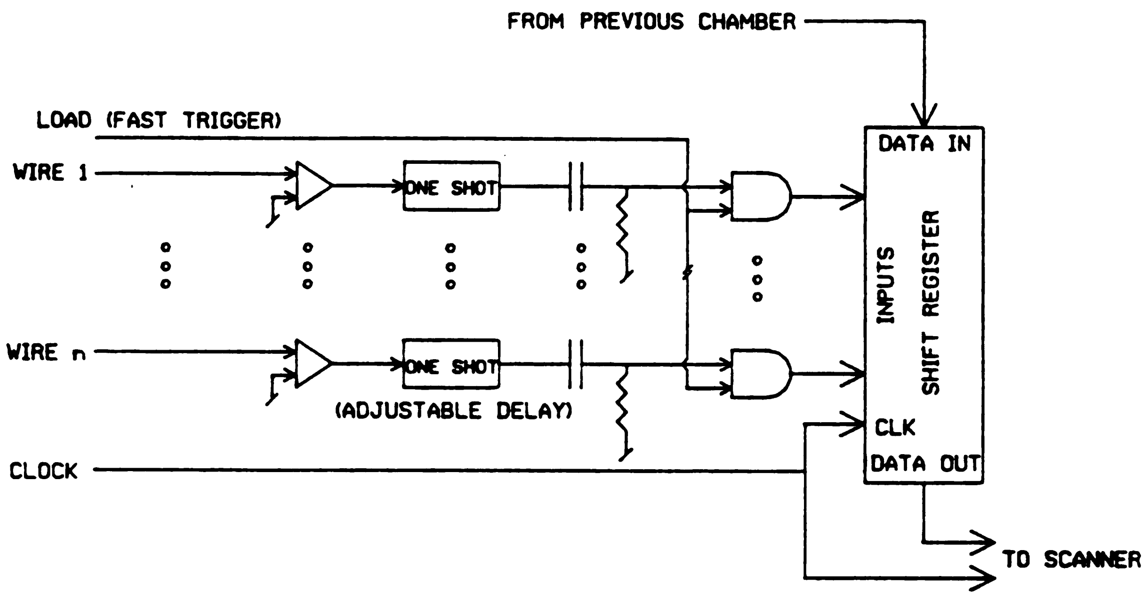

Figure 2-7. PWC Readout System

2.6.2 Drift Chamber System

The drift chamber system [38] consisted of four stations, each station containing eight planes labelled X,X',Y,Y',U,U',V, and V'. Primed planes had wires parallel to unprimed planes of the same type, but offset by one cell length. The cell length (defined as half the distance between adjacent sense wires) was 5 cm. The active area of the chambers was matched to those of the PWC's. The X,X' and Y,Y' planes formed a common gas enclosure, as did the U,U' and V,V' planes. The gas used was CO_2 (10%), Freon 13B1 (0.15%) and Argon (balance). The windows of the chambers were made of 1 mil Aluminum, 3 mil Mylar laminate. A cross section of a package is shown in Figure 2-8.

The drift field in a cell was generated by 30 field wires divided into two parallel planes of 15 wires each. These two planes were separated by 9.52 mm, with the sense wire plane centered between them. Located at the interface between two cells were 3 additional field wires. Two of these wires were in the plane of the field wires, and the third was located in the plane of the sense wires. These last 3 wires were included to improve the definition of the electric field at the interface between adjacent cells. The voltages on the field wires were supplied by a 15 resistor voltage dividing chain (one chain per plane), and were set so that the average field in the cell was 1200 V/cm. The field wires were 100 μm beryllium copper, spaced 3.18 mm apart. The sense wires were 20 μm gold plated tungsten.

The output of each sense wire was amplified and sent to a time to digital converter (TDC). The TDC system contained a separate scaler for each wire, and a shared clock module [39] for each station (Figure 2-9). The signal from the sense wire was used to reset the scaler. A fast trigger was used to stop the scaler. The scaler determined the time between these two signals by counting the number of clock pulses between them. All scalers were stopped by the same signal (common stop).

In order to increase the precision of time measurement (see Figure 2-10), the time between the reset and the following rising clock transition (T_a) was stretched by 16:1 and digitized for each channel. The time between the first rising clock transition following the reset and the first rising clock transition following the stop (T_b) was then digitized by counting clock transitions for each channel. The time between the stop and the following rising clock transition (T_c) was stretched 16:1 and was digitized at twice the clock frequency in the clock module. This time was later subtracted from all channels that shared that clock module. The clock frequency was 20 MHz.

The single hit capability of the drift chamber system prevented it from working at the high rate of the incoming beam. To solve this problem, the region of the chambers where the beam passed through was deadened. This was accomplished by placing plastic sleeves over sections of wires that would have been exposed to the beam. The average deadened area was 10.0 cm^2. Unfortunately, these dead regions were positioned for a previous experiment and did not correspond to the location of the beam in this experiment. To correct for this, hits on wires that were affected by our beam were totally removed by software prior to pattern recognition.

The drift chambers were used to measure the intercept of a transversing particle by relating the clock time to the spatial position of the intercept. A linear relationship was assumed for most of the chamber. The functional form used was

$$X = X_0 \pm V_{\pm} (T_0 - T)$$

where T is the clock time, X_0 is the wire location, T_0 is an offset time, $V_{\pm}$ are drift velocities (one for either side of the wire), and X is the position of the hit. The constants X_0, T_0 and $V_{\pm}$ were obtained for each wire using the PWC system as a reference (see Appendix II for more details). The chambers were aligned to within ± 25 µm and had an average position resolution of 510 µm. Their average efficiency was 65 %.

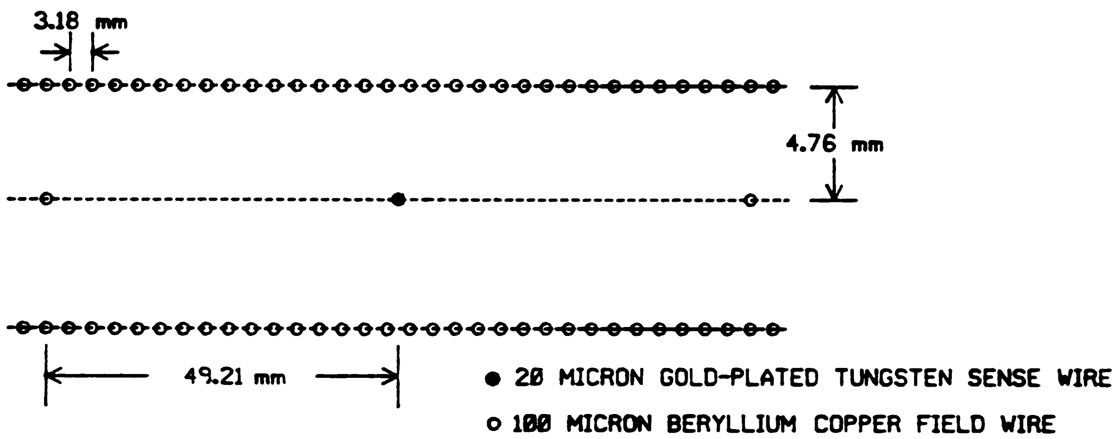

Figure 2-8. Drift Chamber Cell

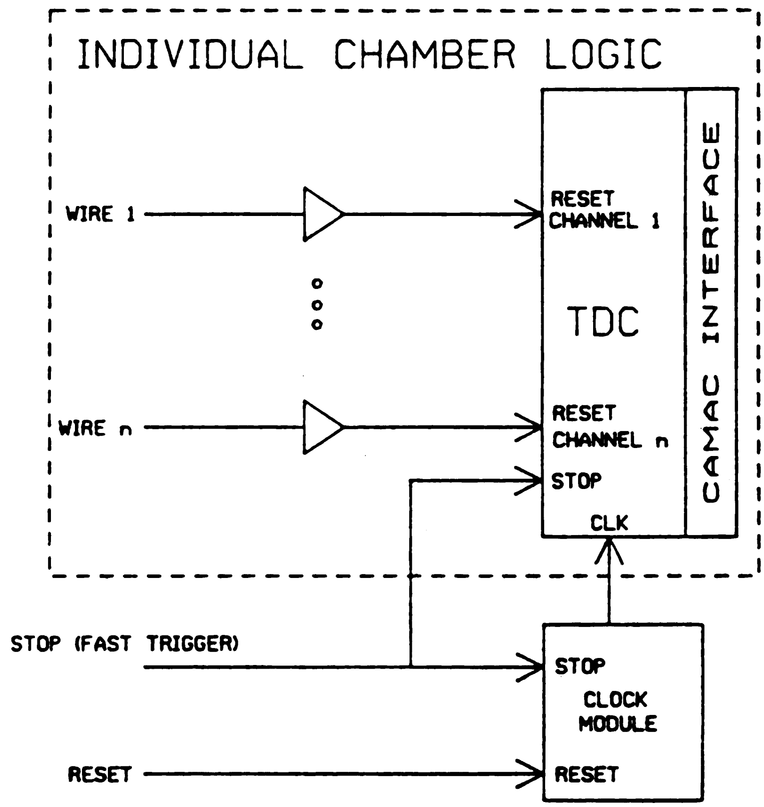

Figure 2-9. Drift Chamber Readout System

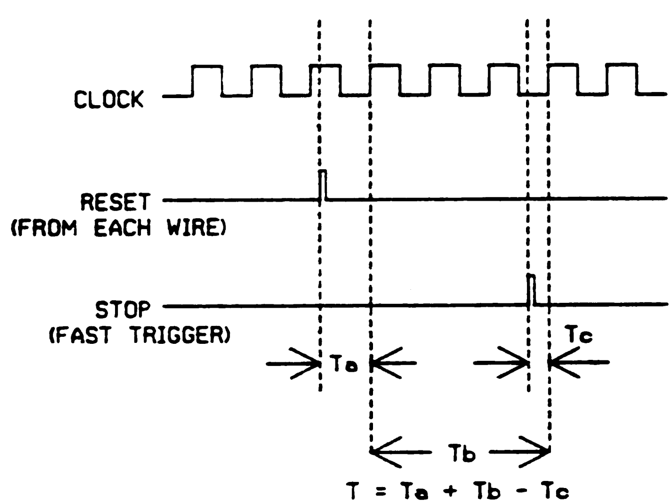

Figure 2-10. Drift Chamber Time Stretcher

2.7 Trigger

Since the inclusive cross sections for producing a Λ, $\bar{\Lambda}$ or K_s^0 are much smaller than the total cross section, most of the interactions in the target were not pertinent to this experiment. In order to avoid wasting time analyzing these interactions, a trigger was set up to attempt to identify only events that contained a Λ, $\bar{\Lambda}$ or K_s^0 decay.

This trigger was composed of two parts - the fast trigger and the slow trigger. The fast trigger was constructed of signals from various scintillation counters, and was used to insure that a beam particle had gone through the beam spectrometer, and had then interacted in the target. The slow trigger was issued by a trigger processor. It tried to identify those interactions that contained a Λ, $\bar{\Lambda}$ or K_s^0 decay. The two parts of the trigger are discussed in more detail below.

2.7.1 Fast Trigger

The logic used in the fast trigger is illustrated in Figure 2-11. The locations of the scintillator counters used as input to this logic are shown in Figure 2-1. The counters B_1, B_2 and B_3 were used to detect the passage of an incoming beam particle. The counter H had a hole in it for the beam to pass through and was used to veto any beam halo. The sizes of these various counters are given in Table 2-3. The signals from these counters, along with a signal from the Cerenkov counter (either K or P) were used in coincidence to define the valid beam signal

$$\text{Beam} = B_1 \cdot B_2 \cdot B_3 \cdot \overline{H} \cdot (K + P).$$

To detect interactions in the target, a counter hodoscope (I) was located just downstream of the forward spectrometer, and was used to identify events with at least one charged particle (other than a beam particle) exiting the apparatus. Two holes were provided for the beam to pass through - one for for running with the positive beam and one for running with the negative beam. The signals from the I counters were logically summed together to form the signal

$$I = \sum I_i.$$

In addition to these counters, a small counter (B_4) was positioned just upstream of the first chamber, centered on the beam. Its purpose was to veto diffractive events that would have triggered the experiment if only the I counters were used. The I counters and the B_4 counter signals were combined to form the interaction signal

$$IT = I \cdot \overline{B}_4 .$$

To prevent triggers from occuring during data acquisition, a level called "Dead" was generated by the data acquisition computer, and was used as a veto.

These signals, in coincidence with the valid beam signal, formed the fast trigger

$$\text{Fast} = \text{Beam} \cdot IT \cdot \overline{\text{Dead}}.$$

Table 2-4 gives some typical rates for these various signals.

Table 2-3. Trigger Counter Sizes

Counter	Size
B_1	3.0 x 6.0 cm
B_2	3.0 x 6.0 cm
B_3	3.0 x 6.0 cm
B_4	4.2 x 3.6 cm
H	10.2 x 30.5 cm
H(hole)	2.54 x 2.54 cm

Table 2-4. Trigger Rates

Signal	Average Rates (per spill) Positive	Negative
Incoming Beam	0.28×10^6	0.33×10^6
$B_1 \cdot B_2 \cdot B_3$	0.28×10^5	0.14×10^6
$B_1 \cdot B_2 \cdot B_3 \cdot \overline{H}$	0.25×10^5	0.13×10^6
Beam	0.82×10^4	0.45×10^4
$B_1 \cdot B_2 \cdot B_3 \cdot \overline{H} \cdot \overline{B}_4$	0.39×10^4	0.16×10^5
Fast	638	325
OK	75	45

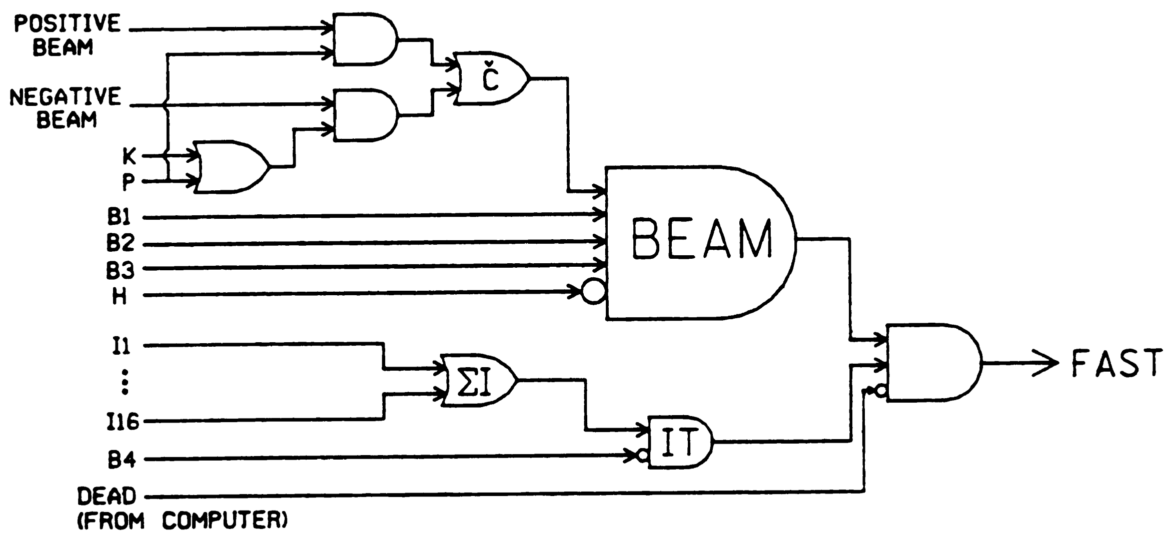

Figure 2-11. Fast Trigger Logic

2.7.2 Trigger Processor

In order to enhance the number of Λ, $\bar{\Lambda}$ and K^0_s's in the event sample, a second, slower level of selection was incorporated into the trigger. A simple device was built to supply this secondary trigger requirement - the trigger processor. This home built, TTL device attempted to identify events containing two tracks (hopefully from a Λ, $\bar{\Lambda}$ or K^0_s decay) by counting the number of hits in the PWC's, and selecting those events whose hit pattern was consistent with the two track topology. It succeeded in increasing the good event to trigger ratio by a factor of four.

If the PWC's were 100% efficient, a good event would cause each PWC to contain two hits, one from each track. With the actual PWC efficiencies, requiring each PWC to contain two hits would make the probability of triggering on the event 0.52. By relaxing this requirement to allow one out of the eight PWC's to miss a hit, the triggering probability becomes 0.87. Because of electronic noise and extra, unrelated tracks within good events, each chamber generally contained more than the two hits associated with the actual decay. The hit pattern requirement that was used for data taking required at least seven out of the eight PWC planes to have two or more hits in them, and allowed the eighth to have one or more.

A schematic of the trigger processor is shown in Figure 2-12. The clock and data lines from each PWC went to separate hit counter boards, one board for each plane. The hits were counted here, and a two bit result was obtained for each plane. In order to help eliminate the effects of spurious hits and tracks not associated with real Λ, $\bar{\Lambda}$ or K^0_s decays, only the central region of each chamber was examined by the hit counters. These regions were defined by the window boards. The circuits on the window boards counted the incoming clock pulses, and only activated the hit counters when the desired regions became available. The windows were obtained from a Monte Carlo study, and were stored by computer into the window latches at the beginning of each run. The latches were read back at the beginning of each spill, and checked to see if they were correct.

The eight 2 bit numbers from the hit counters formed a 16 bit address that was used to reference the 64k x 1 memory. The memory was used to determine whether the hit pattern in that event should be accepted. The memory was downloaded by the computer with the desired hit pattern requirements at the beginning of each run. It was monitored throughout the run to make sure it did not change.

The fast trigger initiated the trigger processor operation. After about 100 μsec, the processor decided if the event had a proper hit pattern, and if it did, a slow trigger (OK) was issued, and data acquisition proceeded. If not, a clear signal was generated to reset the experiment for the next fast trigger. The speed of the trigger processor was dominated completely by the scanning rate of the PWC's.

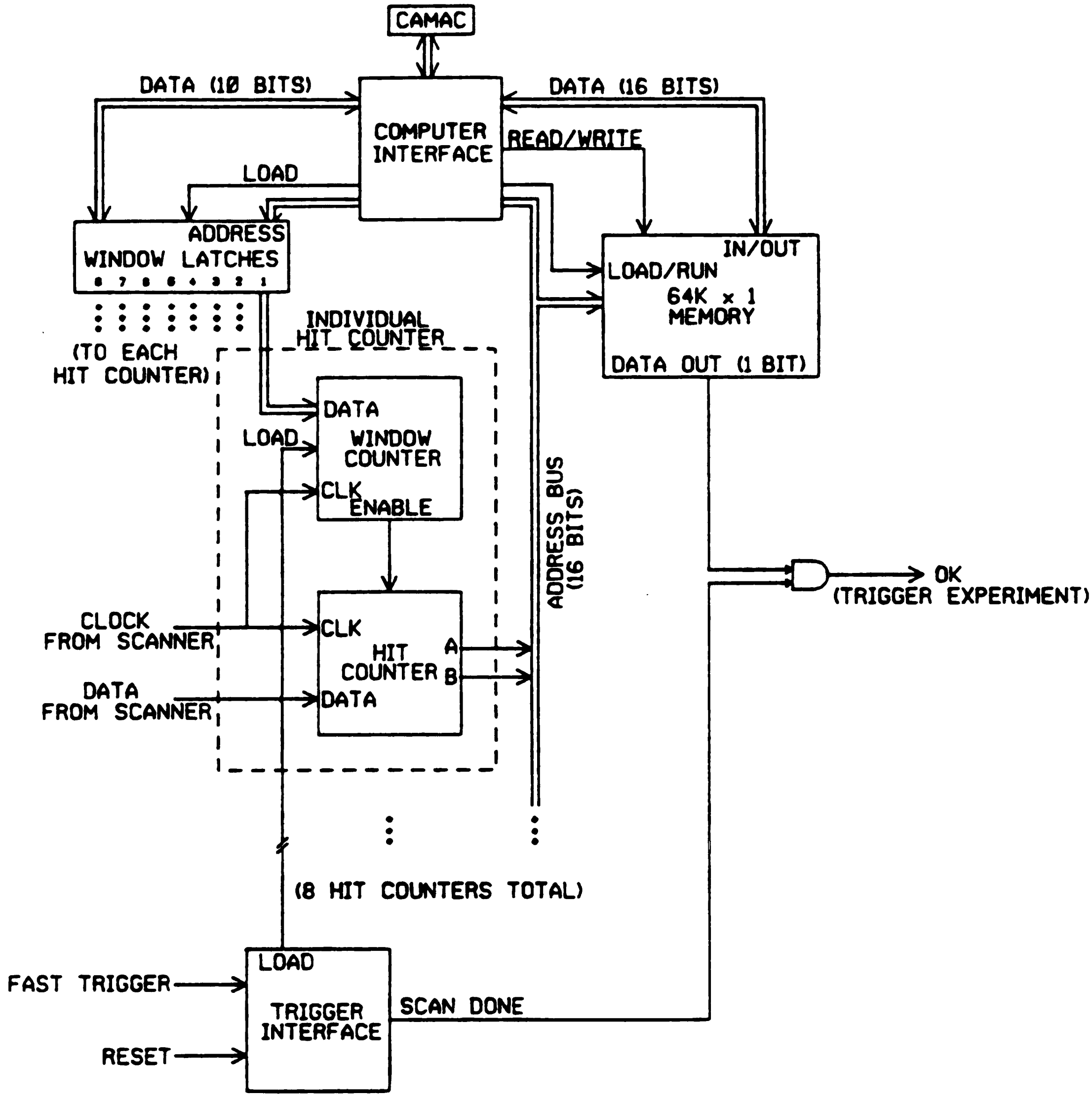

Figure 2-12. Trigger Processor

2.7.3 Auxiliary Triggers

In addition to the trigger described above, two other auxiliary triggers were used:

The first was the straight through trigger (identical to Beam described previously) :

$$ST = B_1 \cdot B_2 \cdot B_3 \cdot \overline{H} \cdot (K + P).$$

It consisted mostly of beam particles that did not interact in the target, and was used to align the beam chambers, as well as to align the beam spectrometer system with the forward spectrometer system.

The second auxiliary trigger was a muon trigger. It used a counter hodoscope (the Mu counters in Figure 2-1) which was situated downstream of the rest of the apparatus, behind 3 m of steel. The logic used to define this trigger was

$$Mu = \sum I_i \cdot \sum Mu_i.$$

The muon trigger was run with 4B5, 4B6, 4B7 and 4B8 turned off, and with a 1.37 m long piece of steel lowered into the beam 290 m upstream of the Cerenkov counter. Muons from pion decays were selected by this trigger. They were used to align the chambers within the forward spectrometer.

Both of these auxiliary triggers were run with the trigger processor set to accept any fast trigger.

2.8 Data Acquisition

The fast trigger initiated the latching of information from the various parts of the apparatus into their respective CAMAC modules. The slow trigger initiated the readout of this information through the CAMAC highway. It consisted of seven standard crates, each controlled by type A-1 crate controllers. The highway was interfaced to the data acquisition computer, an Eclipse S/200, through a modified BIRA 1251 BD branch driver. The information was read in using direct memory access, and was written onto 800 BPI magnetic tape. The dead time during this read was approximately 10 msec.

Data acquisition only occurred during beam spills. A spill was 1 second long, and the time between spills was 10 seconds. During this intermediate time, events were analyzed by the Eclipse to monitor the behavior of the apparatus.

A total of 135 tapes was written, corresponding to 2.7×10^6 triggers.

CHAPTER 3

Analysis

The analysis of this data was divided into three distinct steps - pattern recognition, data reduction, and polarization studies. The pattern recognition phase converted the digital information on the data tapes into spatial tracks. The data reduction phase used these tracks to identify events containing the decay of a Λ, $\bar{\Lambda}$ or K^0_s. These selected events were then studied to see if any polarization effects could be found. Each of these three steps will now be described in detail.

3.1 Pattern Recognition

The pattern recognition was performed by a computer program that used the digitized information on the data tapes to construct 3-dimensional space tracks which corresponded to the passage of charged particles through the experiment. It attempted to locate all the tracks in the spectrometer system regardless of the kinematic configuration of the event. The following is a summary of the algorithm used.

First the information from the various chambers (drift times for drift chambers, wire numbers for PWC's, etc.) was converted into spatial coordinates. It was at this point that hits associated with drift chamber wires in the beam region were removed (see Section 2.6.2).

Next, a search was made for tracks in the Y view. This view was chosen first because it was the non-bending view (except for a small vertical focusing component), and thus tracks in this view should be straight all the way through the spectrometer. To find these tracks, all combinations of Y PWC hits forming straight lines were considered. Hits in the Y drift chambers that lay close to these lines were added to them. Any of these hit patterns that passed a set of minimal requirements (such as the total number of hits, or the χ^2 for a straight line fit) were then considered as Y track candidates.

Finally, a search was made for track projections in the other views that could be linked up with these Y candidates. In each of the X, U, and V views, the particle tracks are bent by the analysis magnet. The projections in these views will thus consist of straight lines upstream and downstream of the magnet, which meet at its center. Because of this, the algorithm handled the upstream and downstream sections separately (and identically). Pairs of XU, XV and UV hits were formed. The Y position of each hit pair was calculated, and if a Y track was found close to that position, the hit pair was combined with that Y track.

Each combination was then used to predict hit positions in the other X, U and V chambers. Hits found close to the predicted positions were then included in those combinations. Upstream and downstream hit combinations that passed another set of minimal cuts were then combined, and pairs that matched up at the center of the analysis magnet were considered spatial tracks, to be used in further analysis. For a very detailed description of the pattern recognition program (including all cuts used), see Appendix I.

Inefficiencies of this algorithm could be caused by several things. Chamber inefficiencies could lower the number of detected hits on the track below the minimum required. Two tracks close together might not be resolved, because of the single hit capability of the drift chambers. Finally, extraneous hits (noise) not associated with real tracks could, when combined with real hits, cause the misidentification of tracks. While the first two inefficiencies can be handled with our Monte Carlo studies, no attempt has been made to measure the third. After studying by eye the behavior of the algorithm on a large number of real data events, it was concluded that this inefficiency is small.

3.2 Data Reduction

In the data reduction phase, previously found tracks were used to reconstruct the decays of Λ, $\bar{\Lambda}$ and K^0_s's. The topology of these events is two tracks in the forward spectrometer that are the decay products of a single, neutral particle produced at some point in the target. Accompanying these forward tracks must be an incoming beam track which produced the neutral particle. To identify events consistent with these characteristics, a set of cuts was applied to the data.

Each event was first required to contain one and only one beam track. The beam track was required to have at least 6 hits, with hits in B1X and B4X mandatory (these were the chambers that most strongly affected the momentum and position resolution). In addition, the reconstructed momentum of the beam track had to lie within the range

$$160 < P_{Beam} < 200 \text{ GeV/c}.$$

This cut removed small tails in the momentum spectrum that were not modeled by the Monte Carlo. Finally, a unique particle identification by the Cerenkov counter was required. These cuts eliminated 13 % of the data, mostly due to an inefficiency in B1X or B4X.

Next, the quality of individual forward tracks was considered. The χ^2 per degree of freedom from a fit to the hypothesis of a single kink (including vertical focusing) at the center of the analysis magnet had to be less that 2.5 for each track. The X and Y intercepts of the track at the center of the analysis magnet (X_{4B8}, Y_{4B8}) had to lie within the magnet's aperture. Also, the X and Y intercepts at each PWC were required to be within the PWC windows that were used by the trigger processor during data taking.

After passing these cuts, all pairs of remaining forward tracks within each event were considered as possible products from the decay of a single, neutral particle; that is, they had to form a neutral V. Each pair of tracks was required to have a total charge of zero, i.e. the two tracks had to be oppositely charged. The charge of a track was determined by the direction of its bend in the analysis magnet. The pair of tracks also had to form a well defined decay vertex. The location of the vertex was defined as the point of closest approach between the two tracks. The distance between the two tracks at this point (C_{Decay}) was required to be less than 1.0 cm. The vertex had to also lie within the evacuated decay pipe region.

To eliminate neutral V candidates that were really by-products of a direct interaction in the target, cuts based on the hypothesis illustrated in Figure 3-1 were applied. Here, the two tracks were traced back through the sweeper magnet, and a search was made for a new vertex. For the undesired interactions, this vertex will be located within the target. Since the $P_\perp$ of the sweeper is so much greater than the decay $P_\perp$ of a Λ, $\bar{\Lambda}$ or K^0_s, if the tracks from these decays are traced back through the sweeper, they will form a false vertex at the center of the sweeper. Figure 3-2 shows the Z position of the vertex of all track pairs for the direct interaction hypothesis (Z_{INT}). A bump at the target from direct interactions and a bump at the center of the sweeper from actual neutral decays can be seen. All events with Z_{INT} less than -25.25 m were rejected. This hypothesis successfully accounted for 49 % of all triggers. Monte Carlo studies have shown that only 7 % of the Λ, $\bar{\Lambda}$ and K^0_s's were lost by this cut.

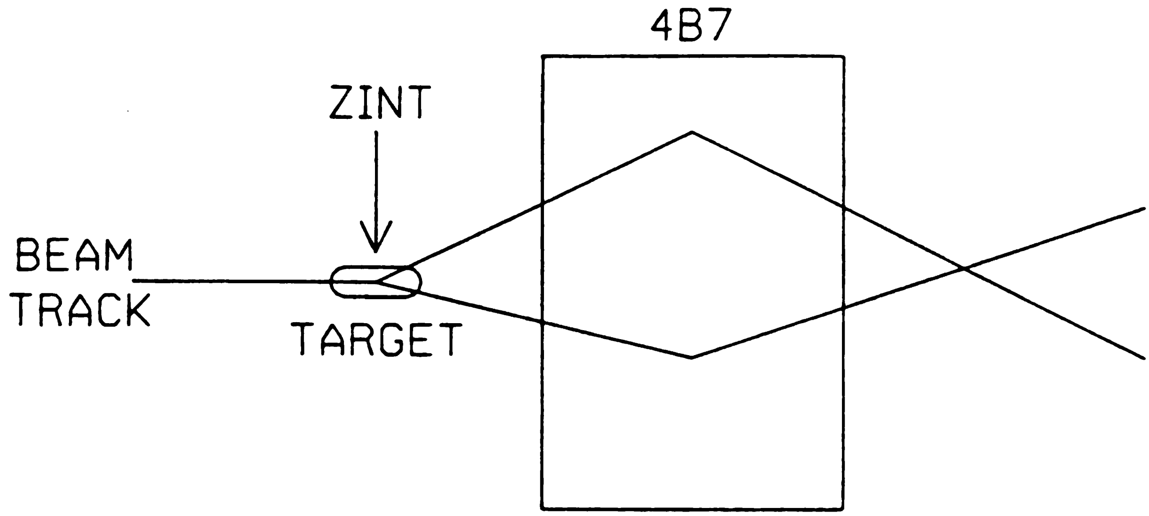

Figure 3-1. A Direct Interaction in the Target

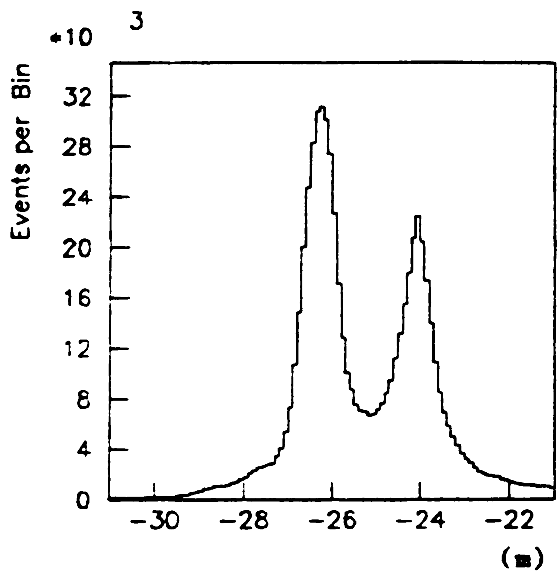

Figure 3-2. The Z of the Direct Interaction Vertex (Z_{INT})

The trajectory of the potential neutral particle was then reconstructed from each surviving pair of tracks. It was required to have a production vertex within the target. This vertex was defined as the point of closest approach between the beam track and the neutral particle trajectory. The distance of closest approach at the vertex (C_{Prod}) had to be less than 1.0 cm.

The three hypotheses

$$\Lambda \rightarrow p + \pi^-$$

$$\bar{\Lambda} \rightarrow \bar{p} + \pi^+$$

$$K^0_s \rightarrow \pi^+ + \pi^-$$

were then tested on the surviving candidates. Lambda and antilambda candidates were required to have

$$0.0 < P_\perp(\text{decay}) < 0.12 \text{ GeV/c},$$

while K^0_s candidates were required to have

$$0.12 < P_\perp(\text{decay}) < 0.21 \text{ GeV/c}.$$

Decay $P_\perp$ is defined as the transverse momentum of a decay particle with respect to its parent particle. Finally, invariant masses were required to be

$$1.104 < M_{\pi^-,p} < 1.128 \text{ GeV/c}^2 \quad (\Lambda)$$

$$1.104 < M_{\pi^+,\bar{p}} < 1.128 \text{ GeV/c}^2 \quad (\bar{\Lambda})$$

$$0.46 < M_{\pi^+,\pi^-} < 0.52 \text{ GeV/c}^2 \quad (K^0_s).$$

Because of the kinematical overlap between K^0_s and lambda decays (K^0_s and antilambdas), it would be possible for an event to satisfy two hypotheses. By setting the minimum decay $P_\perp$ for a K^0_s to 0.12 GeV/c, all such overlaps were decided in favor of the lambda (antilambda) hypothesis. This introduced a background of K^0_s's in the lambda and antilambda samples, which was corrected for later by using the Monte Carlo.

Finally, each event was required to be consistent with the trigger used during data taking. The beam track had to pass through each beam counter, but not through the H counter. None of the forward tracks was allowed to pass through the B_4 counter, while at least one of them was required to pass through an I counter. In addition, only one of the possible 16 PWC hits in the 2 track decay was allowed to be missing. This was a stricter requirement than what the trigger processor applied, and was used to eliminate the effect of noise on the triggering scheme (which was not modeled by the Monte Carlo).

Distributions of the variables used in the above analysis are shown in Figures 3-3 - 3-12. Included are comparisons to the results of the Monte Carlo (which will be described in Section 3.3.1). Figure 3-12 shows the invariant mass distributions obtained. They are all consistent with previous measurements, within the resolution of our system.

Table 3-1 gives a breakdown of the losses due to the cuts described above. It can be noted that most events failed due to more that one cut, and the largest single contributing cut was the one on the invariant masses, which eliminated only 4 % of the events. Only events passing all of these cuts will be used in the polarization analysis.

Table 3-1. Breakdown of Losses due to Cuts

Cuts Used	Events Lost (Fraction)
Z_{INT}, Mass, C_{Decay}	0.207
Z_{INT}, Mass	0.090
Z_{INT}, Mass, C_{Decay}, Z_{Prod}	0.084
Mass, Z_{Prod}	0.057
Mass	0.042
Mass, C_{Decay}, Z_{Prod}, C_{Prod}	0.038
Mass, Z_{Decay}, C_{Decay}, Z_{Prod}, C_{Prod}	0.033
Mass, Z_{Prod}, C_{Decay}	0.030
Mass, Z_{INT}, Z_{Prod}	0.020
Mass, Z_{INT}, C_{Decay}, Z_{Prod}, C_{Prod}	0.019
Z_{Prod}	0.019
Mass, Z_{INT}, C_{Decay}, C_{Prod}	0.016
Mass, Z_{Decay}, Z_{Prod}	0.020
Mass, C_{Decay}, Z_{Prod}, Z_{Decay}	0.019
Z_{INT}	0.006
Any other combination	< 0.001

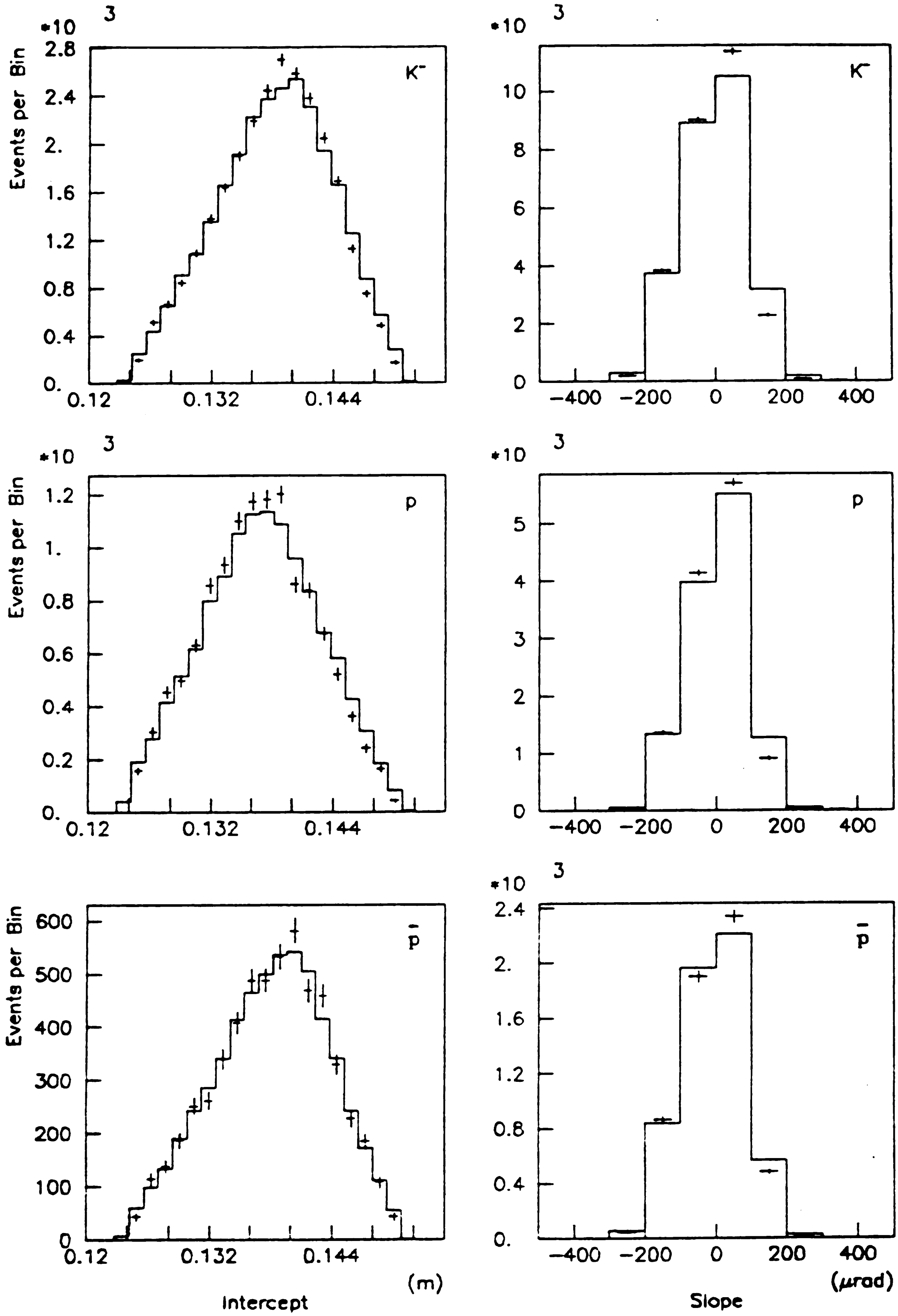

Figure 3-3. X Intercept and Slope of Beams at Target

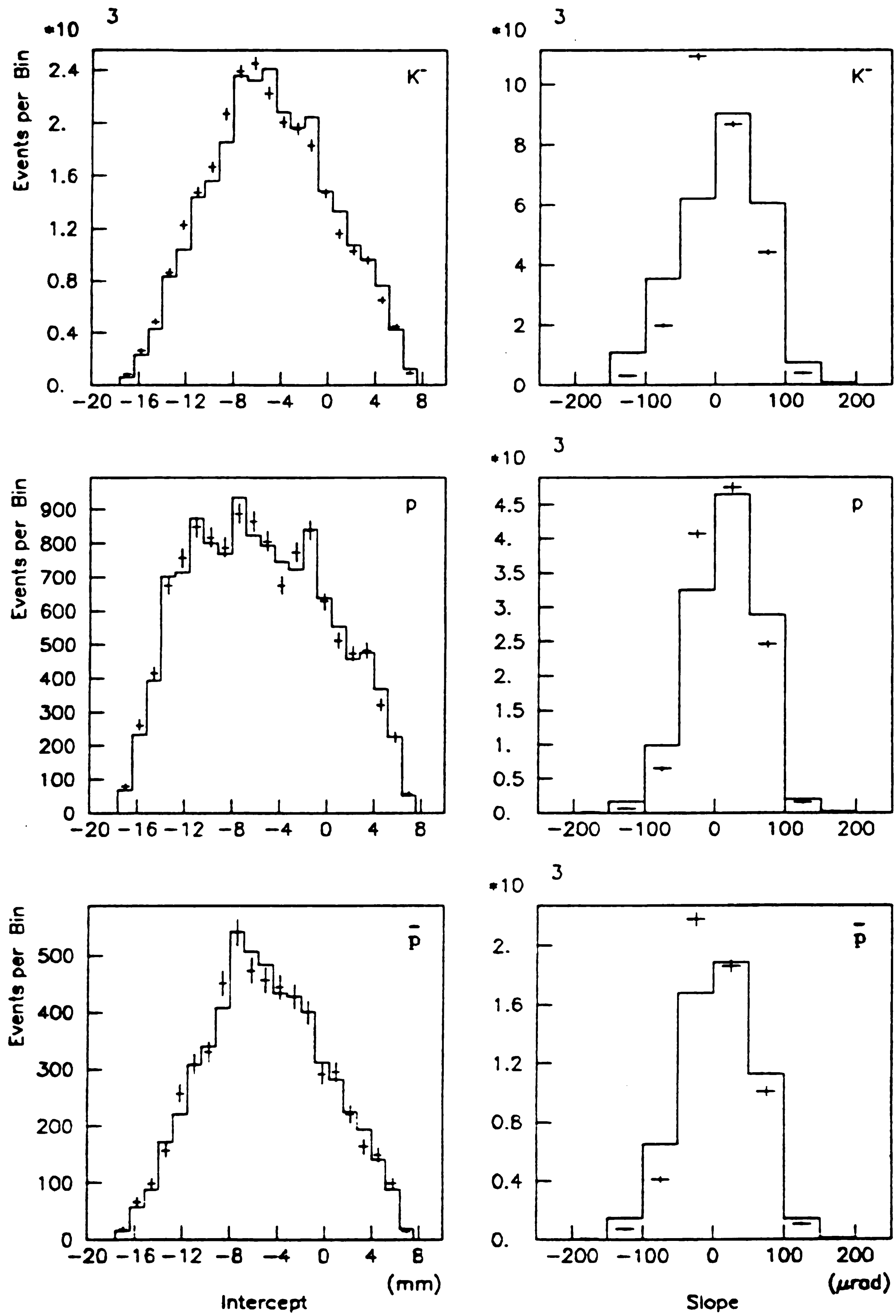

Figure 3-4. Y Intercept and Slope of Beams at Target

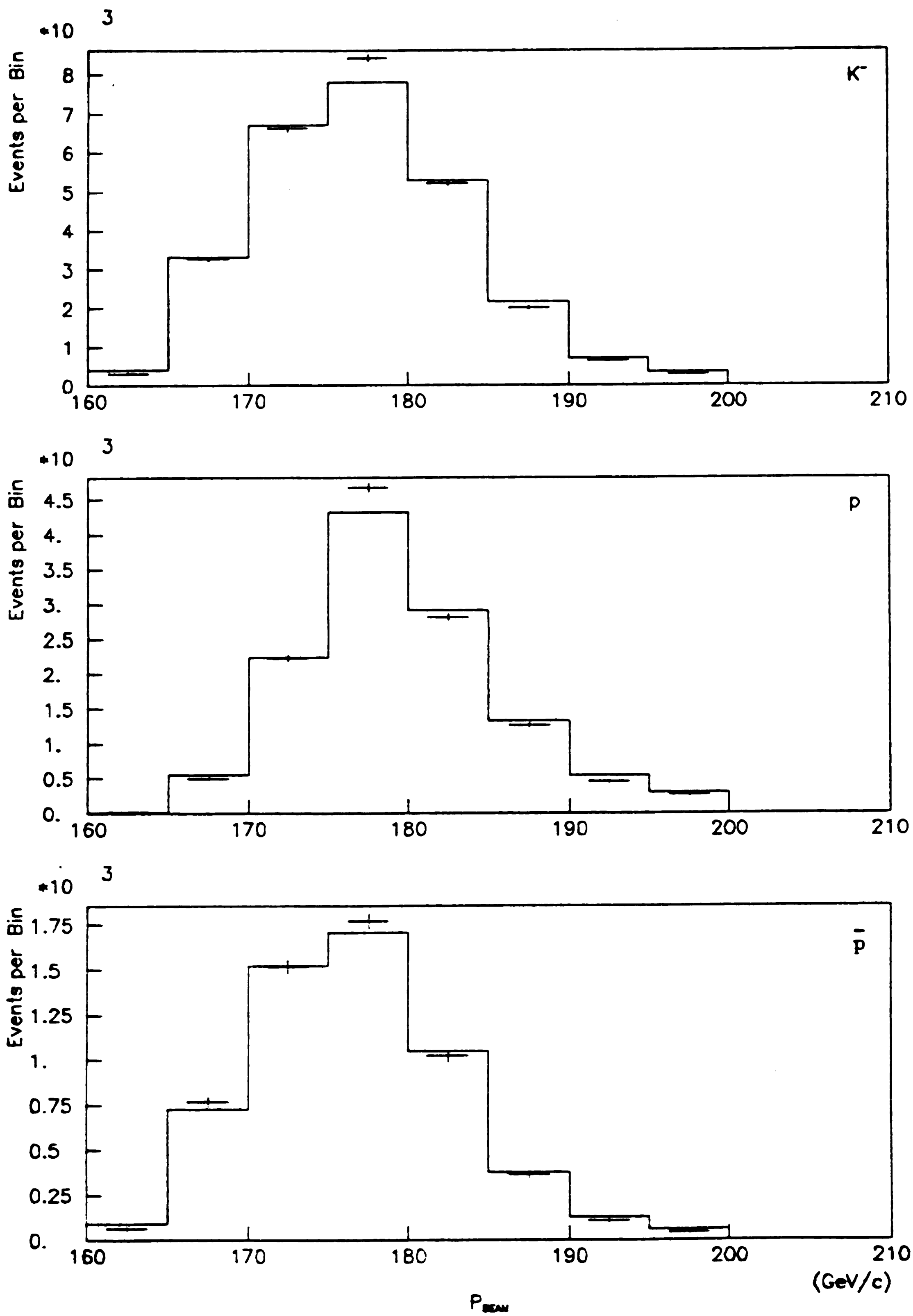

Figure 3-5. Momentum of Beams

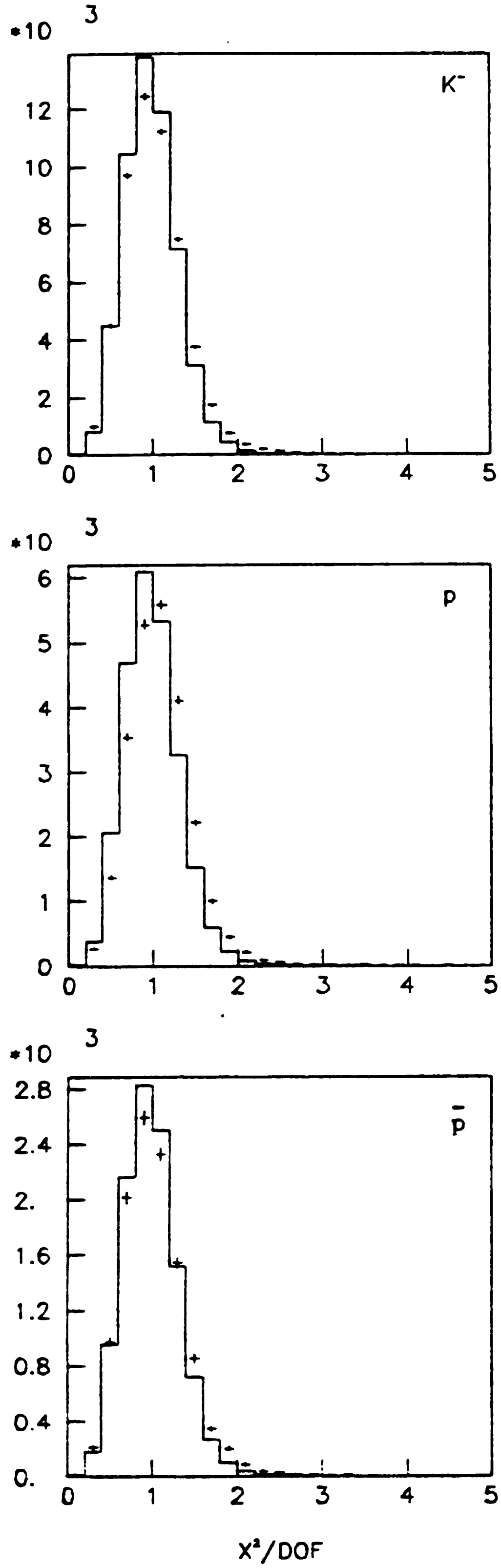

Figure 3-6. χ^2/DOF of Forward Tracks

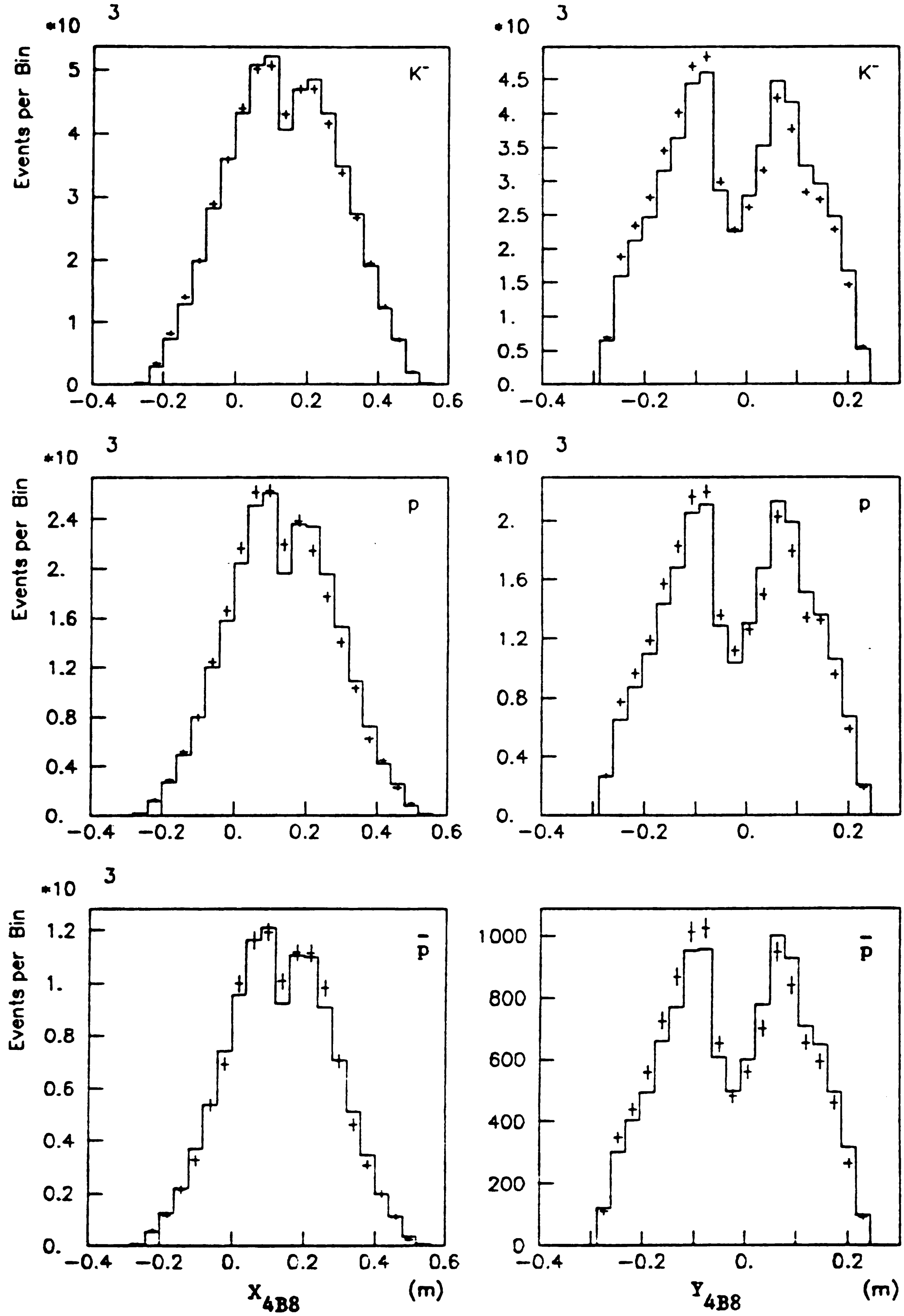

Figure 3-7. Track Intercepts at 4B8

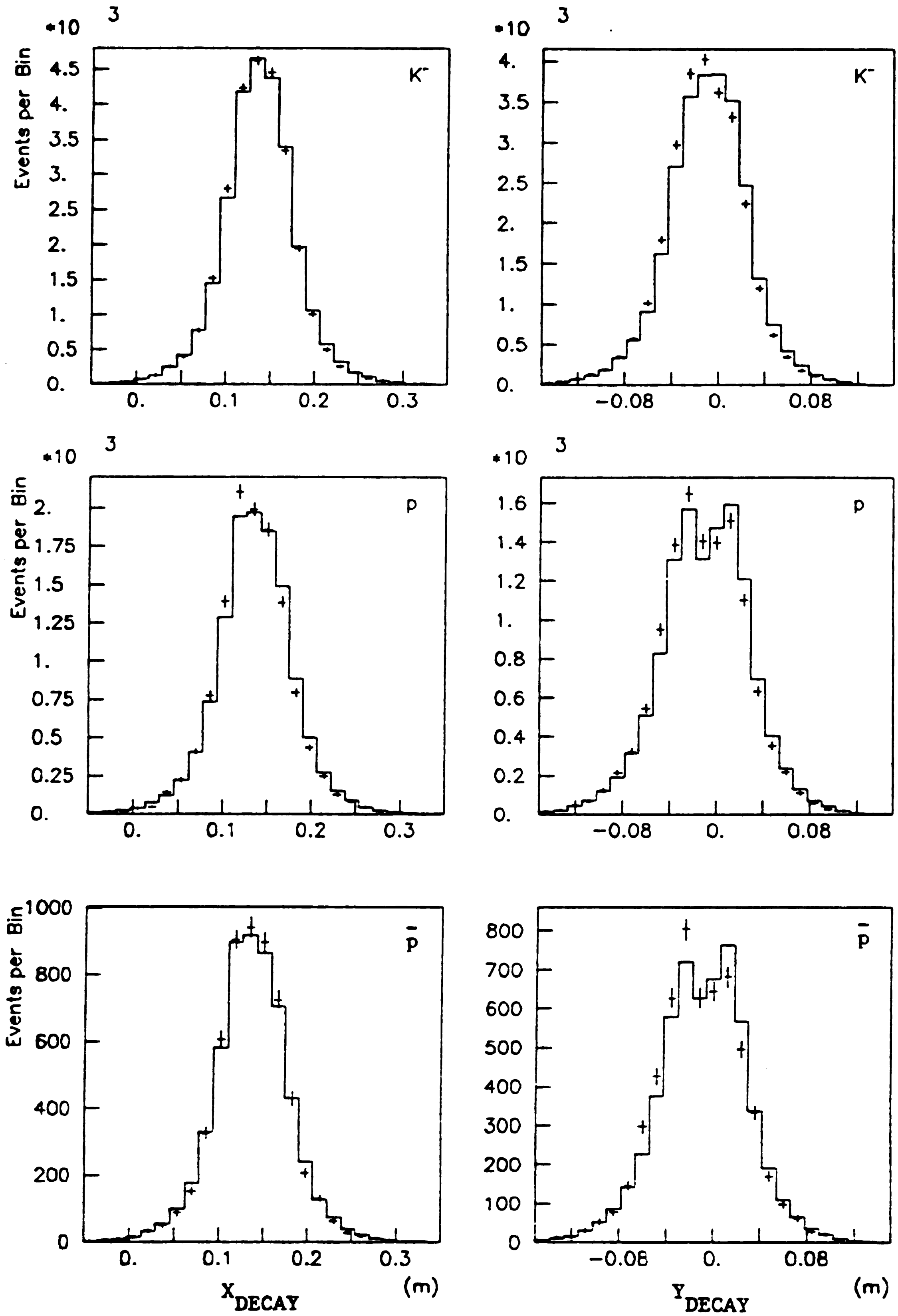

Figure 3-8. X and Y of the Decay Vertex

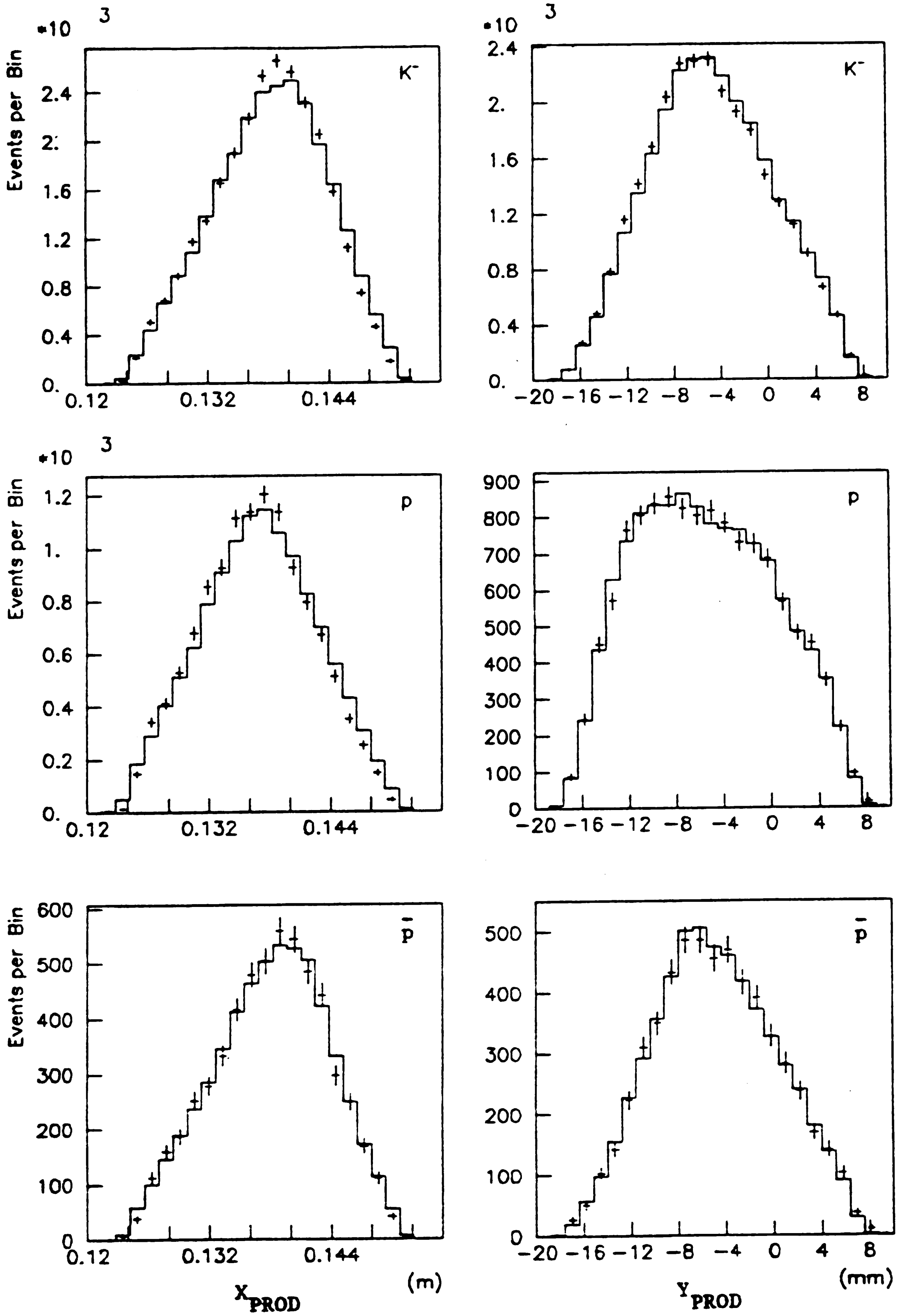

Figure 3-9. X and Y of the Production Vertex

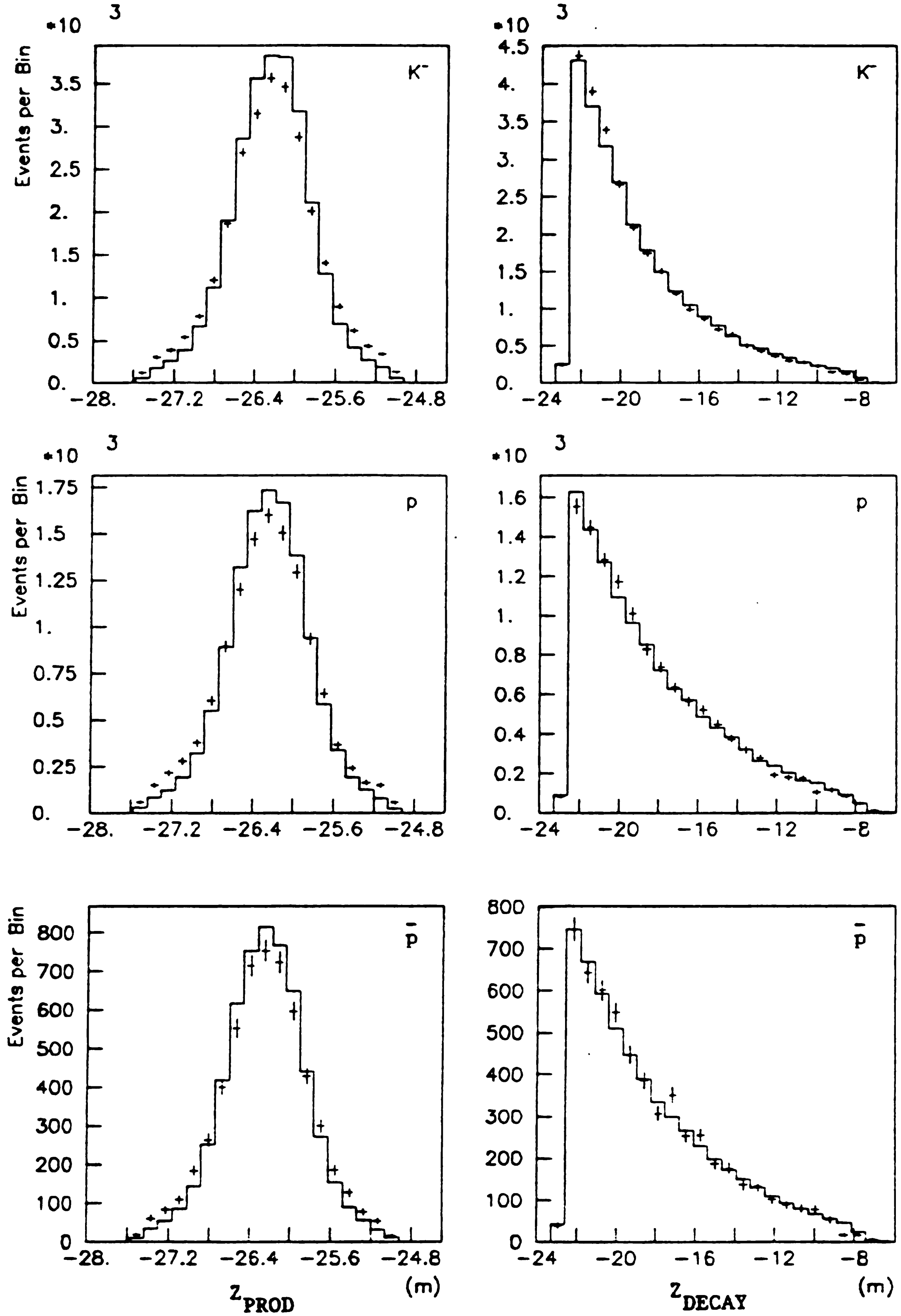

Figure 3-10. Z of Production and Decay Vertices

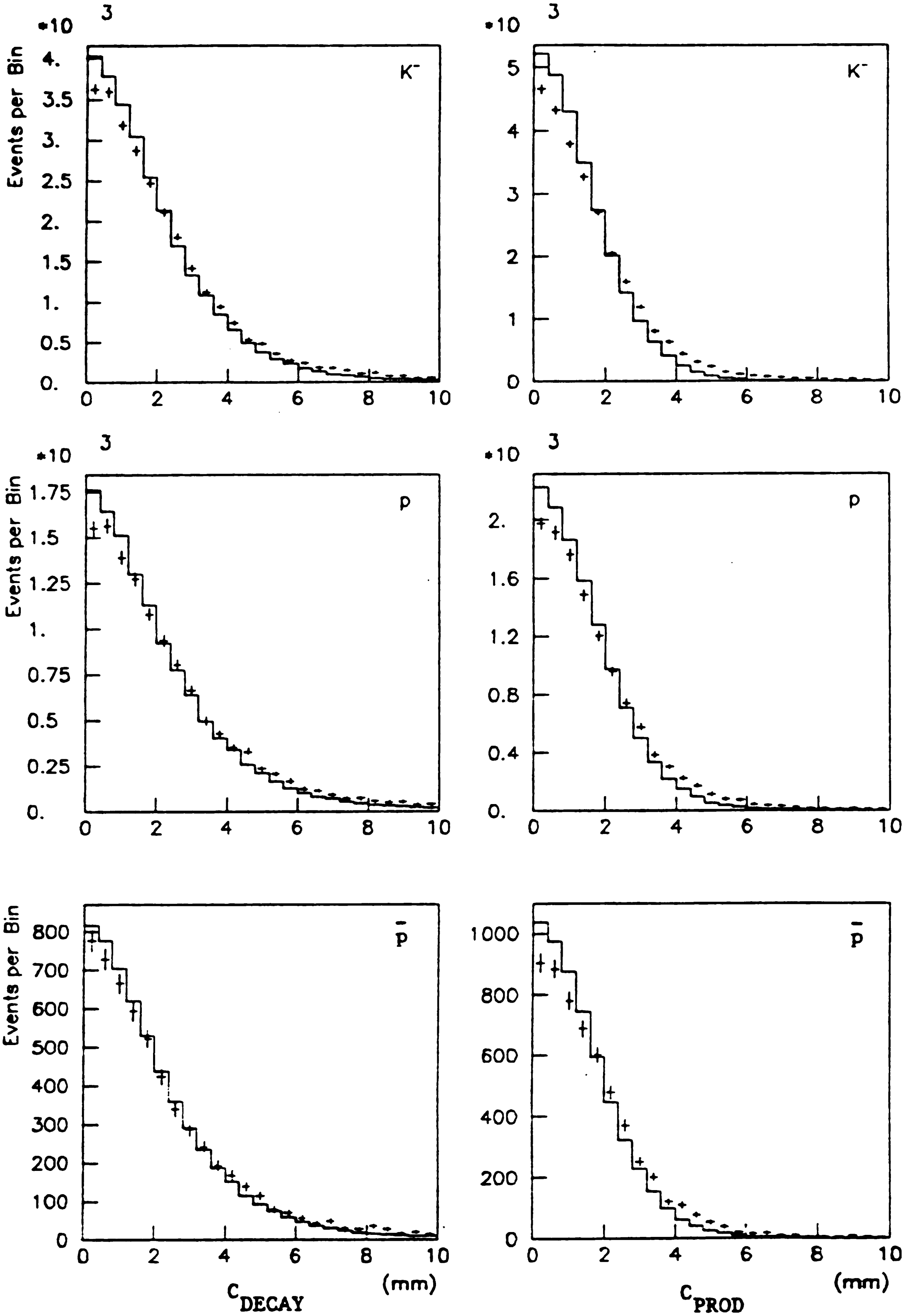

Figure 3-11. Distance of Closest Approach at Vertices

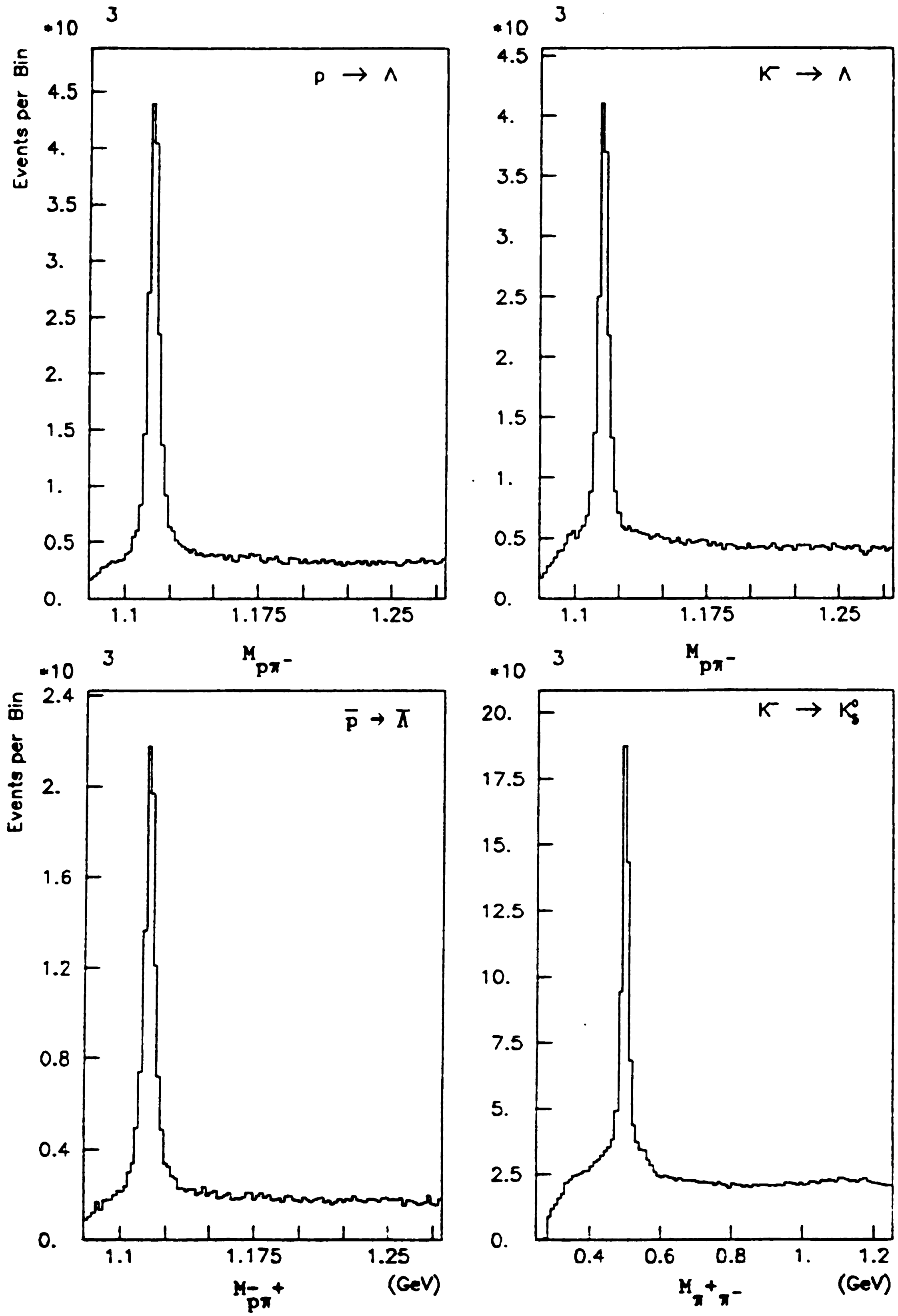

Figure 3-12. Invariant Masses before Cuts

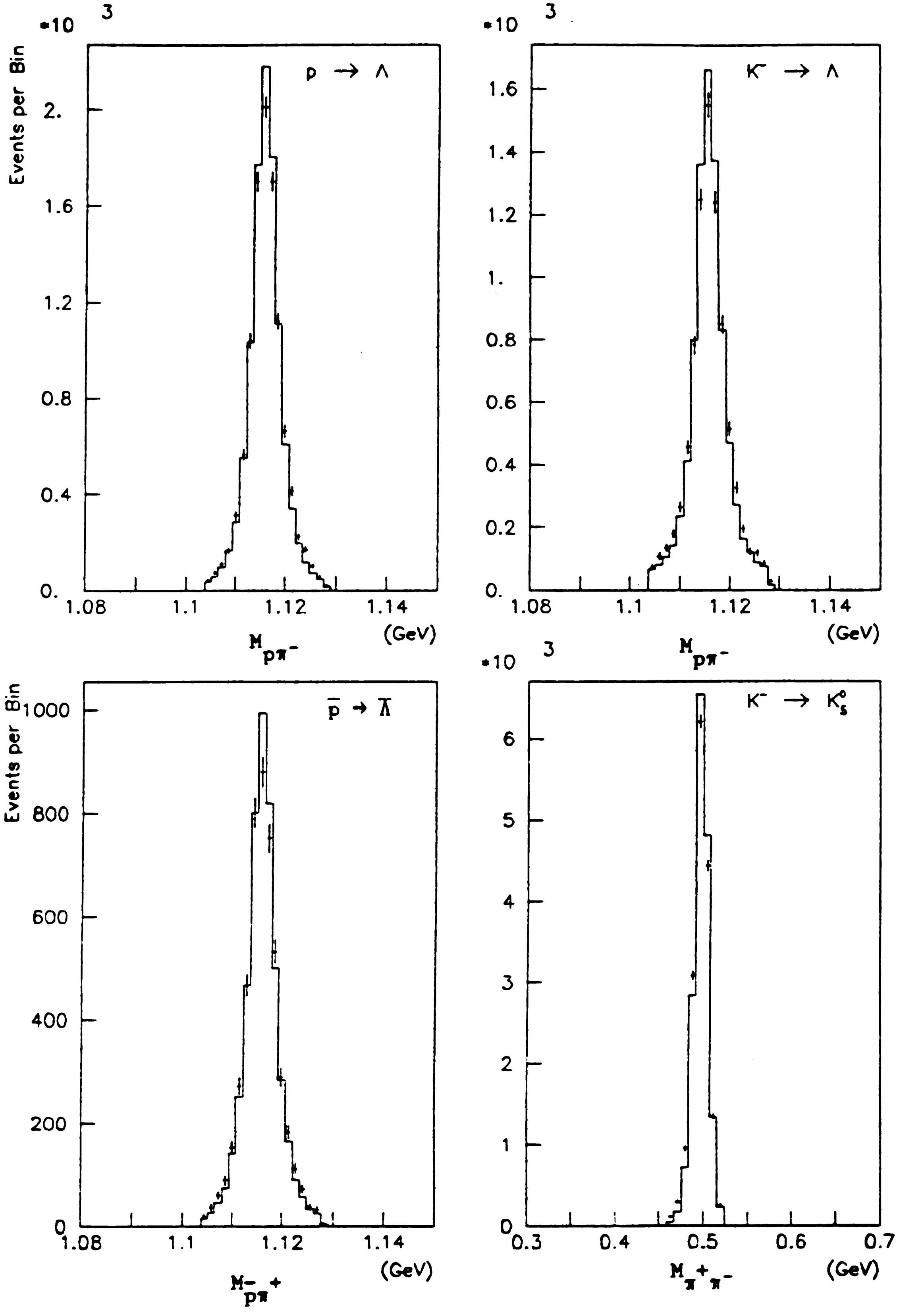

Figure 3-13. Invariant Masses after Cuts

3.3 Polarization Analysis

A summary of the final event sample coming from the data reduction phase is given in Table 3-2. This sample was used in the polarization analysis.

Table 3-2. Summary of the Final Event Sample

Channel	Number of Events
$p \rightarrow \Lambda$	10,480
$\bar{p} \rightarrow \bar{\Lambda}$	4,800
$K^- \rightarrow \Lambda$	8,250
$K^- \rightarrow K^0_s$	16,685

As described in Section 1.3, the polarization of a sample of lambdas can be related to the angular distribution of the pions from their decays. Expanding Equation 1-1, we have

$$\frac{dN}{d\Omega} = \frac{1}{4\pi} \left(1 + \alpha_\Lambda \left[P_X \sin\theta \cos\phi + P_Y \sin\theta \sin\phi + P_Z \cos\theta \right] \right)$$

where P_X, P_Y and P_Z are the components of the polarization vector $\vec{P}$, and θ and ϕ are the azimuthal and polar angles of the pion in the center of mass frame of the lambda (Figure 3-14). This distribution must now be modified to accommodate the limited acceptance of the experiment, the finite resolution of the apparatus, and the effects due to the background of K^0_s's in the Λ and $\bar{\Lambda}$ samples.

The new distribution becomes

$$\frac{dN'}{d\Omega} = A(\theta,\phi)\,\frac{dN}{d\Omega}$$

where $A(\theta,\phi)$ is the total correction to the raw distribution. In order to extract the polarization from this distribution, we must determine the function $A(\theta,\phi)$. This is the role of the Monte Carlo.

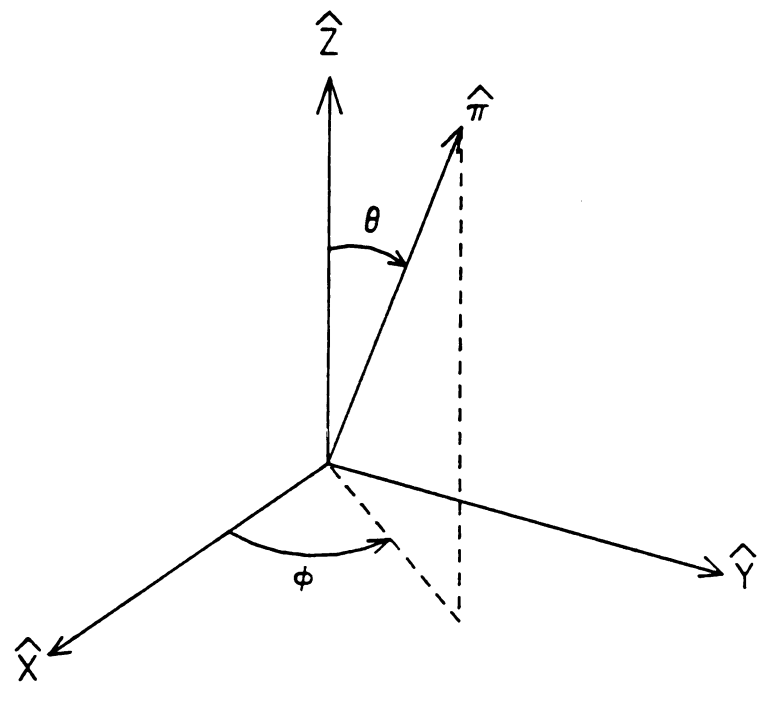

Figure 3-14. Center of Mass Coordinate System.

3.3.1 Monte Carlo

The Monte Carlo program attempted to simulate the behavior of the experiment by modeling the production of particles from a given incoming beam, the behavior of those particles after production and the response of the apparatus to those particles. This was accomplished by a computer program that was divided up into several parts - beam particle generation and tracking, primary particle production and tracking, primary particle decay, decay particle tracking and apparatus response to these various particles. Each of these parts will now be described.

In general, six parameters are required to define the phase space of the beam. We chose as these parameters the momentum of the beam, and its X and Y intercepts and slopes at the first beam chamber (i.e., P_{Beam}, X_0, Y_0, X_0', Y_0', $Z_0 = Z_{B1X}$). The problem of generating the beam phase space is thus equivalent to generating P_{Beam}, X_0, Y_0, X_0', Y_0' at Z_0, remembering to include all possible correlations. To accomplish this, the data was divided up into several momentum ranges, and X_0 vs. X_0' and Y_0 vs. Y_0' plots were generated for each range. The Monte Carlo used the measured momentum spectrum to generate P_{Beam}, and then used the appropriate X_0-X_0' and Y_0-Y_0' plots to generate the remaining variables. The generated beam particle was then tracked through the two beam magnets (4B5 and 4B6), until it got to the target. The K^-, p and $\bar{p}$ beams were handled independently.

The next step in the Monte Carlo was the simulation of the interaction of the beam with the target. Several simplifications were made here. Only one neutral particle was produced per incident beam particle, and that particle was either a Λ, $\bar{\Lambda}$ or K^0_s. The relative probability of generating a Λ, $\bar{\Lambda}$ or K^0_s in the Monte Carlo was adjusted until the reconstructed decay $P_\perp$ distributions matched the data. Figure 3-15 shows the decay $P_\perp$ distributions for events not consistent with the lambda hypothesis and events not consistent with the antilambda hypothesis. These plots allow the determination of the $\bar{\Lambda}/K^0_s$ and Λ/K^0_s ratios respectively. The momentum and production $P_\perp$ of the given particle were generated according to distributions that were adjusted empirically until the reconstructed distributions matched the data (Figure 3-16 and Figure 3-17). No attempt was made to fit these production distributions.

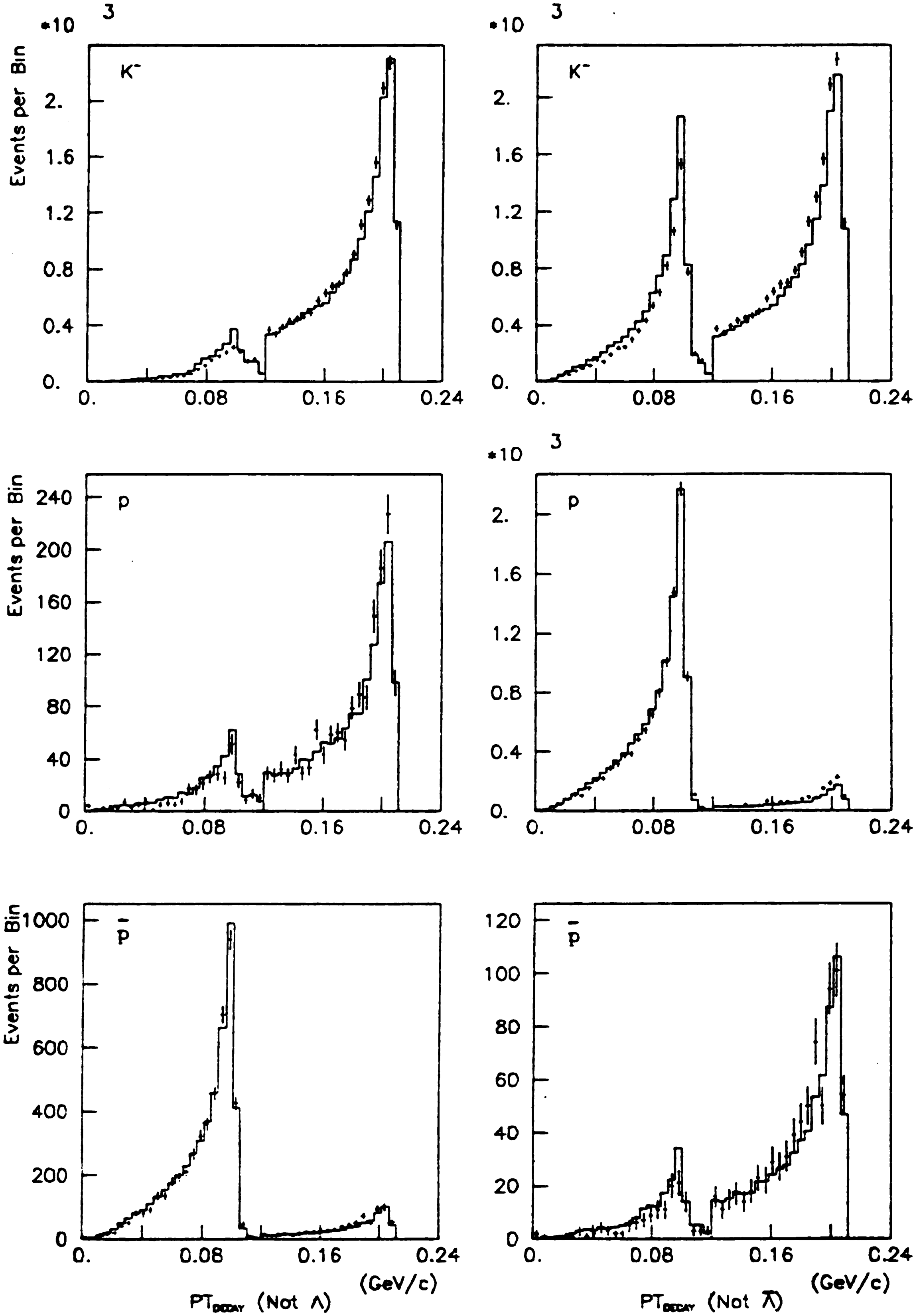

Figure 3-15. Decay $P_{\perp}$ Distributions

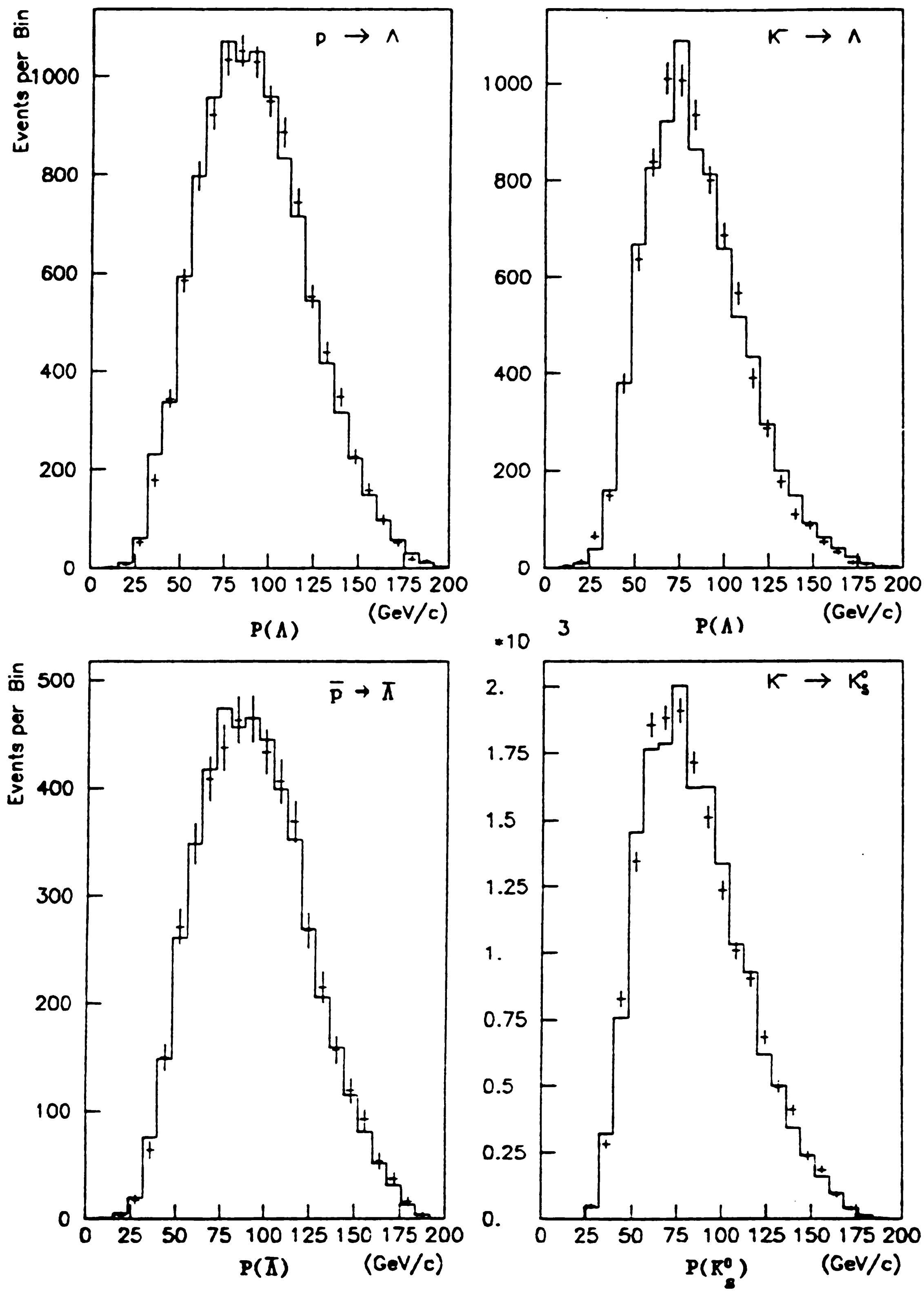

Figure 3-16. Momentum of $\Lambda, \bar{\Lambda}, K_s^0$

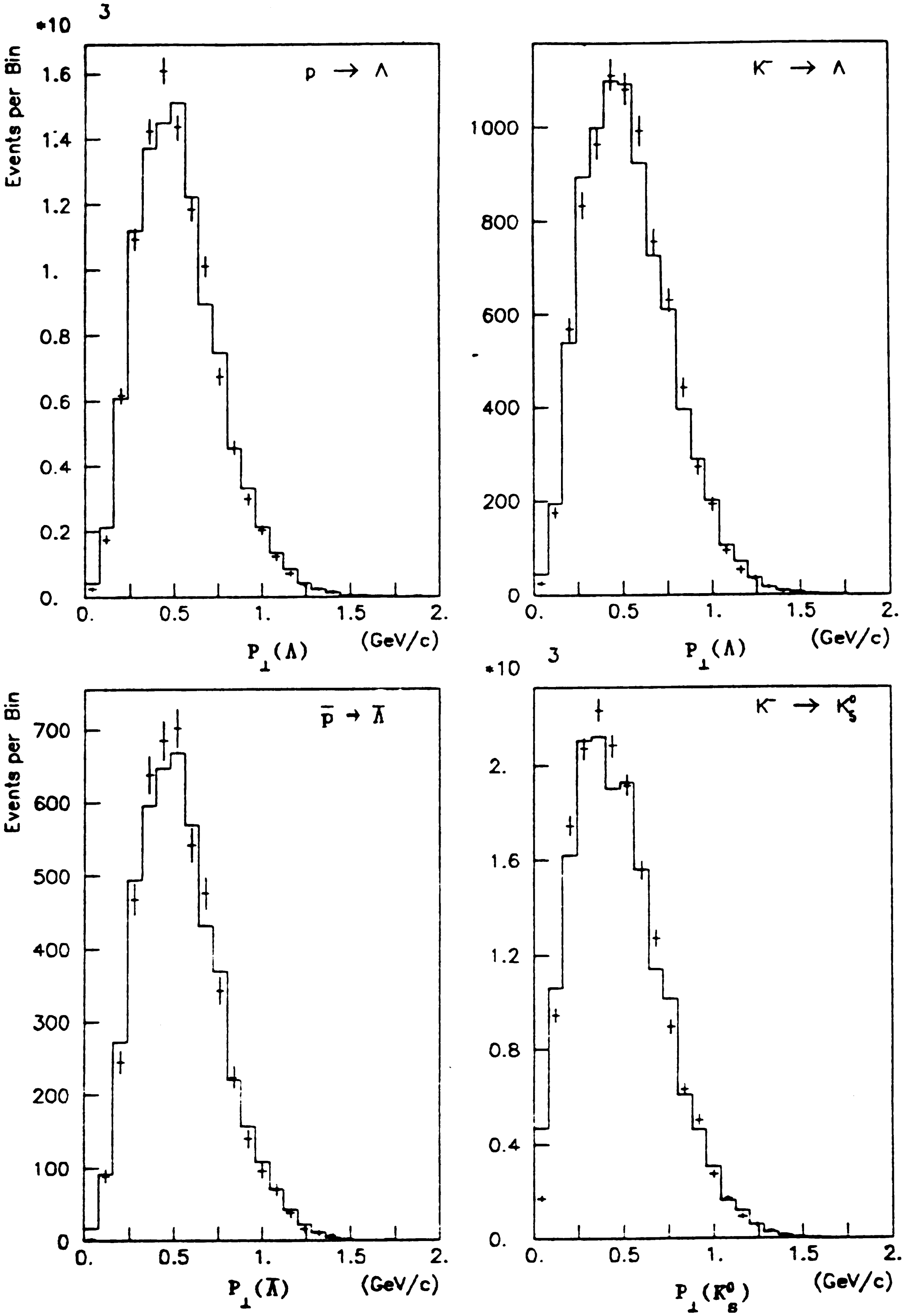

Figure 3-17. $P_\perp$ of $\Lambda, \bar{\Lambda}, K^0_s$

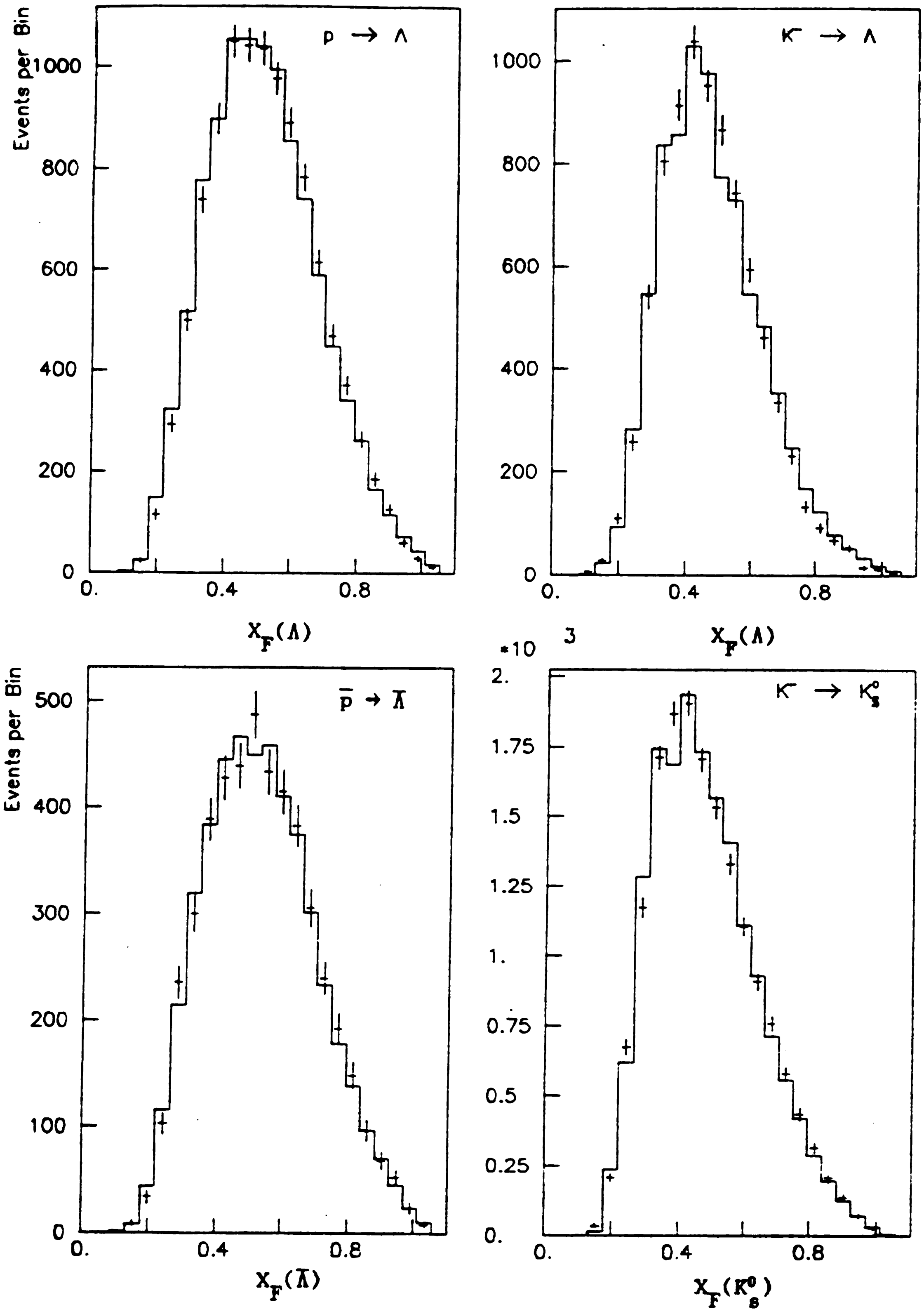

Figure 3-18. X_F of $\Lambda, \bar{\Lambda}, K_s^0$

The produced particle was then tracked through the apparatus, until it decayed. Lambdas and antilambdas decayed exponentially, with $c\tau = 7.89$ cm. The K^0_s decay distribution was an exponential with $c\tau = 2.675$ cm, modified by $K^0_s - K^0_L$ mixing. The only decay modes generated were

$$\Lambda \rightarrow p + \pi^-$$
$$\bar{\Lambda} \rightarrow \bar{p} + \pi^+$$
$$K^0_s \rightarrow \pi^+ + \pi^-.$$

K^0_s decays were generated isotropically in their rest frame. Lambdas and antilambdas were allowed to have a polarization, which was an input to the program. Initially, the lambdas and antilambdas were unpolarized in the Monte Carlo. The data was analyzed with this unpolarized model. The polarization results from this analysis were then put into the Monte Carlo, and the analysis was repeated. It was found that the results did not depend on the polarization models used.

If a lambda or antilambda passed through the sweeper magnet, its spin was precessed. The amount of precession was determined by the $\int B\, dl$ the particle experienced, and the orientation of the spin with respect to the field direction. The ramping effect of the sweeper discussed in Section 2.4 was included.

The generated decay products were then tracked through the rest of the apparatus. Moliere multiple scattering [40] of the particles was included, as was pion decay. The response of the apparatus to these particles was then modeled.

The PWC's were assumed to have 2 mm wire spacing (1 mm for the beam chambers) throughout each chamber. The wire closest to a particle's traversal was considered hit. In addition, if a particle went into a region half way between two wires, both wires were considered hit. The size of this sharing region was determined from the rate of adjacent wire hits in the data. With this procedure, the resolutions of the PWC's in the Monte Carlo matched those of the data. For the efficiency of the PWC's, the chambers were divided up into 3 separate regions - the support string region (100 % inefficient), the central beam region (~ 73 % efficient) and the rest of the chamber (~ 96 % efficient). Each chamber was handled independently.

For the drift chamber system, each wire was handled independently. The location, efficiency and resolution for each wire was obtained from the alignment data. The resolution was modeled by simply doing a Gaussian smearing of the track intercept in the chamber. Also included were the deadened central regions of the drift chambers.

Monte Carlo events were only considered if they would have triggered the experiment. At least one of the two decay particles was required to pass through an I counter. During data taking, the trigger processor required at least 2 hits in 7 out of the 8 PWC's, and at least 1 hit in the other PWC. However, these hits did not have to belong to the tracks from the Λ, $\bar{\Lambda}$ or K^0_s decay. The distribution of the number of PWC hits in these decays is shown in Figure 3-19. The Monte Carlo events were generated with this distribution.

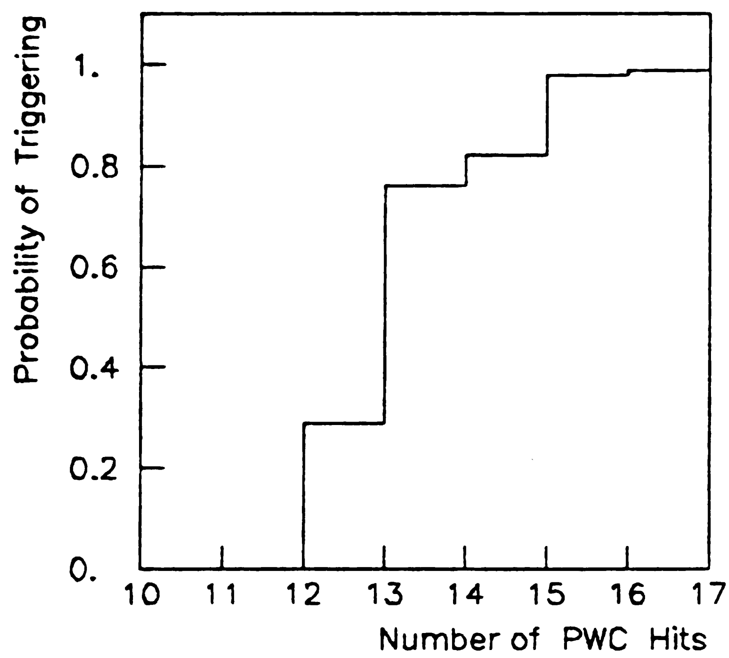

Figure 3-19. Number of PWC Hits in Λ, $\bar{\Lambda}$, K^0_s Events

The Monte Carlo events were written onto tape with the same format as the data events, were processed through the same pattern recognition program, and were required to pass the same cuts as described in Section 3.2. Comparisons of the Monte Carlo and the data have been shown in Figures 3-3 - Figure 3-18. Excellent agreement was obtained.

3.3.2 Calculation of Polarization

By using the Monte Carlo, the function $A(\theta,\phi)$ described in Section 3.3 can in general be calculated. It is simply the number of events reconstructed after all cuts with a given θ and ϕ, divided by the number of events generated with that θ and ϕ.

$$A(\theta,\phi) = \frac{N_{Rec}(\theta,\phi)}{N_{Gen}(\theta,\phi)}$$

It is convenient to convert these continuous functions into discrete functions by binning over θ and ϕ. This is done by integrating over bins of solid angle $\Delta\Omega$, and yields

$$A(\theta_i,\phi_j) = \frac{\int_{\Delta\Omega} N_{Rec}(\theta,\phi)\ d\Omega}{\int_{\Delta\Omega} N_{Gen}(\theta,\phi)\ d\Omega}$$

$$\frac{\Delta N'}{\Delta\Omega} = A(\theta_i,\phi_j) \int_{\Delta\Omega} \frac{dN}{d\Omega}(\theta,\phi) \qquad (3\text{-}1)$$

which are now functions of the binning.

In general, $\Delta N'/\Delta\Omega$ is a function of other variables as well, such as $P_\perp$, X_F, etc.. However, statistical error considerations require the data be analyzed only as a function of a limited number of these variables. To measure P_X, P_Y and P_Z simultaneously, θ and ϕ are required. Previous measurements indicate that the polarization is a function of $P_\perp$ and X_F, and thus they should be included. The limited statistics of the data constrain the analysis to either $P_\perp$ or X_F, and effectively eliminates the possibility of including any other variables in the analysis. It is believed that all suppressed variables have been correctly modeled by the Monte Carlo, and thus integrating over them to calculate $A(\theta,\phi)$ should be correct as well.

In order to use Equation 3-1, we must define the coordinate system in Figure 3-14. Our choice is motivated by noting that parity is conserved when Λ and $\bar{\Lambda}$'s are strongly produced. This implies that their spins must be perpendicular to the production plane, and thus their polarizations must also be perpendicular to the production plane. To utilize this, the coordinate system was defined such that the Z axis was normal to the production plane and the X and Y axes were in the plane. In particular,

$$\hat{z} = \frac{\vec{P}_{\Lambda} \times \vec{P}_{Beam}}{|\vec{P}_{\Lambda} \times \vec{P}_{Beam}|}$$

$$\hat{x} = \frac{\hat{z} \times \hat{z}_{Lab}}{|\hat{z} \times \hat{z}_{Lab}|}$$

$$\hat{y} = \frac{\hat{z} \times \hat{x}}{|\hat{z} \times \hat{x}|} .$$

With this definition, Λ and $\bar{\Lambda}$ spins must be in the $\pm\hat{z}$ direction. Since the Λ's and $\bar{\Lambda}$'s have non-zero magnetic moments, their spins will precess as they pass through the sweeper magnet. The amount of precession is determined by the magnitude of the field, and the orientation of the spin with respect to the field. Assuming the magnetic moment of the Λ is

$$\mu_{\Lambda} = (-0.6138 \pm 0.0047)\ \mu_N$$ [41],

the precession angle is

$$\phi_p = -0.19604 \int B\, dl \sin\theta \ (\mathrm{rad/Tm})$$

where $\int B\, dl$ is the field integral of the sweeper, and θ is the angle between the spin and the field direction. The maximum precession angle in this experiment was $\phi_p = 29°$. During the analysis, the coordinate system was precessed by ϕ_p, and calculated for each event. The pion in the decay was then boosted into this frame, and the pion angular distribution was fit to Equation 3-1. Appendix III gives a detailed description of this fit.

CHAPTER 4

Results and Conclusions

4.1 Bias Studies

Since the determination of a polarization involves the measurement of an asymmetry in a decay distribution, it is important that no apparatus induced asymmetries be present. Although we believe we have modeled our apparatus correctly, it is useful to make independent checks of this. Four such tests have been performed.

The first is a measurement of the lifetimes of the Λ, $\bar{\Lambda}$ and the K^0_s. These measurements are sensitive to the longitudinal acceptance of the experiment. They were obtained by fitting the decay length distributions to exponentials, correcting for acceptance by using the Monte Carlo. The average results are listed in Table 4-1. They were found to be independent of momentum, and are in good agreement with previously measured values.

Table 4-1. Measured Lifetimes of Λ, $\bar{\Lambda}$, K^0_s

Particle	Lifetime	World Average
Λ	$(2.60\pm0.07) \times 10^{-10}$ sec	$(2.6320\pm0.0200) \times 10^{-10}$ sec
$\bar{\Lambda}$	$(2.44\pm0.11) \times 10^{-10}$ sec	
K^0_s	$(0.87\pm0.01) \times 10^{-10}$ sec	$(0.8923\pm0.0022) \times 10^{-10}$ sec

The second test is a measurement of the K^0_s decay asymmetry. Since the K^0_s has spin zero, it must be unpolarized, and thus its decay must be totally symmetric. The procedure followed to obtain the K^0_s asymmetry was identical to that for the lambda and antilambda (with the exception that there was no precession of the coordinate system in the sweeper). Here, the π^- angular distribution was fit to

$$\frac{dN}{d\Omega} = \frac{1}{4\pi}\left(1 + \vec{A} \cdot \hat{\pi} \right),$$

where $\vec{A}$ is the asymmetry. Only K^0_s's produced by the K^- beam were used. The results are shown in Figure 4-1. They are consistent with zero. Although the K^0_s asymmetry measurements are a stronger test for biases than the lifetimes are, the kinematic differences between a K^0_s and a Λ or $\bar{\Lambda}$ implies the K^0_s can not cover all possible sources of apparatus induced signals for Λ or $\bar{\Lambda}$'s.

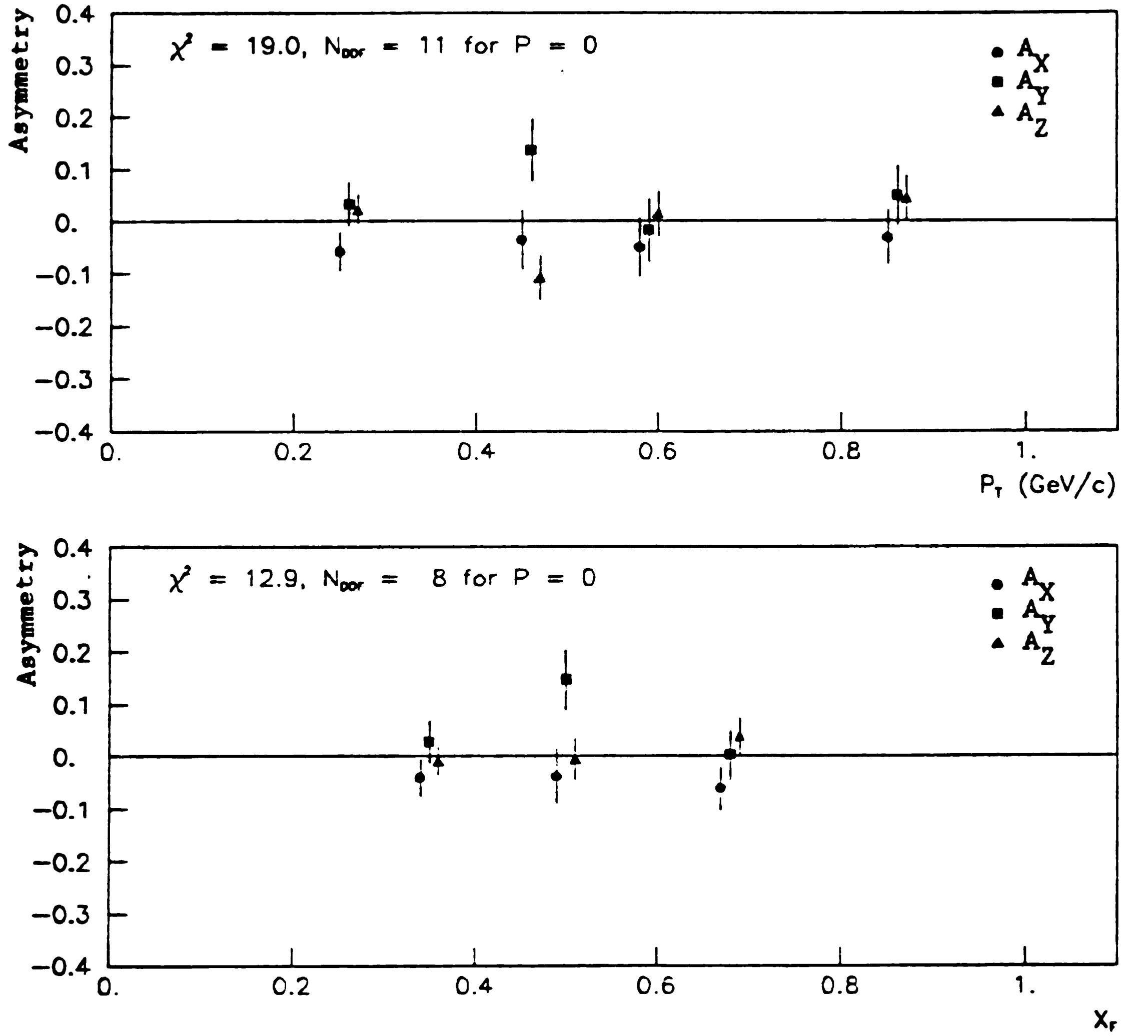

Figure 4-1. Decay Asymmetry of K^0_s from $K^- \to \bar{K}^0_s$

A stronger check for these channels is obtained by the parity conservation requirement for Λ and $\bar{\Lambda}$ polarizations. This requires the X and Y polarizations to be zero. The X and Y results obtained for the channels $p \to \Lambda$, $\bar{p} \to \bar{\Lambda}$ and $K^- \to \Lambda$ are shown in Figure 4-2 and Figure 4-3. All are consistent with zero.

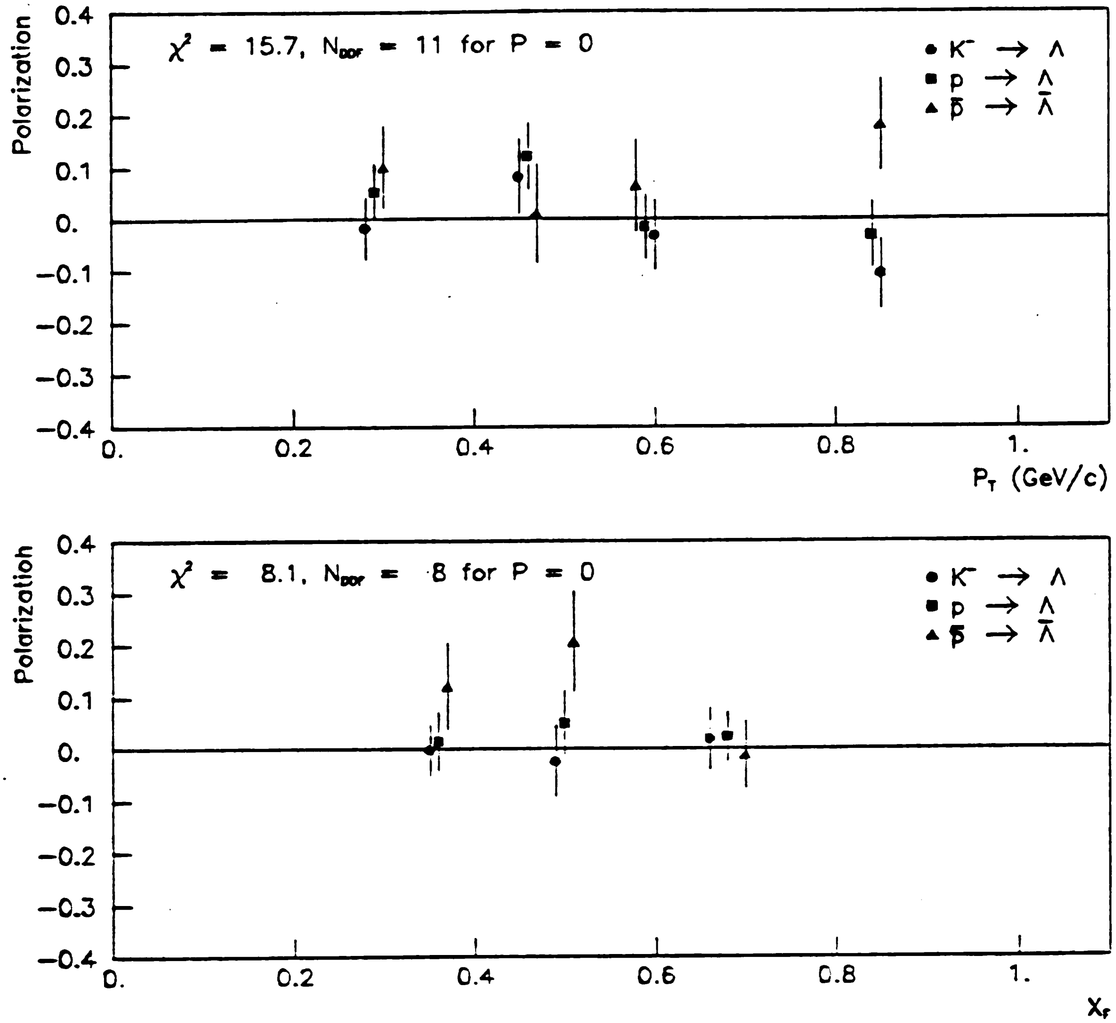

Figure 4-2. X Polarization for $p \to \Lambda$, $\bar{p} \to \bar{\Lambda}$ and $K^- \to \Lambda$

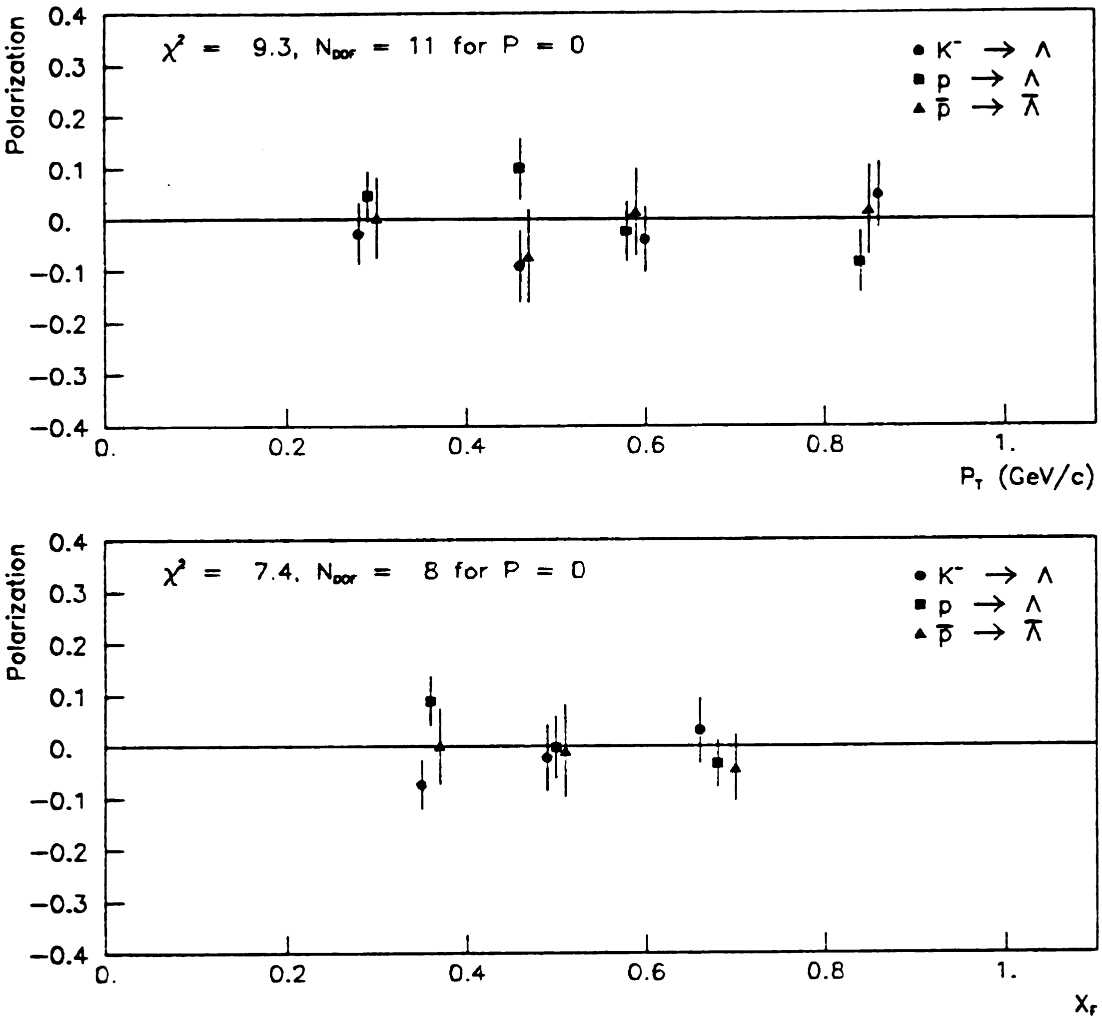

Figure 4-3. Y Polarization for $p \to \Lambda$, $\bar{p} \to \bar{\Lambda}$ and $K^- \to \Lambda$

Finally, a standard procedure, used in several of the previous polarization experiments, of flipping the direction of the magnetic fields in the sweeper and analysis magnet was performed. This is especially useful for fixed production plane experiments, where by combining magnet up and magnet down data, apparatus induced biases can be made to cancel. For this experiment, the production plane varied event by event, and the bias cancelling procedure could not be used. The main effect of reversing the fields in this experiment was to change the area of the downstream two stations that were sampled by the protons and pions from the Λ, $\bar{\Lambda}$ and K^0_s decays. Reversing the fields therefore primarily measured whether the downstream acceptance of the experiment was modeled correctly. The differences between magnet up and magnet down polarization results are shown in Figure 4-4. They are consistent with zero. All other polarization results presented are for combined up and down data.

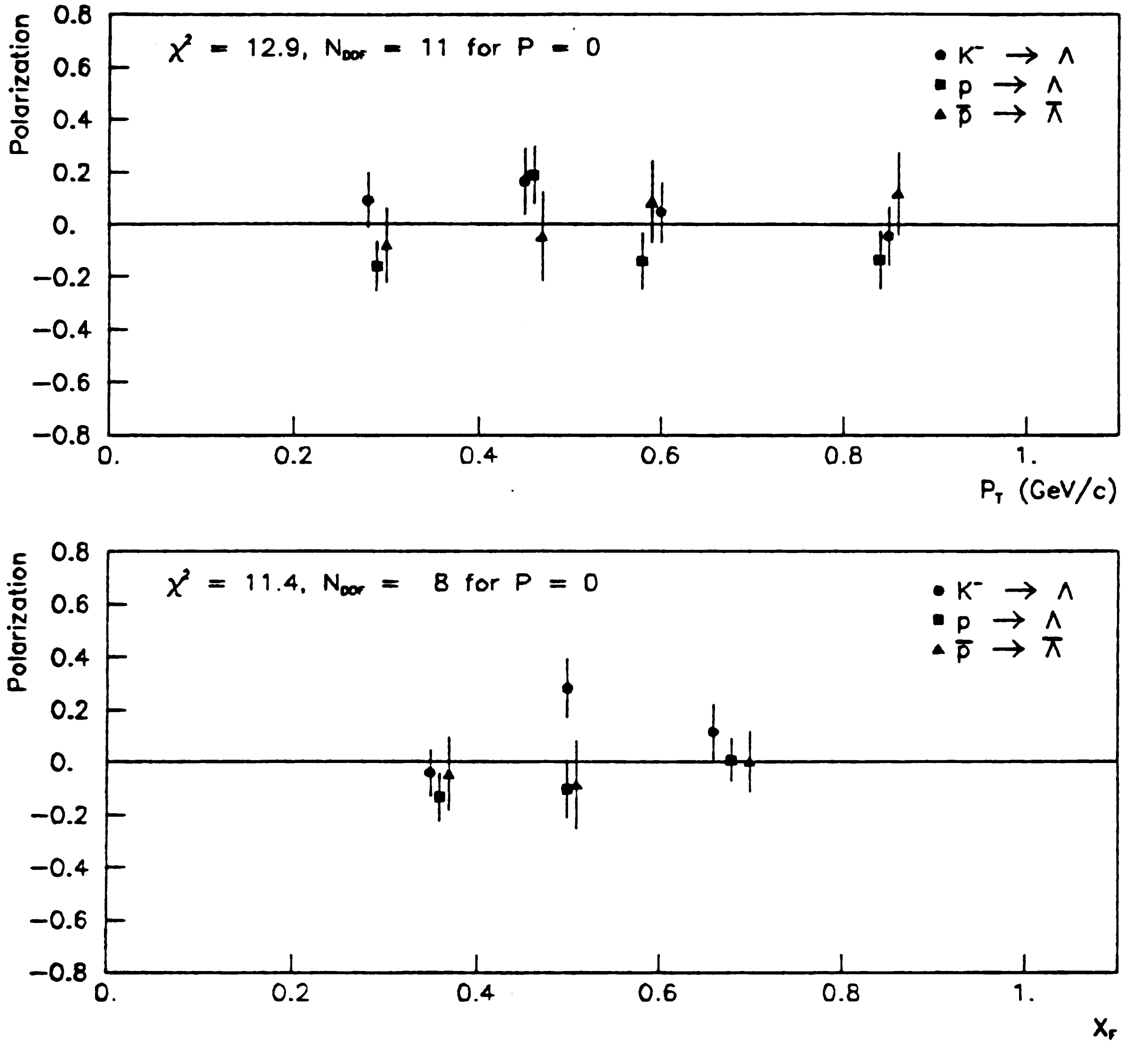

Figure 4-4. P_z (Up - Down) for $p \rightarrow \Lambda$, $\bar{p} \rightarrow \bar{\Lambda}$ and $K^- \rightarrow \Lambda$

The above tests yield results consistent with zero systematic bias, within the level of our statistics. However, there can still be systematic errors in the Z polarizations of the Λ and $\bar{\Lambda}$'s. A discussion of these errors will follow the presentation of the polarization results.

4.2 Polarization Results

The polarization results for the channels $p \rightarrow \Lambda$, $\bar{p} \rightarrow \bar{\Lambda}$ and $K^- \rightarrow \Lambda$ are listed in Table 4-2 - Table 4-4, and are shown in Figure 4-2 - Figure 4-4. The data have been binned both in $P_\perp$ and X_F. The assumptions made in the analysis that define the sign of the polarization were

$$\alpha_\Lambda = -0.642 \pm 0.013$$

$$\alpha_{\bar{\Lambda}} = -\alpha_\Lambda$$

$$\frac{dN}{d\Omega} = \frac{1}{4\pi}(1 + \alpha P \cos\theta)$$

where θ is the angle between the pion and the production plane normal in the center of mass. Finally, the production plane normal was defined as

$$\hat{z} = \frac{\vec{P}_\Lambda \times \vec{P}_{Beam}}{|\vec{P}_\Lambda \times \vec{P}_{Beam}|} .$$

The data presented here include both directly produced lambdas and antilambdas, and those produced indirectly (such as from radiative decays of Σ^0's). A discussion of the contribution to the polarization results from such non-prompt sources is contained in Section 4.3.

Table 4-2. Polarization Results for $p \rightarrow \Lambda$

$P_{\perp}$ Bin	$\langle P_{\perp} \rangle$	$\langle X_F \rangle$	P_Z
0.00 - 0.40	0.29	0.42	-0.012±0.047
0.40 - 0.52	0.46	0.50	0.073±0.055
0.52 - 0.68	0.59	0.54	0.151±0.053
0.68 - 1.50	0.84	0.60	0.079±0.055

X_F Bin	$\langle X_F \rangle$	$\langle P_{\perp} \rangle$	P_Z
0.00 - 0.45	0.36	0.43	0.040±0.045
0.45 - 0.55	0.50	0.56	0.089±0.055
0.55 - 1.00	0.68	0.64	0.070±0.041

Table 4-3. Polarization Results for $\bar{p} \rightarrow \bar{\Lambda}$

$P_{\perp}$ Bin	$\langle P_{\perp} \rangle$	$\langle X_F \rangle$	P_Z
0.00 - 0.40	0.30	0.46	-0.026±0.070
0.40 - 0.52	0.47	0.53	-0.031±0.083
0.52 - 0.68	0.59	0.56	0.117±0.076
0.68 - 1.50	0.85	0.63	0.173±0.080

X_F Bin	$\langle X_F \rangle$	$\langle P_{\perp} \rangle$	P_Z
0.00 - 0.45	0.36	0.41	0.055±0.069
0.45 - 0.55	0.50	0.53	-0.064±0.081
0.55 - 1.00	0.70	0.61	0.174±0.056

Table 4-4. Polarization Results for $K^- \rightarrow \Lambda$

$P_{\perp}$ Bin	$\langle P_{\perp} \rangle$	$\langle X_F \rangle$	P_Z
0.00 - 0.40	0.28	0.39	-0.234±0.052
0.40 - 0.52	0.46	0.46	-0.419±0.064
0.52 - 0.68	0.60	0.50	-0.438±0.058
0.68 - 1.50	0.85	0.57	-0.615±0.056

X_F Bin	$\langle X_F \rangle$	$\langle P_{\perp} \rangle$	P_Z
0.00 - 0.45	0.36	0.42	-0.326±0.043
0.45 - 0.55	0.50	0.57	-0.466±0.057
0.55 - 1.00	0.66	0.66	-0.470±0.052

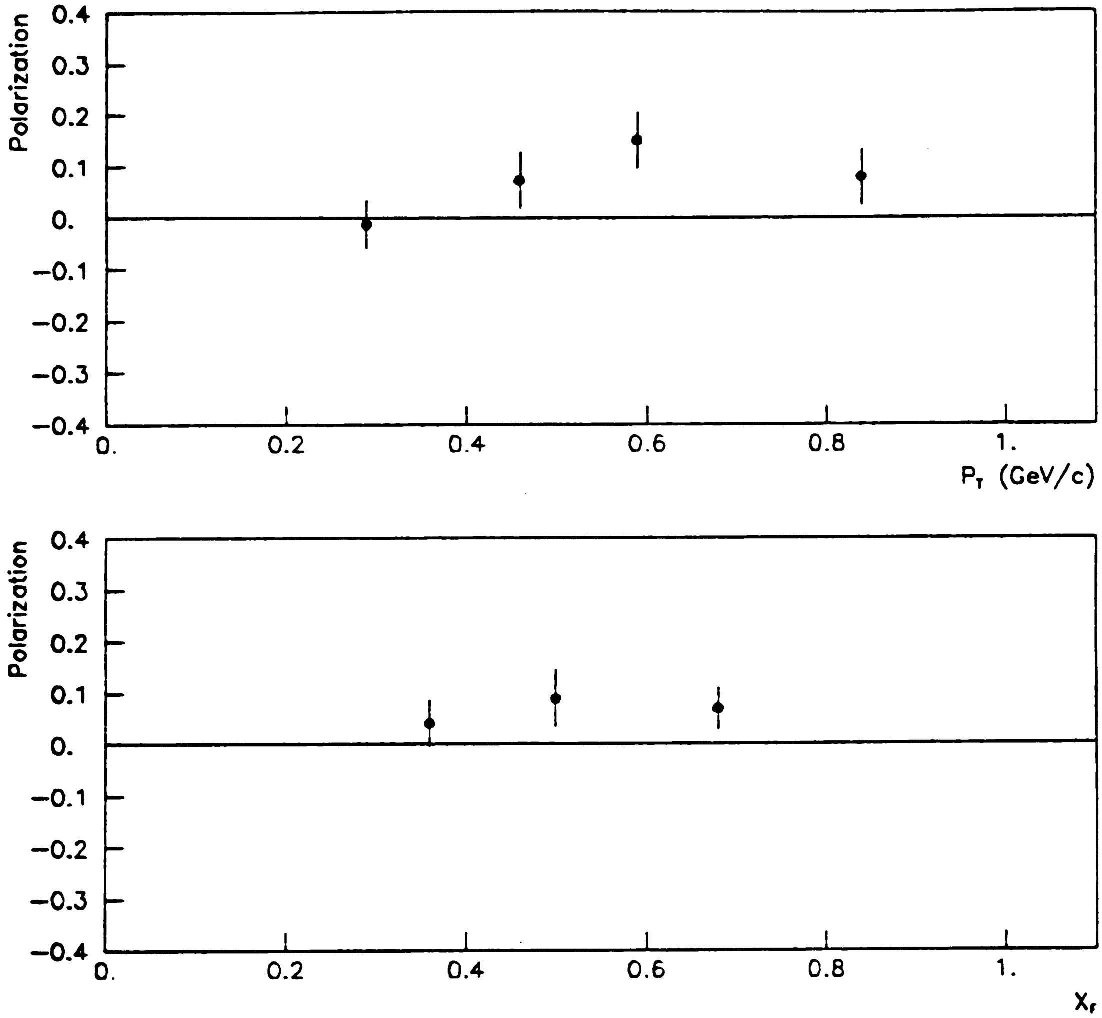

Figure 4-5. Polarization Results for $p \rightarrow \Lambda$

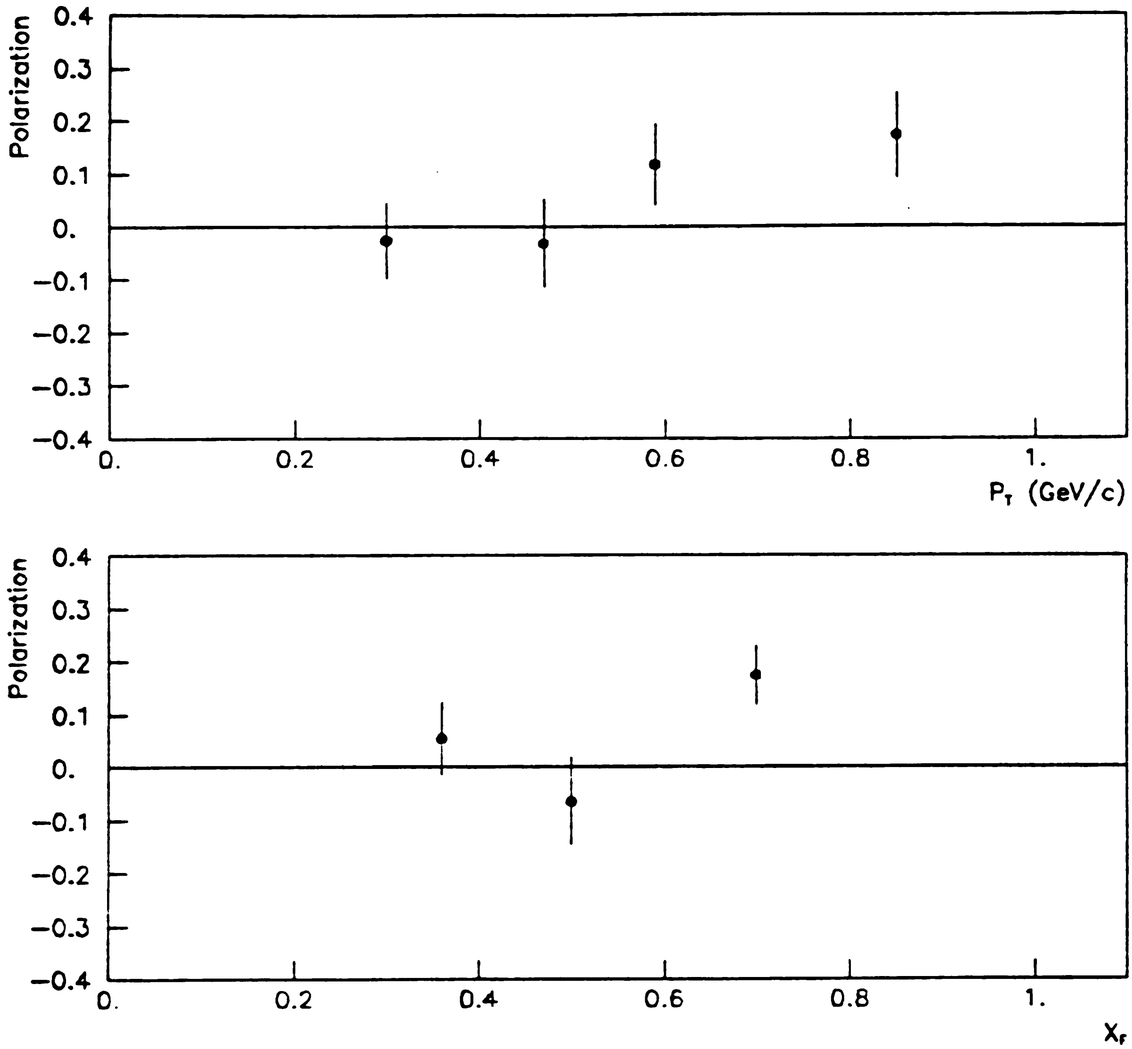

Figure 4-6. Polarization Results for $\bar{p} \to \bar{\Lambda}$

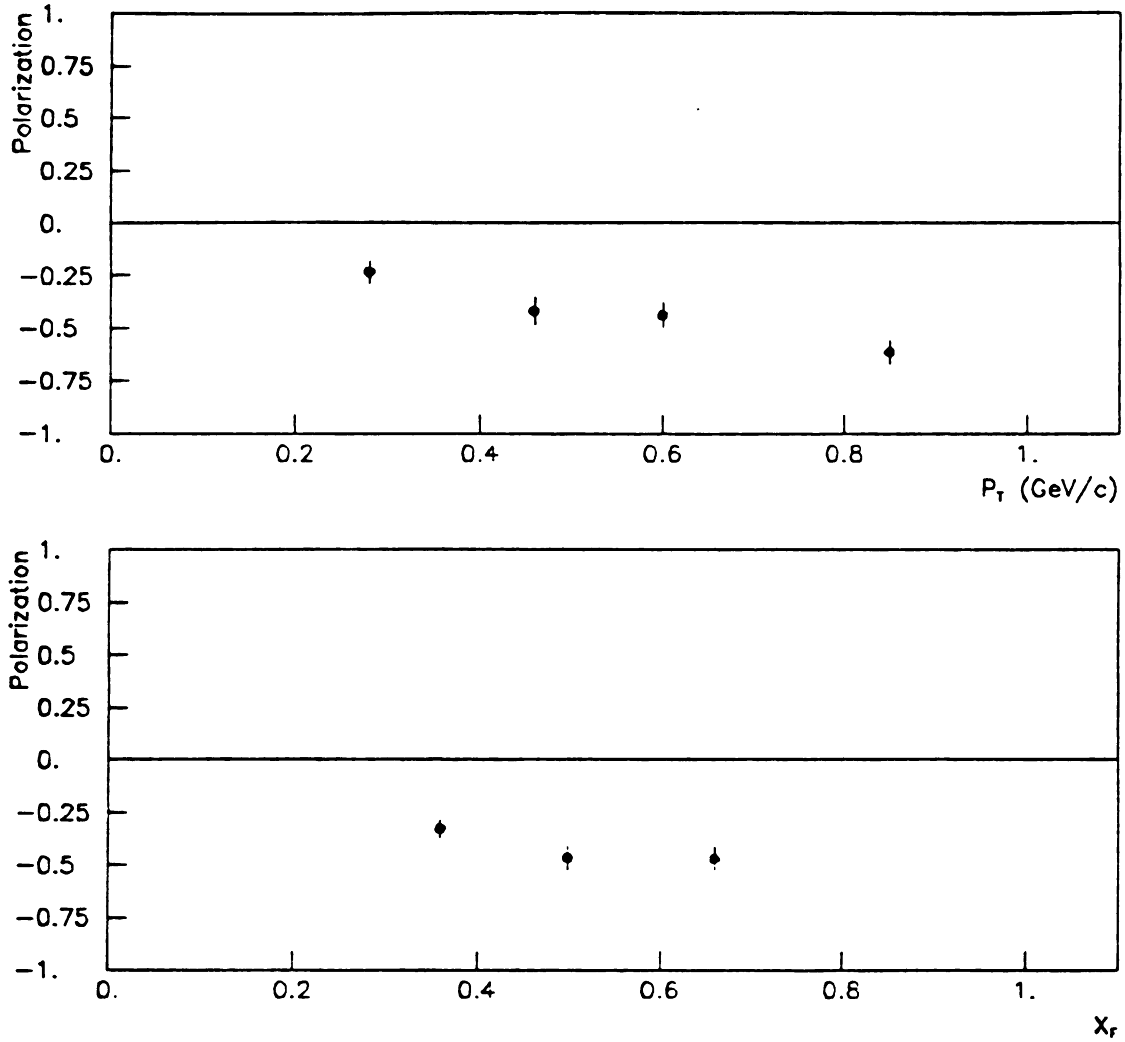

Figure 4-7. Polarization Results for $K^- \to \Lambda$

As can be seen, the results for $p \to \Lambda$ and $\bar{p} \to \bar{\Lambda}$ are severely constrained by statistics, and thus the possible conclusions are quite limited. The two channels show positive polarizations, and are consistent with having equal magnitudes. Using previous measurements as a guide, the polarizations have been fit to linear functions of $P_\perp$. The intercepts for the fits have been constrained to go through zero at zero $P_\perp$. The results are

$$p \to \Lambda \qquad P = (0.136 \pm 0.046)\ P_\perp \quad (\chi^2 = 3.46 \text{ with } N_{DOF} = 3)$$

$$\bar{p} \to \bar{\Lambda} \qquad P = (0.139 \pm 0.067)\ P_\perp \quad (\chi^2 = 2.99 \text{ with } N_{DOF} = 3),$$

and are illustrated in Figure 4-8.

Although the statistics for the $K^- \to \Lambda$ channel are just as bad as the other channels, the signal is much greater. The results of a linear $P_\perp$ fit yield

$$K^- \to \Lambda \qquad P = (-0.756 \pm 0.049)\ P_\perp \quad (\chi^2 = 1.72 \text{ with } N_{DOF} = 3).$$

Comparison of this result to the $p \to \Lambda$ and $\bar{p} \to \bar{\Lambda}$ channels show a polarization of opposite sign, with a slope larger by a factor of 5.6.

Also shown in Figures 4-5 - 4-7 are the polarization results as functions of X_F. All three reactions show non-zero results, however the range of X_F covered by this experiment was not large enough to allow any reasonable determination of the polarization's dependence on X_F.

Comparisons with other experiments are shown in Figure 4-9 and Figure 4-10. No attempt has been made to correct for the kinematical differences between this experiment and the others. The data are in agreement within errors.

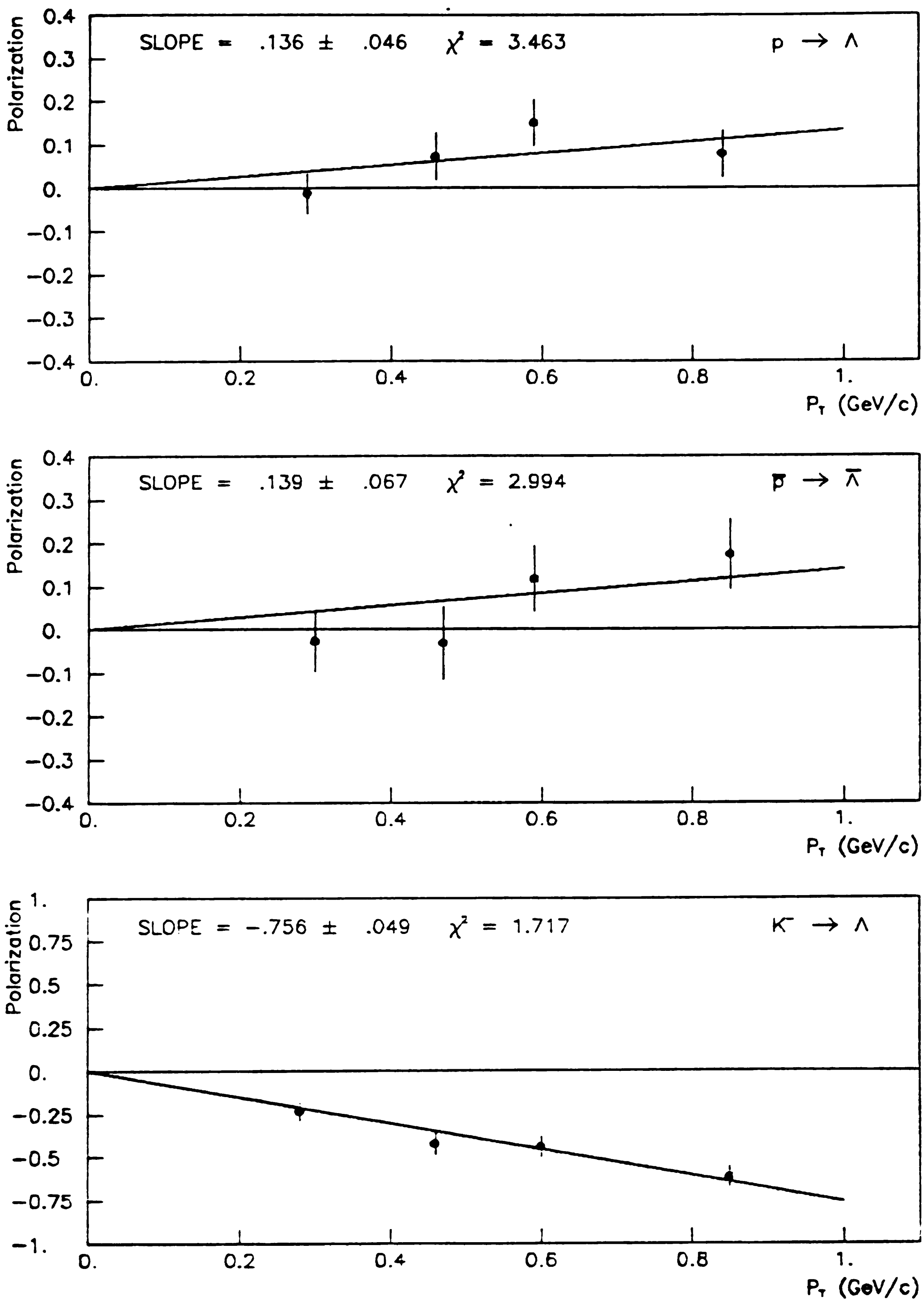

Figure 4-8. Linear Fits of Polarization versus $P_{\perp}$.

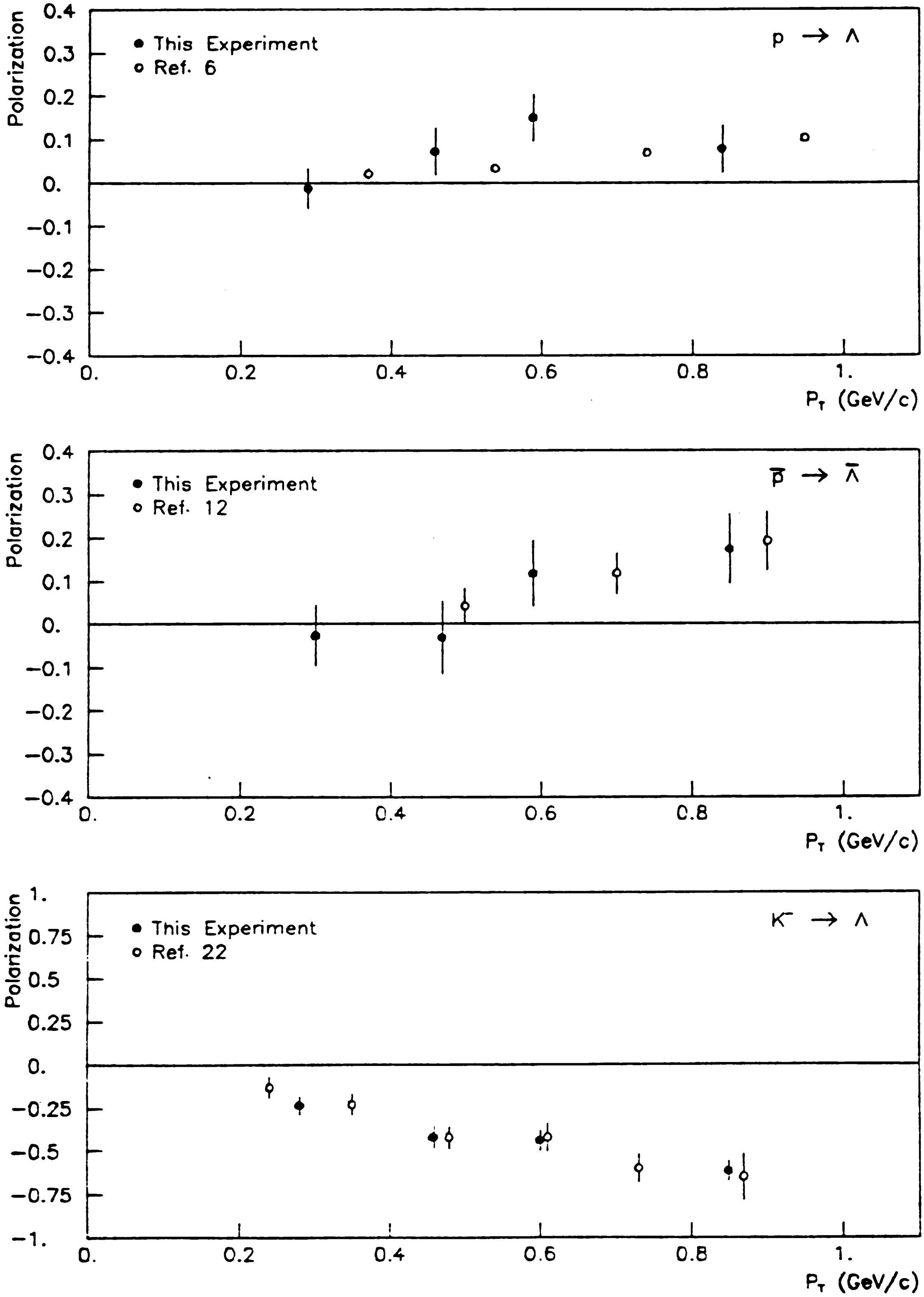

Figure 4-9. Comparison of Results to Previous Experiments (vs. $P_{\perp}$)

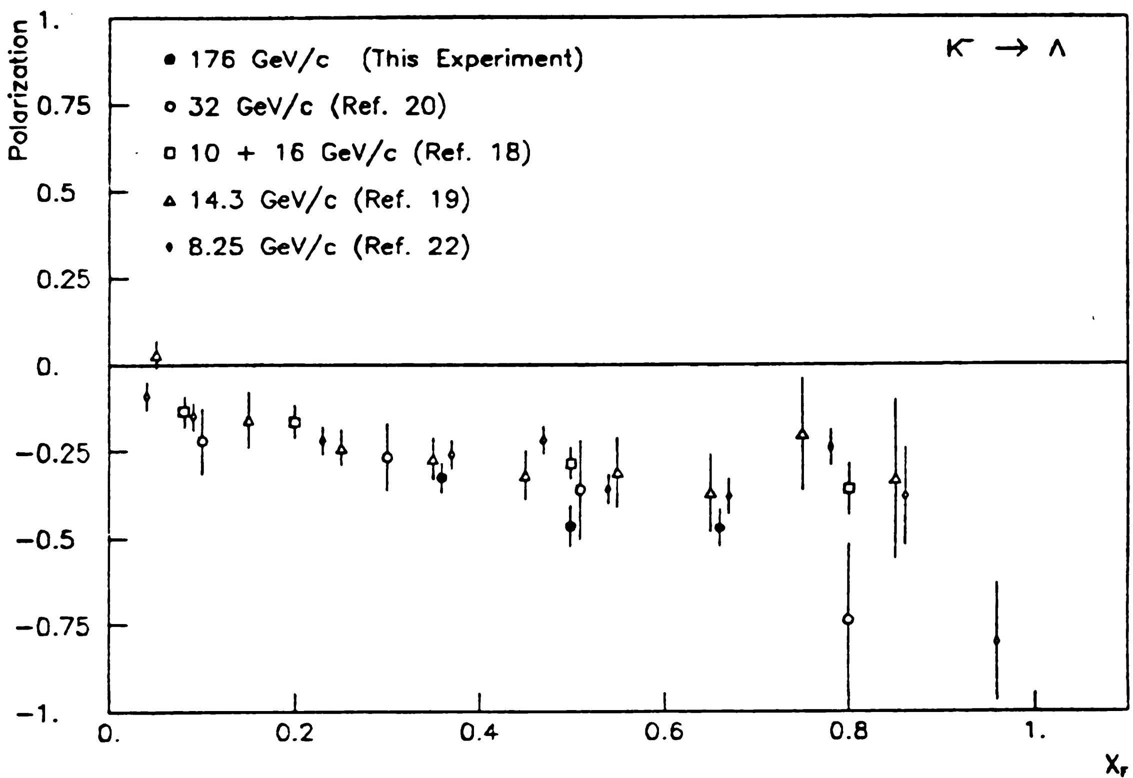

Figure 4-10. Comparison of Results to Previous Experiments (vs. X_F)

4.3 Systematic Errors and Backgrounds

The errors quoted in Table 4-2 - Table 4-4 are statistical only. Systematic errors have been estimated by using the Monte Carlo. As mentioned in Section 2.4, a known source of systematic error was the ramping magnetic field of the sweeper magnet. It was estimated that a 20 % error in the sweeper field would cause less than a 1 % error in the polarization measurement (due to improper precession of the Λ and $\bar{\Lambda}$ spins). The field of the sweeper changed by only ± 4 % during the spill. Systematic errors have also been estimated for possible misalignments of the apparatus and improper resolution modeling by the Monte Carlo. A total systematic error of less than ± 0.015 has been determined, which is negligible compared to the statistical errors.

A known source of background in the lambda and antilambda samples was due to the kinematical overlap between their decays and a K^0_s decay. As mentioned earlier, this background has been corrected for with the Monte Carlo. The relative percentage of K^0_s in the lambda and antilambda samples was 11.2 %, 0.7 % and 0.8 % for the K^-, p and $\bar{p}$ beams respectively. No other source of non-lambda or non-antilambda was considered.

The other type of background in this experiment was due to non-prompt lambda and antilambdas. One potential source for these particles is the radiative decay of a $\Sigma^0 \rightarrow \Lambda\ \gamma$ ($\bar{\Sigma}^0 \rightarrow \bar{\Lambda}\ \gamma$). This experiment was unable to distinguish such decays. The polarization of these Λ's ($\bar{\Lambda}$'s) depends on the initial polarization of the Σ^0 ($\bar{\Sigma}^0$) according to

$$P_{\Lambda(\bar{\Lambda})} = -\frac{1}{3} P_{\Sigma^0(\bar{\Sigma}^0)}. \text{ [42]}$$

In order to correct for such non-prompt Λ's ($\bar{\Lambda}$'s), the polarization and relative production rates for the Σ^0 ($\bar{\Sigma}^0$) must be known.

Measurements have been made of the relative rates for p [43] and K^- [22] beams at lower energies. The results are consistent with

$$\frac{\Sigma^0}{\Sigma^0 + \Lambda} \approx 30\ \%.$$

No data is available for $\bar{p}$ beams. The only Σ^0 polarization measurement [17] has been performed with a p beam. The results are very limited in statistics, but they indicate

$$P_{p\to\Sigma^0} \approx - P_{p\to\Lambda} .$$

With the above information, one can estimate the prompt Λ polarization from $p \to \Lambda$ to be a factor of 1.3 greater than the measured value (assuming the acceptance for non-prompt Λ's is the same as for prompt Λ's). If we assume that $\bar{\Sigma}^0$'s and $\bar{\Lambda}$'s from $\bar{p}$'s behave the same as Σ^0's and Λ's from p's, the prompt $\bar{\Lambda}$ polarization from $\bar{p} \to \bar{\Lambda}$ is also a factor of 1.3 greater than the measured value. Although the relative production rates are known for K^- beams, it is difficult to make any reasonable assumptions about the polarization for $K^- \to \Sigma^0$, and no correction for non-prompt lambdas in the K^- sample has been calculated.

Other potential sources of non-prompt Λ's and $\bar{\Lambda}$'s, such as the radiative decay $\Xi^0 \rightarrow \Lambda\ \gamma$, have considerably smaller cross-sections, and have been ignored.

4.4 Conclusions

The polarization of lambdas and antilambdas has been measured using the reactions

$$p + p \rightarrow \Lambda + X$$
$$\bar{p} + p \rightarrow \bar{\Lambda} + X$$
$$K^- + p \rightarrow \Lambda + X,$$

at a beam momentum of 176 GeV/c, using a liquid hydrogen target. Non-zero results have been obtained for all three channels. With the sign conventions chosen (Section 4.2), the polarizations for $p \rightarrow \Lambda$ and $\bar{p} \rightarrow \bar{\Lambda}$ are positive, equal in magnitude, with an average polarization of 0.063 ± 0.022 within our kinematic range. The polarization for $K^- \rightarrow \Lambda$ is negative, with an average polarization of -0.419 ± 0.029. All reactions are consistent with a linear dependence on $P_\perp$.

When comparing polarization results from various experiments, it is important to note the kinematical regimes of the data, since the polarization is a function of both $P_\perp$ and X_F [5]. The $P_\perp$ and X_F distributions for $p \rightarrow \Lambda$, $\bar{p} \rightarrow \bar{\Lambda}$ and $K^- \rightarrow \Lambda$ are so similar in this experiment, that comparisons of these reactions are possible. While the similarity between the polarization of $p \rightarrow \Lambda$ and $\bar{p} \rightarrow \bar{\Lambda}$ is perhaps understandable, the large signal in $K^- \to \Lambda$ is quite impressive. The reason for the difference may lie in the fact that the s quark in $K^- \to \Lambda$ is a leading parton, where as the s quark in $p \to \Lambda$ ($\bar{s}$ in $\bar{p} \to \bar{\Lambda}$) comes from the sea. Future experiments are needed to study the reaction $K^- \to \Lambda$ in more detail, along with its companion $K^+ \to \bar{\Lambda}$.

The only theoretical model which seems to be consistent with the polarization data is the one by Degrand and Miettinen. It agrees with the signs of the polarizations for all existing data, and except for the signal in $K^- \to \Lambda$, is in reasonable agreement with the relative magnitudes of the various channels. However, its method of determining the actual magnitude is very non-rigorous, and does not seem to give the correct ($P_\perp$, X_F) dependences.

Polarization experiments yield sensitive measurements of spin dependent terms in reaction amplitudes. Before any theory can be declared correct, it must be able to explain such experiments. To date, no theory successfully accomplishes this.

APPENDICES

APPENDIX I

Pattern Recognition Algorithm

The program used for the pattern recognition will be described in detail here. A brief description can be found in Section 3.1.

The program first searches for tracks in the Y view. All possible pairs of Y hits are considered, with the constraint that these pairs of hits must be separated by at least one station. Also, the line defined by the two hits must point back to a region near the target. These constraints help eliminate fake tracks, and improve the speed of the algorithm. Each pair of hits passing these requirements is used as a seed to search for a potential track. Roads along the line defined by the seed pair are searched to find the closest hit within the road for each of the 12 Y planes. The road widths are ± 3 mm for the PWC's and ± 6 mm for the drift chambers. These road widths are very conservative - the PWC resolution is about 0.6 mm and the drift chamber resolution is about 0.4 mm. The reason the drift chambers had such large road widths was that their alignment was initially not as good as the PWC's. If a total of 5 or more hits (including the seed pair) are found, the hit pattern is declared a Y track candidate. Also accepted are roads containing 3 or more PWC hits. No more than 40 such roads are presently allowed. This is limited only by the dimensions of certain arrays in the program. If more than 40 roads are found, the number of hits requirement is increased by one and the previous steps are repeated. This continues until less than 40 roads are found. This procedure is extremely conservative and time-consuming, but also extremely safe. It could be made much faster by reducing the number of seed planes.

Each track candidate is fit to a straight line. All contributing planes are checked for hits which are closer to the fit line. If found, the hit that was used is replaced. If a hit no longer lies within the road, it is removed. If a plane did not contribute, but now has a hit within the road, it is added to the pattern. The new track is refit, and the replacing, removing and/or adding of hits is performed only once more. A cut on the confidence level (probability) of the fit is made. This cut is at 0.001. If the candidate fails the probability cut, the hit with the largest contribution to the χ^2 is removed and the track is refit. This continues until the track passes the probability cut, or until it fails the number of hits requirement. The procedure followed is probably good for tracks which have a large number of good hits and only a few bad hits. It is certainly a bad procedure if the numbers of good and bad hits are similar.

If the track candidate fails to pass these cuts, the above steps are repeated using a fit that allows a bend at the center of the analysis magnet. This is done to pick up tracks that pass near the outer regions of the magnet, where there is a substantial non-vertical component to the field.

No two Y-tracks are allowed to share a hit. If hit sharing is detected, the shared hit is awarded to the better track. In order to determine which track is the better one, a rather involved series of criteria is applied. If both tracks have been fit the same way (straight vs. kinked) and one has a probability that is 200 times that of the other, that track is better. If one track is a straight track and the other is a kinked track, and the straight track has a probability that is 100 times that of the other, it is the better track. If neither of these is true, then the track with the most Y PWC's is better. If this doesn't work, then if one track has 2 more total Y hits on it than the other, it is better. If none of the above is true, and if one of the tracks is straight and the other one is kinked, the straight track is chosen. Finally, if still no track can be determined as better, the track with the highest probability is chosen. The candidate from which the hit has been removed is refit and reconsidered with regard to all Y-track cuts listed above.

This continues until no hits are shared. The above series of rules were determined empirically by examining the behavior of the algorithm on real data, and comparing the results to what the eye considered the correct answer. Candidates making it this far are declared good Y-tracks and will be written onto the output tape.

Next, correlations between Y tracks and hits in the X, U and V chambers are searched for. Combinations of UV, U'V', XU, X'U', XV, and X'V' drift chambers are used from each station. Other combinations are possible, but were ignored to save time.

Hits from each combination are paired together and a Y coordinate is calculated. If this Y coordinate is within the road around a Y track, the pair is considered correlated with that Y track, and is stored. The UV road width is ± 4 mm and the XU and XV road widths are ± 14 mm. A minimum road width is defined to be ± 6 mm for UV and ± 10.5 mm for XU and XV, and it is within this window that most of the real correlations are expected to appear. If a second pair of hits is discovered closer to the Y track than the first, it will replace the first, unless it happens to be within the minimum road. If more than one pair is discovered within the minimum road, they are all recorded up to a limit of four. No priority ordering is done for such multiple pairs. If more than four pairs are found, only the best ones are kept.

Using the found XUV correlations and Y tracks, full space tracks are now searched for. The spectrometer is first split at the magnet into two symmetric halves - an upstream half and a downstream half, each half containing two full stations. Each half is handled independently. If both stations in a half have correlations in them, all possible pairs of combinations are investigated. The program limits the number of such combinations to 16. If a pair is contained in an already found track, it is not investigated. A preliminary fit in the XUV-view to a straight line is made combining these new pairs and the correlated Y track. The Y track is fixed to its previous result. A cut on the probability at 0.001 is made.

If a combination passes this cut, a full XYUV fit is performed and the result of this fit is projected into all planes not already contributing to the space track. The replacing, removing and/or adding of hits that was performed for the Y tracks is now done on the track segments using all chambers. However, the hits forming the initial correlation and the hits on the Y track are not allowed to change during this process.

The track segments surviving the above procedure are stored. These tracks are checked to make sure that no track is a subset of any other. Any subsets are removed.

If no tracks were found in a particular half of the spectrometer, all combinations of X PWC hits and previously found XUV drift chamber correlations are used to form roads, up to a limit of 16 (any more are ignored). These possible roads go through the same testing as previously described. Any track segments surviving these tests are stored.

At this point, there exist possible upstream and downstream track segments that are correlated to Y tracks. An attempt is now made to connect these segments at the analysis magnet. In order to do this matching, each segment pair is examined to see if its X mismatch at the center of the magnet is less than 5 mm. If so, this pair is stored. If not, it is skipped. If a second pair is found with an X mismatch less that the first, but not less than 4 mm, it will replace the first. If two pairs are found with mismatches less than 4 mm, then the pair with the highest probability is chosen.

If no match has been found, the set of upstream segments is compared to the set of downstream segments. The best set is determined by a multi-step procedure. If only one half of the spectrometer has track segments in it, that set is the best. Otherwise, the highest probability in one set is compared to the highest probability in the other set. If one is a factor of 200 more than the other, that set is the best. If a set has a track segment with more X PWC hits on it than every track in the other set, that set is chosen. If this isn't true, the set containing the track segment with the most X hits is picked. Finally, if all else fails, the set containing the track segment with the highest probability is declared the best.

A search for track segments in the non-chosen set that link up to the track segments in the chosen set is now performed. Roads are formed using the previously found XUV correlations in the non-chosen set and the X intercept at the magnet of each track segment in the chosen set. The usual filling in of the road, fitting it, checking its probability (cut at 0.001) and refitting it (if necessary) is done for each road found. Here a minimum of 3 XUV hits in 2 stations or 2 PWC hits is required.

Any candidates passing these cuts are tested to see if the X mismatch at the magnet between it and the track segment used as a seed is within the cut described above. If a pair of upstream and downstream segments have been found that match up, these segments are stored.

If a matching track has still not been found, a sweep search in X is done, using the X intercept of each track in the chosen set as a pivot. This sweep search forms roads using the pivot point and each X hit in the station farthest from the magnet in the spectrometer half being searched. These roads are filled, fit, checked for probability, refit, and matched as previously described.

If there is still no matched track, the half of the spectrometer that was not previously chosen is now used and the above steps repeated.

At this point, no two track segments are allowed to share even a single hit. If such sharing is detected, the hit in question is awarded to the better track. This is determined by another involved procedure. If the probabilities of the two tracks differ by a factor of 20, then the one with the higher probability is the better track. Otherwise, the track with the most number of X PWC hits if the better one. If this is not true, the track with the most number of total XUV hits is the better one. Finally, if none of the above are not true, the track with the highest probability is chosen.

An attempt is now made to use the X PWC's as seeds. All combinations of X PWC hits that form 4 hit X tracks that meet at the magnet are examined. Each X PWC track is combined with each Y track previously found (regardless of whether that Y track has already been linked to an XUV track). This XY track forms a road which is filled in, fit, checked for probability, refit, and matched at the magnet. If this XY combination fails to pass these cuts, it is ignored. If it passes these cuts, it is required to have at least one UV hit or it is also ignored. If the new XYUV track passes all of the above cuts, and no previous XYUV track had been previously found, the new XYUV track is saved. If an XYUV track had been found, it is compared to the new XYUV track. The track with the most number of hits is saved and the other one ignored.

Up to this point, XUV hit sharing has only been checked when comparing track segments linked to the same Y track. An attempt is now made to eliminate XUV hit sharing between different XYUV tracks. If sharing is detected, the hits are removed from the worse track unless the two tracks share 3 or fewer hits. If so, it is impossible at this point to tell which track is worse, and they are allowed to keep these hits. However, if the hits are to be removed, the worse track is determined by the following series of tests. If one track has fewer X PWC hits than the other, it is worse. Otherwise, the track with the fewest total XUV hits is worse. Finally, the track with the lower probability is worse.

After the hits are removed, the track is refit and tested to see if it passes all of the cuts. If not, it is eliminated from the list. All patterns of hits previously stored are written onto tape for later use by the data reduction phase.

APPENDIX II

Drift Chamber Alignment

In order to determine spatial position from clock time in the drift chambers, a set of alignment constants was needed. These constants were determined offline by using the PWC system as a reference. Tapes containing muon triggers (Section 2.7.3) were processed through an analysis program that required each event to contain one and only one forward track, with at least 7 PWC hits on that track. These tracks were then fit to straight lines using the PWC's only, and the χ^2 per degree of freedom was required to be less than 5.0. With these requirements, 220,000 muon events were obtained. They had the properties of being well defined, straight spatial tracks that did not require any a priori drift chamber alignment. For the purpose of the drift chamber analysis, only these muon events were used.

By plotting the position of the muon given by the PWC track versus the clock value for the cell that the muon went through, several features were observed (See Figure II-1). The expected linear relationship between position and time can be seen (A). Also evident is the dead time of the amplifier (B), and the noise in the system (C).

Finally, unexpected crosstalk between neighboring wires is seen (D).

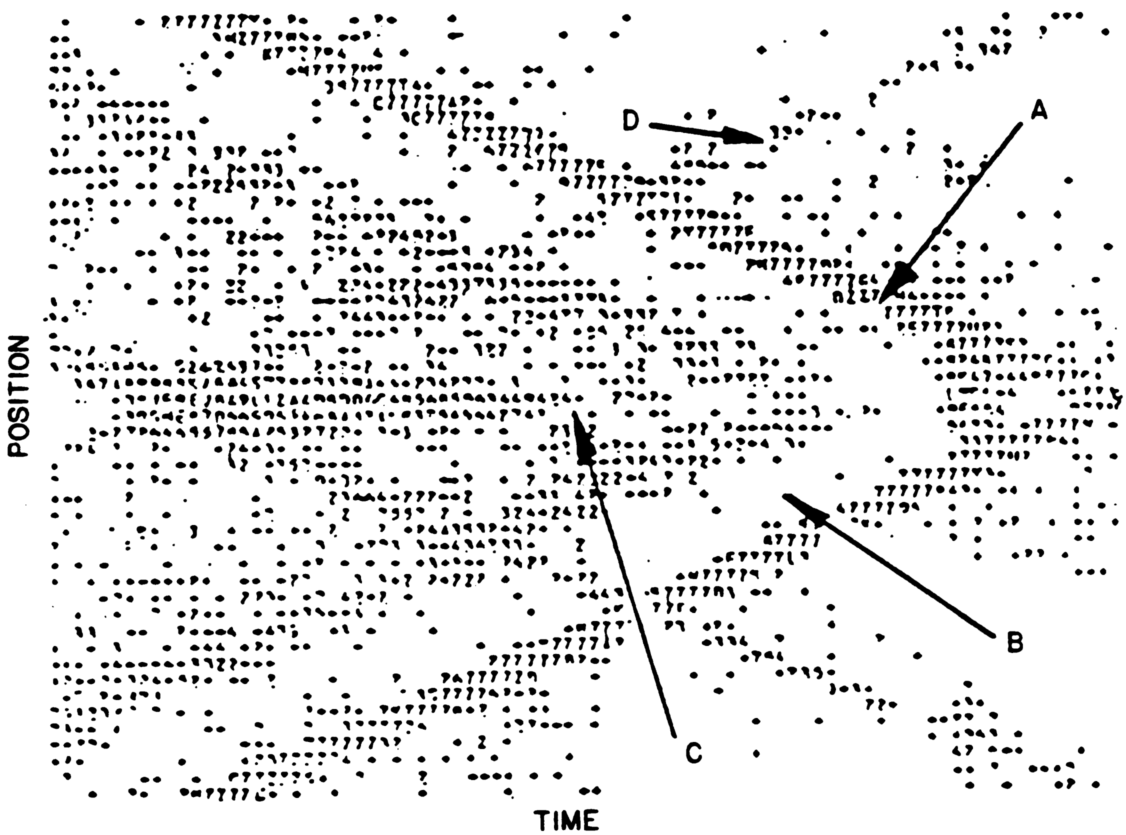

Figure II-1. Position versus Time for a Drift Chamber Cell

Only those clock times that belonged to feature A were considered valid. Upon closer examination of these times, it was found that a nonlinear relationship existed between position and time for hits near both the sense wire and the high voltage wires. The size of the nonlinear region near the high voltage wires was ~ 5 mm and that near the sense wire was ~ 3 mm. The nonlinearity near the field wires was about a factor of 5 worse than near the sense wires. These nonlinearities are attributed to large fluctuations in the electric fields at these points.

In order to parameterise the linear region, the functional form

$$X = X_0 \pm V_{\pm} (T_0 - T) \quad \text{(II-1)}$$

was used where T is the clock time, X_0 is the wire location, T_0 is an offset time, $V_{\pm}$ are drift velocities (one for either side of the wire), and X is the position of the hit. The constants X_0, T_0 and $V_{\pm}$ were obtained for each wire by fitting feature A to Equation II-1 in the linear regions. In addition, another parameter, θ, was needed to describe the rotation of each wire away from its nominal orientation (i.e., vertical for X chambers). The average rotation of the wires was 1.4 mrad. The nonlinear regions were handled by creating lookup tables which contained corrections to the linear function. A total of 25 alignment constants was used for each of the 418 wires in the system.

APPENDIX III

The Polarization Fit

The center of mass distribution of pions from lambda decays is

$$\frac{dN}{d\Omega} = \frac{1}{4\pi} \left(1 + \alpha_\Lambda \left[P_X \sin\theta \cos\phi + P_Y \sin\theta \sin\phi + P_Z \cos\theta \right] \right)$$

where P_X, P_Y and P_Z are the components of the polarization vector $\vec{P}$, and θ and ϕ are the azimuthal and polar angles of the pion. This equation is modified by the acceptance function $A(\theta,\phi)$ to become

$$\frac{dN'}{d\Omega} = \frac{A(\theta,\phi)}{4\pi} \left(1 + \alpha_\Lambda \left[P_X \sin\theta \cos\phi + P_Y \sin\theta \sin\phi + P_Z \cos\theta \right] \right).$$

The data were analyzed by binning over $P_\perp$ (X_F) and then within each $P_\perp$ (X_F) bin, binning over $\cos\theta$ and ϕ. Each $P_\perp$ (X_F) bin was handled independently.

The acceptance for a particular $(\cos\theta_i,\phi_j)$ bin was calculated as

$$A_{i,j} = \frac{\displaystyle\int_{\cos\theta_i-\Delta\cos\theta/2}^{\cos\theta_i+\Delta\cos\theta/2} \int_{\phi_j-\Delta\phi/2}^{\phi_j+\Delta\phi/2} N_{REC}(\cos\theta,\phi)\ d\cos\theta\ d\phi}{\displaystyle\int_{\cos\theta_i-\Delta\cos\theta/2}^{\cos\theta_i+\Delta\cos\theta/2} \int_{\phi_j-\Delta\phi/2}^{\phi_j+\Delta\phi/2} N_{GEN}(\cos\theta,\phi)\ d\cos\theta\ d\phi}$$

where $N_{REC}(\cos\theta,\phi)$ and $N_{GEN}(\cos\theta,\phi)$ are the number of reconstructed and generated events with $(\cos\theta,\phi)$ given by the Monte Carlo, and $\Delta\cos\theta$ and $\Delta\phi$ are the bin widths used. Binning over $\cos\theta$ and ϕ changes the pion angular distribution into

$$\frac{\Delta N'}{\Delta\Omega} = \frac{A_{i,j}}{4\pi} \int_{\cos\theta_i - \Delta\cos\theta/2}^{\cos\theta_i + \Delta\cos\theta/2} \int_{\phi_j - \Delta\phi/2}^{\phi_j + \Delta\phi/2} \frac{dN}{d\Omega}\, d\cos\theta\, d\phi$$

$$= \frac{A_{i,j}}{4\pi} \left(I^1_{i,j} + \alpha_\Lambda \left[P_X I^2_{i,j} + P_Y I^3_{i,j} + P_Z I^4_{i,j} \right] \right)$$

where

$$I^1_{i,j} = \Delta\cos\theta\, \Delta\phi$$

$$I^2_{i,j} = \tfrac{1}{2} \left[\eta_2 \sqrt{1 - \eta_2^2} + \sin^{-1}\eta_2 - \eta_1 \sqrt{1 - \eta_1^2} + \sin^{-1}\eta_1 \right] \times \left(2 \cos\phi_j \sin\Delta\phi/2 \right)$$

$$I^3_{i,j} = \tfrac{1}{2} \left[\eta_2 \sqrt{1 - \eta_2^2} + \sin^{-1}\eta_2 - \eta_1 \sqrt{1 - \eta_1^2} + \sin^{-1}\eta_1 \right] \times \left(2 \sin\phi_j \sin\Delta\phi/2 \right)$$

$$I^4_{i,j} = \cos\theta_i\, \Delta\cos\theta\, \Delta\phi$$

$$\eta_2 = \cos\theta_i + \Delta\cos\theta/2$$

$$\eta_1 = \cos\theta_i - \Delta\cos\theta/2 .$$

A least squares fit of the data to Equation III-1 was performed. The χ^2 that was minimized was

$$\chi^2 = \sum_{ij} \left[\frac{D_{i,j} - N\, A_{i,j} \left(I^1_{i,j} + \alpha_\Lambda \,[\, P_X\, I^2_{i,j} + P_Y\, I^3_{i,j} + P_Z\, I^4_{i,j} \,] \right)}{\sqrt{D_{i,j}}} \right]^2$$

where

$$N = \frac{\sum D_{i,j}}{\sum A_{i,j} \left(I^1_{i,j} + \alpha_\Lambda \,[\, P_X\, I^2_{i,j} + P_Y\, I^3_{i,j} + P_Z\, I^4_{i,j} \,] \right)}$$

normalized the Monte Carlo to the data. The program DUBNAL (originally FUMILI) in the Fermilab Cyber Computer Library was used to minimize this expression for P_X, P_Y and P_Z. The results did not depend on the $(\cos\theta,\ \phi)$ binning.

LIST OF REFERENCES

LIST OF REFERENCES

1) A. Gaidot, *et al.*, Phys. Lett. 57B (1975) 389.

2) G. L. Kane, J. Pumplin and W. Repko, Phys. Rev. Lett. 41 (1978) 1689.

3) G. Bunce, *et al.*, Phys. Rev. Lett. 36 (1976) 1113.

4) L. G. Pondrom, Proc. of XIV International Symposium on Multiparticle Dynamics, Eds. P. Yager and J. F. Gunion (1983) 563.

5) B. Lundberg, Ph.D. Thesis, University of Wisconsin-Madison (unpublished).

6) K. Heller, *et al.*, Phys. Rev. Lett. 41 (1978) 607.

7) S. Erhan, *et al.*, Phys. Lett. 82B (1979) 301.

8) K. Raychaudhuri, *et al.*, Phys. Lett. 90B (1980) 319.

9) F. Abe, *et al.*, Phys. Rev. Lett. 50 (1983) 1102.

10) K. Heller, *et al.*, Phys. Lett. 68B (1977) 480.

11) F. Lomanno, *et al.*, Phys. Rev. Lett. 43 (1979) 1905.

12) P. Chauvat, *et al.*, Cern Preprint CERN-EP/83-104.

13) O. E. Overseth, High Energy Physics with Polarized Beams and Polarized Targets , Proc. of the 1980 International Symposium, Eds. C. Joseph and J. Soffer (1980) 114.

14) K. Heller, *et al.*, Phys. Rev. Lett. 51 (1983) 2025.

15) C. Wilkinson, *et al.*, Phys. Rev. Lett. 46 (1981) 803.

16) P. S. Cooper, High Energy Spin Physics AIP Conference Proceedings No. 95, Particles and Fields subseries No. 28, edited by G. Bunce (1982) 102.

17) E. C. Dukes, Ph. D. Thesis, University of Michigan (unpublished).

18) H. Grässler, *et al.*, Nucl. Phys. B136 (1978) 386.

19) H. Abramowicz, *et al.*, Nucl. Phys. B105 (1976) 222.

20) M. L. Faccini-Turluer, *et al.*, Particles and Fields (1979) 19.

21) I. V. Ajinenko, *et al.*, Phys. Lett. 121B (1983) 183.

22) M. Baubillier, *et al.*, Nucl. Phys. B148 (1979) 18.

23) R. Rameika, High Energy Spin Physics AIP Conference Proceedings No. 95, Particles and Fields subseries No. 28, edited by G. Bunce (1983) 77.

24) J. R. Bensinger, *ibid.*, 126.

25) D. Aston, *et al.*, Nuc. Phys. B195 (1982) 189.

26) Barth, *et al.*, Z. Physik C10 (1981) 205.

27) B. Andersson, G. Gustafson and G. Ingelman, Phys. Lett. 85B (1979) 417.

28) T. A. DeGrand and H. I. Miettinen, Phys. Rev. D 24 (1981) 2419.

29) M. Roos, *et al.* (Particle Data Group), Phys. Lett. 111B (1982) 1.

30) F. Paige, D. Sidhu, Phys. Rev. D14 (1976) 2307.

31) G. Gustafson, High Energy Spin Physics AIP Conference Proceedings No. 95, Particles and Fields subseries No. 28, edited by G. Bunce (1983) 355.

32) H. Kobrak, R. Pitt and R. Swanson, Fermilab Technical Memo TM-597 (1975).

33) The Cerenkov counter was patterned after a design by S. Pruss of Fermilab.

34) The beam chambers were constructed by the Research Services Department of the Fermi National Accelerator Laboratory.

35) M. Abolins *et al.*, Nucl. Instr. Meth. 192 (1982) 331.

36) Model WCS-200 Wire Chamber Scanner manufactured by Nanometric Systems, Inc., 837 North Cuyler Avenue, Oak Park, IL 60302.

37) The PWC's were built by the Carleton University Physical Sciences Shop.

38) The Drift Chambers were built by Nanometric Systems, Inc..

39) T. F. Droege, M. M. Watson and T. R. Wesson, IEEE Trans. Nucl. Sci. NS-23 (1976) No. 1 248.

40) S. Goudsmit and J. L. Saunderson, Phys. Rev. 57 (1940) 24.

41) L. Schachinger, *et al.*, Phys. Rev. Lett. 41 (1978) 1348.

42) R. Gatto, Phys. Rev. 109 (1958) 610.

43) M. W. Sullivan, *et al.*, Phys. Lett. 142B (1984) 451.